NORTHWESTERN UNIVERSITY

Entanglement Generation in Green Fluorescent Proteins

A DISSERTATION

SUBMITTED TO THE GRADUATE SCHOOL

IN PARTIAL FULFILMENT OF THE REQUIREMENTS

for the degree

DOCTOR OF PHILOSOPHY

Field of Physics and Astronomy

By

Siyuan Shi

EVANSTON, ILLINOIS

September 2018

Abstract

Entanglement Generation in Green Fluorescent Proteins

Siyuan Shi

The recent development of quantum biology results in various breakthroughs in exploring the role of quantum physics in biological systems, as well as in observing and controlling light-matter interactions in biological materials on a fundamental quantum level. We seek to combine the concept of quantum biology with quantum optics to gain a better understanding of the role of quantum physics in biology to enable some novel applications in applying quantum tools in biological materials. Specifically, we have chosen green fluorescent protein as a medium for investigating the quantum effects. In this dissertation, we study the origin of the nonlinearity, generate photon pairs inside the green fluorescent proteins through the four-wave mixing process, measure and improve the purity of the generated photon pairs, and create quantum entanglement within the green fluorescent proteins.

Acknowledgements

I would like to start by thanking my mom and dad. I am grateful for their support, although they live in China, but I feel like that they are always around for backing me up and encouraging me to move forward through the whole Ph.D. journey. My mom talks with me every week, where I share my discoveries, perspectives, happiness, and sometimes pain with her. My dad seldomly talks with me, but every talk is meaningful with a lot of life wisdoms.

I would like to express the deepest appreciation to my academic supervisor Professor Prem Kumar, who has the attitude and the substance of a genius: he continually and convincingly conveyed a passion and seriousness about research, and an excitement about teaching. This dissertation would not be possible without his guidance and persistent help.

I would like to thank my committee members, Professor Nathaniel Stern and Professor John Ketterson for their insightful comments and encouragement, and for the hard question which incented me to widen my research from various perspectives.

I would like to thank Prof. Kim Fook Lee and Dr. Abu Thomas for the stimulating discussions, for the countless days we were working together in front of the experimental setup, and for the insightful inputs to the publications.

I would like to thank my fellow labmates for the interesting discussions, and for all the fun we have had in the last seven years. Also, I would like to thank my friends at Northwestern University, including Xiao, who has my roommate for 10 years since undergraduate college, my friends Bo, Huanxin, and Hao, in the physics department, and my friends Zixuan, Chen, and Li, who help me a lot in preparation for the career.

Contents

List of Figures

1. **Chapter 1. Introduction**

We have witnessed the development of quantum biology in recent years. Specifically, people have been asking and exploring the role of quantum physics in biological systems. For example, researchers have found evidences for quantum coherence in photosynthesis [1], quantum entanglement in light-harvesting complexes [2], and quantum mechanism in magnetoreception [3]. We, as an expert in entangled photon sources [4, 5], have been asking ourselves a question: can we combine the concept of quantum biology with quantum optics, to gain a better understanding of the role of quantum physics in biology, or enable some novel applications in applying quantum tools in biological materials. Specifically, we have chosen the green fluorescent protein (GFP) as a medium for investigating the quantum effects. GFP is a novel material discovered in1962 [6] by Shimomura, who first purified it from Aequorea victoria. GFP is ideal for our study since it can be cloned, engineered, and recombinantly expressed, which has opened a new gate in cellular and molecular biology. Applications of GFP include biological cell lasers [7, 8], high resolution optical imaging [9], measurement of single-molecule movement [10], etc. What's more, two-photon excitation of GFP has found many potential applications in biomedical imaging [11]. And this could see potential applications in quantum spectroscopy [12] for using novel quantum control knobs to explore the light-matter interactions and enhancing the precision for certain measurement in biological materials [13].

In this study, we utilize the $\chi^{(3)}$ nonlinearity of GFP for the generation of correlated/entangled photon pairs through a spontaneous four-wave mixing (SpFWM) process. This is the first step toward developing a quantum information processing platform in a biological environment. Our goal is to explore the quantum nonlinearity in biological systems. In this chapter, we first outline the brief history of the study of quantum biology, and then introduce some interesting applications such as GFP-based biological cell laser for biomedical imaging.

1.1 Quantum Biology

Before the twentieth century, physics hardly play a role in the study of biology due to the complexity of living beings. In the early twentieth century, the invention of more powerful microscopes and techniques has enabled the possibility of using physical and mathematical methods to describe microscopic biological systems [14]. Remarkably, Schrödinger predicted several functional features of DNA in his lecture series. Niels Bohr, Pascual Jordan, and Max Delbruck argued that the quantum idea of complementarity was fundamental to the life sciences [15]. In 1965, Per-Olov Löwdin stated that a new field of study called "quantum biology" [16].

Quantum biology relies on quantum mechanics and theoretical chemistry to explain and apply the effects occurring in biological systems. Many biological processes involve the transformation of energy into other forms to be used in chemical reactions

and are quantum mechanical in nature. For example, chemical reactions, light absorption, transfer of excitation energy, and transfer of electrons and protons are typical natural biological processes that involve quantum effects. Specifically, in light absorption, consider a photon being absorbed by the system and its energy is taken up by the matter, typically in the forms of excited electrons in an atom. Therefore, the electromagnetic energy is transformed into the kinetic and potential energies of an electron. This energy may be further transformed into chemical energy, electromagnetic radiation, or thermal energy via chemical reactions. Quantum biology reveals the quantum nature of such biological interactions by modeling them with quantum-physics tools. Now that we understand that quantum mechanics can play a role in biology, a new question is raised: how important is the role? In other words, are there any advantages the quantum effects can bring to the biological systems that the classical effects cannot? Are there any tasks that can only be performed using quantum mechanics?

Researchers are still looking for the answer. Although quantum mechanics clearly exists in biology, however, in many complex biological systems, the physiological impacts of quantum mechanics still requires further study. In the past decades, many experiments suggest that quantum mechanics may be harnessed for biological advantages in some cases. For example, studies have suggested that certain natural processes such as photosynthesis[1] and avian magnetoreception[3] can take advantage of quantum coherence in biological systems. Light harvesting complexes

(LHC)[2] and avian magnetoreception can exhibit quantum superposition and non-locality based on absorption of coherent [17] and incoherent light [18], respectively. Upon absorbing the light through the linear (one-photon) or nonlinear (two-photon) processes, the entangled biological systems (electron-spin states and chromophore sites) act as quantum meters [19] for measuring quantum effects in avian bio-compass and excitation energy transfer in photosynthesis.

1.2   Quantum Spectroscopy

Along with the development of quantum biology is the growth of quantum spectroscopy. Quantum spectroscopy is an emerging spectroscopic technique thriving from the recent advances in quantum optics [20, 21] where the nonlinear radiation field is down to the few-photon level, thus the quantum nature of field is manifested and must be considered. Like the conventional nonlinear spectroscopy where classical light is used to detect matter properties, quantum spectroscopy also aims at light-matter interactions. However, unlike conventional spectroscopy where the variation of frequencies and time delays of classical light work as control knobs, quantum spectroscopy utilizes the parameters of the quantum state of light as novel control knobs [22] to supplement the classical parameters. The distinctive advantages of quantum light in spectroscopy stem from improved signal-to-noise ratio owing to strong correlation between light and matter, particularly quantum entanglement [23].

Advances in both quantum biology and quantum spectroscopy have driven our attention to develop novel quantum spectroscopic techniques in biological materials. The generation of entangled photon pairs in the green fluorescent protein (GFP) is the most fundamental basis for the development where the entanglement is generated in situ.

1.3   Green Fluorescent Protein

1.3.1   History of Green Fluorescent Protein

In 1962, Shimomura et al. extracted the GFP from the jellyfish *Aequorea Victoria* [6]. GFP is composed of 238 amino acid residues and exhibits green fluorescence when exposed to light in the blue to ultraviolet range [24]. Although GFP exhibits many unique and promising features in both biology and optics, utilizing GFP as a tool for molecular biologists had not begun until 30 years since the extraction. The revolution started in 1992 when Douglas Prasher reported the cloning and nucleotide sequence of wtGFP [25]. Remarkably, in biology, the original GFP was expressed in the nematode C. Elegans and used as a marker for gene expression[26]. In physics, people have studied and utilized the high quantum efficiency (~80%) of the green fluorescence [27]. What makes GFP more valuable is that it can be expressed by a wide variety of organisms and fused to other proteins while maintaining its unique fluorescence capability [10, 24, 28]. Nowadays, there are 20 naturally occurring and artificially engineered fluorescent proteins (FPs). These proteins are used for the study of

intracellular dynamics[29, 30], reporter gene technology [31], drug discovery [32], and super-resolution microscopy [11, 33, 34]. In 2008, Nobel Prize in chemistry was awarded to Chalfie, Shimomura, and Tsien for honoring their discovery and development of GFP.

1.3.2   Applications of Green Fluorescent Proteins

Some applications are noteworthy. For example, the development of biological cell lasers based on GFP. Lasers have been widely used in many parts of modern society. Its applications range from science, optical communication, medicine to entertainment. To meet a variety of needs, different types of lasers have been invented, including the biological cell laser. Of all these different types of lasers, the most essential part is the gain medium, which exist in three aggregate forms—gaseous, liquid, and solid. And FP is used as the gain material in developing a microlaser [8, 35]; the laser made of the GFP-expressing *Escherichia coli* bacteria has seen a clear threshold behavior and discrete peaks in its emission spectrum. The development keeps moving forward. Nowadays, we have seen the novel invention of optofluidic biolasers [7]. They incorporate biological molecules into the gain medium and contain optical cavities in fluidic environments. The unique property of these lasers is that, during laser generation, tiny changes in biological processes in the gain medium are amplified. As a result, researchers can use the amplified light to quantify the tiny changes induced by some biological processes in the gain medium [8, 35-39]. In more details, the

number of gain molecules is increased/reduced due to some biochemical or biological processes. These increasing/reducing molecules not only change the gain of the resonant cavity but may also change the refractive index of it. Within the resonant cavity, light bounces back and forth while interacting with the gain medium. At last, when the amplified light eventually leaves the resonant cavity, its output intensity, spectrum, threshold and other characteristics are measured and recorded as clues to determine the gain medium characteristics. Therefore, the optofluidic biolasers have been developed into a highly sensitive way to measure the changes in biological molecules. The uniqueness of this detection method is that it utilizes the amplifying power of stimulated emission, which is different from conventional fluorescence-based detection.

Another example involves GFP in the optical imaging. In a conventional fluorescence microscope, the main limit is its spatial resolution. To see clearer images, the numerical aperture of the lens needs to be small. However, as the aperture decreases, due to diffraction, light cannot be focused more sharply than $\lambda/2NA$, where NA is the numerical aperture of the lens, λ is the wavelength of light. Researchers have proposed a method to overcome this problem. That is to force the fluorescence features of the object fluoresce sequentially [40]. This method requires a mechanism working as a switch. When the switch is turned on, the fluorophores under control are able to fluoresce; when the switch is turned off, those fluorophores become non-fluorescent. The requirement has been fulfilled by introducing a reversibly

switchable enhanced green fluorescent protein (rsEGFP). Thus, microscope based on rsEGFP has been invented. Another advantage of rsEGFP based microscope is that rsEGFP can work with low levels of light which is favored in many applications [41-44]. As a result, researchers have reached imaging resolution of < 40 nm in living cells by distributing functional rsEGFP-fusion proteins into those cells. The rsEGFP has also shown its application in data storage [45].

Another application of fluorescent proteins is to image protein-protein interaction [46]. Different methods are proposed. The first method is known as fluorescence correlation spectroscopy (FCS) [47]. FCS is a method based on correlation analysis. It analyzes the correlation of fluorescence fluctuations in a defined illumination volume fixed in space. In details, fluorescently labeled proteins are prepared in a cell where light focuses onto. These fluorescently labeled proteins may interact with each other. Researchers are able to track the protein-protein interaction by measuring and analyzing the differences in fluorescence diffusion times. However, FCS is relatively insensitive to changes in molecular mass [48]. The second method known as fluorescence cross-correlation spectroscopy (FCCS) appears to be more sensitive than FCS [49]. FCCS traces two spectrally distinguishable fluorophores to identify when the two molecules coincide. To obtain more details of the molecular interaction, a third method called fluorescence resonance energy transfer (FRET) can be applied [50]. FRET provides spatial and temporal information of protein-protein interactions

The potential application of FPs in quantum technology still awaits exploration. The generation of non-classical light, such as squeezed and entangled light, in biologically produced FPs would open the potential for quantum spectroscopy and quantum-enhanced measurements in biological systems because entanglement can provide precision that surpasses the uncertainty principle [51]. Entanglement can be generated in FPs owing to the strong optical nonlinearity [52] and the process can be quite efficient because of the protective beta-barrel structure surrounding the fluorophore in the protein [53]. In addition, since the FPs strongly couple to light, even at the single-photon level, it is feasible that quantum-optic techniques for creating, manipulating, and characterizing photonic quantum states, developed for use in quantum information processing (QIP), could be directly applied to FPs. By projecting the entanglement of the quantum fields back to FPs, precise preparation and control of higher excited states [54-56] may be feasible.

The nonlinearity of FPs has been explored in many areas. Their nonlinearities arise from transition dipole moment and permanent dipole moment difference between ground state and excited state [52, 57]. The properties of two-photon absorption of FPs have been studied thoroughly and developed for biomedical imaging. For example, two-photon laser scanning microscopy has been developed to image living tissues up to a very high depth [58, 59]. In addition, the dispersive optical nonlinearities of FPs can be explored for developing biologically engineerable sources of quantum light states [60, 61]. In our group, we have measured the $\chi^{(3)}$ of GFP by

using a z-scan technique. We obtain two-photon absorption coefficient $\beta = 0.05 \pm 0.03$ cm/GW and the nonlinear index $n_2 = 10^{-19}$ m^2/W. Correlated photon pairs can be generated in fluorescent protein samples through a phase-matched four-wave mixing process [62].

Photosynthetic systems have shown high efficiency in energy harvesting and transporting [1, 2]. The key to this high efficiency is attributed to the existence of long-lived (several hundred femtoseconds) quantum coherence in the energy transfer processes [63, 64]. Two-dimensional electronic spectroscopy method based on four-wave mixing process has been used to study the quantum coherence of energy transfer process. In the method, two phase-locked, ultrashort pump beams interact with the system. Then the system is left for evolving for some time duration before the third signal beam is sent in. In this four-wave mixing configuration, the generated signals are mapped onto a two-dimensional frequency-frequency domain for analyzing the quantum beats arising from quantum coherence. In addition, researchers are working on building biological models for exploring the quantum nonlinearity of the photosynthetic systems [65-68]. Recently, it is proven that a small synthetic molecule can reproduce the nonlinear quantum coherence with a remarkable lifetime [63].

2 Chapter2. Theory Background

2.1 Overview

In this chapter, we will discuss the origin of the $\chi^{(3)}$ nonlinearity of EGFP, where we model the electronic system of the molecule as a two-level system with permanent dipole moments. We also study the nonlinear processes such as FWM, TPA, and Raman scattering that occur during the experiments. Next, we will go through the theory of z-scan technique which helps to characterize the $\chi^{(3)}$ nonlinearity of EGFP, and the method of quantum state tomography, which characterize the created entangled state, and the way of measuring correlations between the photon pairs.

2.2 Nonlinearity

2.2.1 Two-level System Approximation
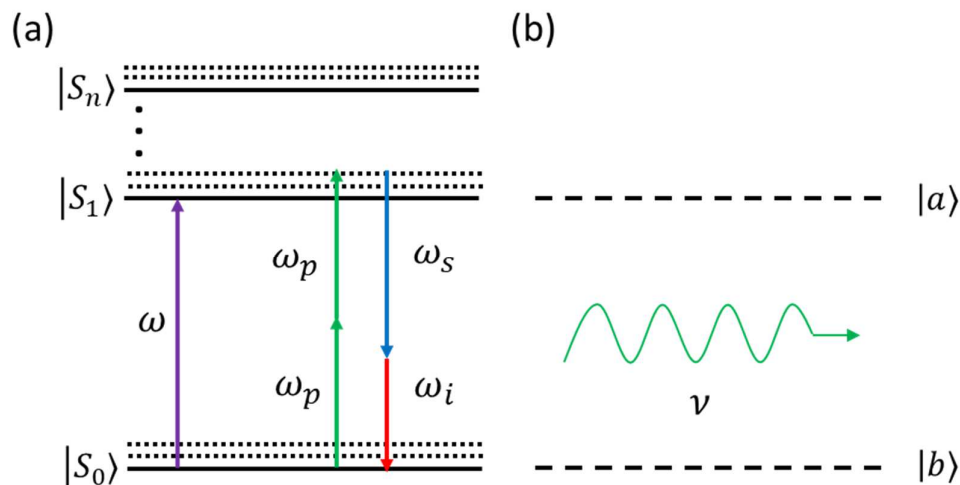
Partial energy-level diagram of EGFP and the two-level system with permanent dipole difference. (a) The relevant partial energy-level diagram of EGFP and the spontaneous four-wave mixing process. The solid lines represent energy levels including the ground state ($|S_0\rangle$), the first excited state ($|S_1\rangle$), and the higher excited states ($|S_n\rangle$). The dotted lines represent vibronic levels. The purple arrow indicates the frequency (ω) between $|S_0\rangle$ and $|S_1\rangle$. The two green arrows with frequencies of ω_p, the blue arrow with a frequency of ω_s, and the red arrow with a frequency of ω_i represent the spontaneous four-wave mixing process where two pump photons (ω_p) are converted to a signal photon (ω_s) and an idler photon (ω_i). (b) The two-level system with permanent dipole moments. The dashed lines represent the two levels ($|a\rangle$) and ($|b\rangle$). The green curved arrow represents the external electric field with a frequency of n interacting with the system.

The nonlinearity of EGFP originates from the modulations of certain electronic states within external electric fields. Specifically, the $\chi^{(3)}$ nonlinearity characterizes the molecule's $\chi^{(3)}$ nonlinear response to an external electric field, which leads to an induced polarization that is proportional to the multiplication of three electric field amplitudes. The strength of the induced polarization is related to the strength of resonance between the electronic states and the electric field; when the field frequency matches the energy gap between two electronic states, the probability that

the electron transits from one to another is much greater, and always result in a large

$\chi^{(3)}$ near that frequency. The scenario is usually the case for $\chi^{(3)}$ nonlinearity in a

multi-level system where the fields drive the electronic states from the ground state to

the highest state via intermediate states. Or it can also describe the $\chi^{(3)}$ nonlinearity

within a two-level system where the fields drive the electronic state up and down, and

then up again. However, in our case, the mechanism is different. According to the

partial energy-level diagram of EGFP as shown in Fig. 2.1a, the ground state ($|S_0\rangle$)

and the first excited state ($|S_1\rangle$) are involved in the SpFWM process. We see that the

signal (ω_s) and idler (ω_i) photons are created by annihilating two pump photons (ω_p).

The permanent dipole moments are the key through the SpFWM process since there is

no intermediate state that serves as a jump pad for pumping the electrons. To study

the physics of the $\chi^{(3)}$ nonlinearity in this case, we model the electronic states of the

EGFP molecule as a two-level system with permanent dipole moments as shown in

Fig. 2.1b that includes all the core concepts which are relevant to the process. Then,

we introduce an electric field with a frequency ($\nu \sim 0.5\omega$) near the two-photon

resonance to perturb the system for analyzing the induced nonlinearity. The

Hamiltonian of the system is given by

$$H_0 = \frac{1}{2}\hbar\omega \begin{pmatrix} 1 & 0 \\ 0 & -1 \end{pmatrix}, \tag{2.1}$$

$$H_{int} = -\mu\, \tilde{E}(t), \tag{2.2}$$

$$H = H_0 + H_{int}. \tag{2.3}$$

Where H_0 is the original Hamiltonian of the system with a resonance frequency of ω, and H_{int} is the interaction Hamiltonian induced by the perturbation of the system with the electric field ($\tilde{E}(t)$). $\mu = er$ is the dipole moment operator with $-e$ as the charge of an electron. To calculate the $\chi^{(3)}$ nonlinearity of the system in respond to the linearly polarized monochromatic field, we define

$$E = xEe^{-ivt} + xE^*e^{ivt}, \tag{2.4}$$

where x is the unit vector along the x-axis, and $E = Ae^{ikz}$. is the field amplitude with A as a constant, k as the wave vector along the z-axis. Therefore,

$$H_{int}(t) = -e\hat{x}(Ee^{-ivt} + E^*e^{ivt}), \tag{2.5}$$

where $\hat{x}$ is the position operator.

We introduce the density matrix formalism [69] to study the evolution of the system since the precise state is obscure. The density matrix of the electronic state of a two-level system is given as

$$\rho(t) = \begin{pmatrix} \rho_{aa} & \rho_{ab} \\ \rho_{ba} & \rho_{bb} \end{pmatrix}, \tag{2.6}$$

where ρ_{aa} and ρ_{bb} represent the probabilities for the system to be found at its energy eigenstate $|a\rangle$ and $|b\rangle$, respectively, ρ_{ab} and ρ_{ba} represent the coherence between the two eigenstates. The Liouville equation for the density matrix is given by

$$\partial_t \rho = (-i/\hbar)[H_0 + H_{int}]\rho - \Gamma\rho, \tag{2.7}$$

where Γ is the decay tensor. In our system, ρ_{aa} decays with a rate of $\gamma_1 = 1/T_1$, where T_1 is the longitudinal relaxation time, whereas ρ_{bb} increases with the same rate due to the decrease of ρ_{aa}. Both ρ_{ab} and ρ_{ba} decay with a rate of $\gamma_2 = 1/T_2$, where T_2 is the transverse relaxation time. By assigning the decay terms to the individual elements of the density matrix, we can obtain the Liouville equation for each component as

$$\partial_t \rho_{aa} = -\frac{i}{h}\left(\mu\rho_{ba} - \rho_{ab}\mu\right)\left(Ee^{-ivt} + E^*e^{ivt}\right) - \gamma_1\rho_{aa}, \tag{2.8}$$

$$\partial_t \rho_{bb} = -\frac{i}{h}\left(\mu\rho_{ab} - \rho_{ba}\mu\right)\left(Ee^{-ivt} + E^*e^{ivt}\right) + \gamma_1\rho_{aa}, \tag{2.9}$$

$$\partial_t \rho_{ab} = -\frac{i}{h}\left(\mu_{aa}\rho_{ab} + \mu\rho_{bb} - \rho_{aa}\mu - \rho_{ab}\mu_{bb}\right)\left(Ee^{-ivt} + E^*e^{ivt}\right) - (i\omega + \gamma_2)\rho_{ab}. \tag{2.10}$$

$$\partial_t \rho_{ba} = -\frac{i}{h}\left(\mu_{bb}\rho_{ba} + \mu\rho_{aa} - \rho_{bb}\mu - \rho_{ba}\mu_{aa}\right)\left(Ee^{-ivt} + E^*e^{ivt}\right) + (i\omega - \gamma_2)\rho_{ba}. \tag{2.11}$$

where we have introduced the dipole moments. Specifically, $\mu_{aa} = -\langle a|e\hat{x}|a\rangle$ and $\mu_{bb} = -\langle b|e\hat{x}|b\rangle$ are the permanent dipole moments on the two states; $\mu_{ab} = -\langle a|e\hat{x}|b\rangle$ and $\mu_{ba} = -\langle b|e\hat{x}|a\rangle$ are the transition dipole moments between the two states. We have chosen the phases of $|a\rangle$ and $|b\rangle$ to allow $\mu_{ab} = \mu_{ba}$, so that we can use a single notation (μ) to represent both transition dipole moments. To remove the redundancy in the analysis, we introduce $\rho = \rho_{aa} - \rho_{bb}$, since $\rho_{aa} + \rho_{bb} = 1$. Therefore, we can obtain

$$\partial_t \rho = -2i\Omega_1 \left(\rho_{ba} - \rho_{ab}\right)e^{-ivt} - 2i\Omega_1^* \left(\rho_{ba} - \rho_{ab}\right)e^{ivt} - \gamma_1(\rho + 1), \tag{2.12}$$

$$\partial_t \rho_{ab} = i\Omega_1 \rho e^{-ivt} + i\Omega_1^* \rho e^{ivt} - i\Omega_2 \rho_{ab} e^{-ivt} - i\Omega_2^* \rho_{ab} e^{ivt} - (i\omega + \gamma_2)\rho_{ab}. \tag{2.13}$$

where, $\Omega_1 = \frac{\mu E}{\hbar}$ and $\Omega_2 = \frac{(\mu_{aa} - \mu_{bb})E}{\hbar}$ are Rabi frequencies. Since the system is driven by the field with a frequency of v, we can expand ρ and ρ_{ab} into Fourier series with frequencies of integer multiples of v as

$$\rho = \rho_0 + \left[\sum_{n=1}^{\infty} \rho_n e^{invt} + \text{C. C.}\right], \tag{2.14}$$

$$\rho_{ab} = \eta_0 + \left[\sum_{n=1}^{\infty} \eta_n e^{invt} + \text{C. C.}\right]. \tag{2.15}$$

By plugging Eq. 2.14 and Eq. 2.15 into Eq. 2.12 and Eq. 2.13, we will see how each Fourier amplitude will evolve over time as

$$\partial_t \rho_0 = -2i\Omega_1 \left(\eta_{-1}^* - \eta_1\right) - 2i\Omega_1^* \left(\eta_1^* - \eta_{-1}\right) - \gamma_1(\rho_0 + 1), \tag{2.16}$$

$$\partial_t \rho_1 = -2i\Omega_1 \left(\eta_{-2}^* - \eta_2\right) - 2i\Omega_1^* \left(\eta_0^* - \eta_0\right) - (iv + \gamma_1)\rho_1, \tag{2.17}$$

$$\partial_t \rho_2 = -2i\Omega_1 \left(\eta_{-3}^* - \eta_3\right) - 2i\Omega_1^* \left(\eta_{-1}^* - \eta_1\right) - (i2v + \gamma_1)\rho_2, \tag{2.18}$$

$$\partial_t \eta_{-2} = i\Omega_1 \rho_1^* + i\Omega_1^* \rho_3^* - i\Omega_2 \eta_{-1} - i\Omega_2^* \eta_{-3} + \left(-i\omega + i2v - \gamma_2\right)\eta_{-2}, \tag{2.19}$$

$$\partial_t \eta_{-1} = i\Omega_1 \rho_0 + i\Omega_1^* \rho_2^* - i\Omega_2 \eta_0 - i\Omega_2^* \eta_{-2} + \left(-i\omega + iv - \gamma_2\right)\eta_{-1}, \tag{2.20}$$

$$\partial_t \eta_0 = i\Omega_1 \rho_1 + i\Omega_1^* \rho_1^* - i\Omega_2 \eta_1 - i\Omega_2^* \eta_{-1} + \left(-i\omega - \gamma_2\right)\eta_0, \tag{2.21}$$

$$\partial_t \eta_1 = i\Omega_1 \rho_2 + i\Omega_1^* \rho_0 - i\Omega_2 \eta_2 - i\Omega_2^* \eta_0 + \left(-i\omega - iv - \gamma_2\right)\eta_1, \tag{2.22}$$

$$\partial_t \eta_2 = i\Omega_1 \rho_3 + i\Omega_1^* \rho_1 - i\Omega_2 \eta_3 - i\Omega_2^* \eta_1 + \left(-i\omega - i2v - \gamma_2\right)\eta_1. \tag{2.23}$$

The Fourier amplitudes are useful for obtaining the $\chi^{(3)}$ nonlinearity of the system. We first discuss the long-time response of the system to the field, when the interaction can lead to a steady-state solution in the given time frame; this reveals the $\chi^{(3)}$ nonlinearity of the system in response to a continuous-wave electric field. We then discuss the instantaneous response of the system to the field, when the state has just started evolving; this clarifies the nonlinearity of the system in response to a pulsed electric field. The following formalisms assume that the impact of higher-order nonlinearities to the Fourier amplitudes is negligible when comparing to the impact of lower-order nonlinearities; the amplitude of the electric field shouldn't break its upper limit. Therefore, we can group the selected Fourier amplitudes into four buckets, based on the order of perturbations as shown in Fig. 2.2 and Fig. 2.3. The perturbations of the first-order amplitudes ($\eta_{\pm 1}$ and their conjugates) originate from the interactions between the electric field and the 0th amplitude (ρ_0), as indicated by the arrows. Similarly, the perturbations of the second-order (third-order) amplitudes arise from the interactions between the field and the first-order (second-order) amplitudes. We segment the perturbation processes based on whether they involve the permanent dipole moments. By calculating the response of the amplitudes in a proper sequence from lower order to higher order, we can obtain the third-order polarization of the system that is induced by the electric field, and then find out the $\chi^{(3)}$ nonlinearity.
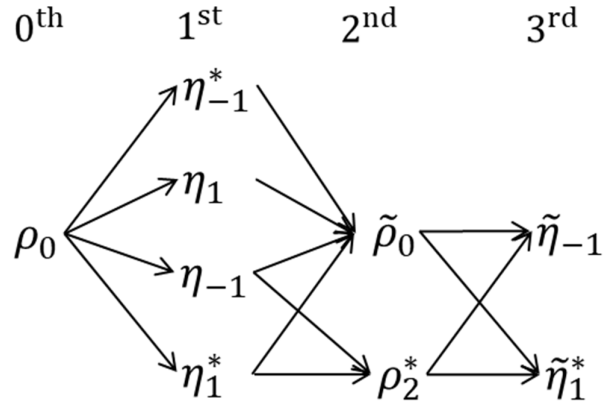
Figure 2. 2

The perturbation of Fourier amplitudes. Fourier amplitudes that are driven by the electric field on different orders, without the contribution of the permanent dipole moments. The arrows indicate where the processes occur. The straight arrows represent the processes induced by the transition dipole moments, the dashed arrows represent the processes induced by the permanent dipole moments.
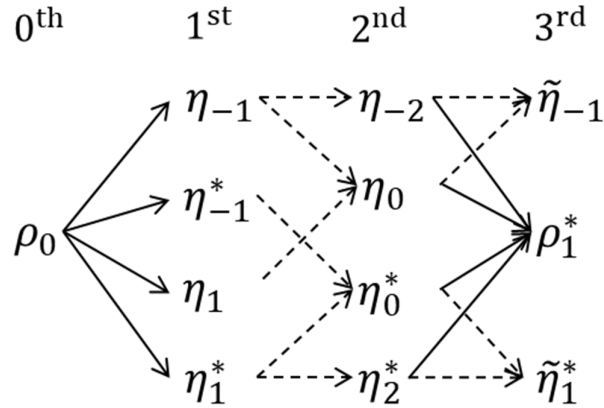
Figure 2. 3

The perturbation of Fourier amplitudes. Fourier amplitudes that are driven by the external field, with the contribution of both the transition dipole moments and the permanent dipole moments.

A. Long-time response

When the electric field is off, the system is in the ground state, where $\rho_0 = 1$, and all the other Fourier amplitudes are 0. When the field is on, we first focus on solving the first-order Fourier amplitudes, which are $\eta_{\pm 1}$ and their conjugates. If we plug $\rho_0 =$

1 into [Eq. 20](#) and [Eq. 22](#), and then neglect the higher order terms, we can solve the differential equations for $\eta_{\pm 1}$ as

$$\eta_{-1} = \frac{-i\Omega_1}{i(\omega - v) + \gamma_2}\left[1 - e^{(-i\omega + iv - \gamma_2)t}\right], \tag{2.24}$$

$$\eta_1 = \frac{-i\Omega_1^*}{i(\omega + v) + \gamma_2}\left[1 - e^{(-i\omega - iv - \gamma_2)t}\right]. \tag{2.25}$$

which will eventually reach the steady-state solution when $t \gg T_2$ as

$$\eta_{-1}(t \; ? \; T_2) = \frac{-i\Omega_1}{i(\omega - v) + \gamma_2}, \tag{2.26}$$

$$\eta_1(t \; ? \; T_2) = \frac{-i\Omega_1^*}{i(\omega + v) + \gamma_2}. \tag{2.17}$$

Next, we focus on solving the second-order Fourier amplitudes, which include $\tilde{\rho}_0$, ρ_2, η_{-2}, η_0, and η_2, where $\tilde{\rho}_0$ is the perturbation of ρ_0. If we plug [Eq. 2.26](#) and [Eq. 2.27](#) into Eqs. [2.16](#), [2.18](#), [2.19](#), [2.21](#), and [2.23](#), meanwhile neglecting the higher-order terms, we can obtain

$$\tilde{\rho}_0(t \gg T_1) = \frac{-2\left[i\Omega_1\left(\eta_{-1}(t \; ? \; T_2) - \eta_1(t \; ? \; T_2)\right) + \text{C.C.}\right]}{\gamma_1}, \tag{2.28}$$

$$\rho_2(t \gg T_1) = \frac{-2\left[i\Omega_1^*\left(\eta_{-1}(t \; ? \; T_2) - \eta_1(t \; ? \; T_2)\right)\right]}{i2v + \gamma_1}, \tag{2.29}$$

$$\eta_{-2}(t \gg T_2) = \frac{-i\Omega_2\,\eta_{-1}(t \; ? \; T_2)}{i(\omega - 2v) + \gamma_2}, \tag{2.30}$$

$$\eta_0(\text{t} \gg T_2) = \frac{-i\Omega_2\,\eta_1(t\,?\,\,T_2) - i\Omega_2^*\,\eta_{-1}(t\,?\,\,T_2)}{i\omega + \gamma_2},$$ (2.31)

$$\eta_2(\text{t} \gg T_2) = \frac{-i\Omega_2^*\,\eta_1(t\,?\,\,T_2)}{i(\omega + 2v) + \gamma_2},$$ (2.32)

Finally, we focus on solving the third-order Fourier amplitudes, which include ρ_1, and $\tilde{\eta}_{\pm 1}$, where $\tilde{\eta}_{\pm 1}$ are the perturbations of $\eta_{\pm 1}$. These are the Fourier amplitudes that directly contribute to the induced third-order polarization, and therefore the $\chi^{(3)}$ nonlinearity as given in the relation

$$\chi^{(1)}(v) = \frac{N\left(\eta_{-1} + \eta_1^*\right)\mu}{\varepsilon_0 E},$$ (2.23)

$$\chi_{1111}^{(3)}(v = v + v - v) = \frac{N\left[\frac{1}{2}\beta_0^*\left(\mu_{aa} - \mu_{bb}\right) + \tilde{\eta}_{-1}\mu + \tilde{\eta}_1^*\mu\right]}{3\varepsilon_0 EEE^*},$$ (2.34)

where N is the density of the molecule, and P is the induced polarization by each molecule. The detailed solution of $\chi^{(3)}$ is shown in the Appendix A.

B. Instantaneous Response

As the term suggests, the difference between the instantaneous response and the long-term response is that the system hasn't reached a steady state in a short time frame. Therefore, we should not use the steady-state solutions of the lower-order perturbations for predicting the solutions of the higher-order perturbations. Instead, we rely on the time-dependent Fourier amplitudes for calculations starting from the first-order perturbations to the third-order perturbations. Therefore, we plug

and Eq. 2.25 into Eq. 2.16, 2.18, 2.19, 2.21, and 2.23. By neglecting the higher-order terms, we obtain

$$\partial_t \overset{\circ}{\tilde{\rho}}_0 = -2i\Omega_1\left(\eta_{-1}^* - \eta_1\right) - 2i\Omega_1^*\left(\eta_1^* - \eta_{-1}\right) - \gamma_1(\overset{\circ}{\tilde{\rho}}_0), \tag{2.35}$$

$$\partial_t \rho_2 = -2i\Omega_1^*\left(\eta_{-1}^* - \eta_1\right) - \left(i2v + \gamma_1\right)\rho_2, \tag{2.36}$$

$$\partial_t \eta_{-2} = -i\Omega_2 \eta_{-1} + \left(-i\omega + i2v - \gamma_2\right)\eta_{-2}, \tag{2.37}$$

$$\partial_t \eta_0 = -i\Omega_2 \eta_1 - i\Omega_2^* \eta_{-1} + \left(-i\omega - \gamma_2\right)\eta_0, \tag{2.38}$$

$$\partial_t \eta_2 = -i\Omega_2^* \eta_1 + \left(-i\omega - i2v - \gamma_2\right)\eta_1. \tag{2.39}$$

Here, we solve for Eq. 2.35 as an example for demonstrating the method.

$$\partial_t \overset{\circ}{\tilde{\rho}}_0 = -2i\Omega_1\left(\eta_{-1}^* - \eta_1\right) - 2i\Omega_1^*\left(\eta_1^* - \eta_{-1}\right) - \gamma_1(\overset{\circ}{\tilde{\rho}}_0) = C_1(t) + C_2 \overset{\circ}{\tilde{\rho}}_0 \tag{2.40}$$

where C_1 is a function of t, and C_1 is a constant. Assume $\tilde{\rho}_0 = F(t)e^{C_2 t}$, where F is a function of t, then

$$\dot{F} = C_1(t)e^{-C_2 t}, \tag{2.41}$$

Therefore, the integration on F will provide the solution for $\tilde{\rho}_0$, which is given as

$$\tilde{\rho}_0 = \sum_{m=\pm 1}\sum_{n=\pm 1}\frac{-2|\Omega_1|^2 e^{D(0,-\Gamma_1)t}}{D(m\omega + nv, \Gamma_2)} \times \{G[D(m\omega + nv, \Gamma_2 - \Gamma_1)] - G[D(-2v, -\Gamma_1)]\}, \tag{2.42}$$

where function $G(x)$ is defined as $G(x) = -(e^{-xt} - 1)/x$, and function $D(x, y)$ is defined as $D(x, y) = ix + y$. The same method can be used to solve for the other second-order Fourier amplitudes ρ_2, η_{-2}, η_0, and η_2. The results are

$$\rho_2 = \sum_{m=\pm1} \frac{-2|\Omega_1|^2 e^{D(-2\nu,-\Gamma_1)t}}{D(m\omega+\nu,\Gamma_2)} \times \{G[D(m\omega-\nu,\Gamma_2-\Gamma_1)] - G[D(-2\nu,-\Gamma_1)]\}, \quad (2.43)$$

$$\eta_{-2} = \frac{-\Omega_1\Omega_2 e^{D(-\omega+2\nu,-\Gamma_2)t}}{D(\omega-\nu,\Gamma_2)} \times \{G[D(\nu,0)] - G[D(-\omega+2\nu,-\Gamma_2)]\}, \quad (2.44)$$

$$\eta_0 = \frac{\Omega_1^*\Omega_2 e^{D(-\omega,-\Gamma_2)t}}{D(\omega+\nu,\Gamma_2)} \times \{G[D(\nu,0)] - G[D(-\omega,-\Gamma_2)]\} + \frac{\Omega_2^*\Omega_1 e^{D(-\omega,-\Gamma_2)t}}{D(\omega-\nu,\Gamma_2)}$$

$$\times \{G[D(-\nu,0)] - G[D(-\omega,-\Gamma_2)]\}, \quad (2.45)$$

$$\eta_2 = \frac{-\Omega_1^*\Omega_2^* e^{D(-\omega-2\nu,-\Gamma_2)t}}{D(\omega+\nu,\Gamma_2)} \times \{G[D(-\nu,0)] - G[D(-\omega-2\nu,-\Gamma_2)]\}. \quad (2.46)$$

Finally, by plugging the second-order Fourier amplitudes into Eq. 2.17, Eq. 2.20, and

Eq. 2.22, we obtain

$$\partial_t \rho_1 = -2i\Omega_1\left(\eta_{-2}^* - \eta_2\right) - 2i\Omega_1^*\left(\eta_0^* - \eta_0\right) - (i\nu + \gamma_1)\rho_1, \quad (2.47)$$

$$\partial_t \tilde{\eta}_{-1} = i\Omega_1\tilde{\rho}_0 + i\Omega_1^*\rho_2^* - i\Omega_2\eta_0 - i\Omega_2^*\eta_{-2} + (-i\omega + i\nu - \gamma_2)\eta_{-1}, \quad (2.48)$$

$$\partial_t \tilde{\eta}_1 = i\Omega_1\rho_2 + i\Omega_1^*\tilde{\rho}_0 - i\Omega_2\eta_2 - i\Omega_2^*\eta_0 + (-i\omega - i\nu - \gamma_2)\eta_1, \quad (2.49)$$

The solutions for ρ_1 and $\tilde{\eta}_{\pm1}$ are shown in the Appendix. B. As a result, we can

calculate the instantaneous $\chi^{(3)}$ nonlinearity of the system in respond to the external

field by using Eq. 2.34.

Parameter	Symbol	Value
Longitudinal relaxation time	T_1	1 ns
Transverse relaxation time	T_2	10 fs

Transition dipole moments	μ	10 Debye
Permanent dipole moment	$\Delta\mu$	20 Debye
Resonant frequency	ω	4.2×10^{15} Hz
Molecule density	N	2.1×10^{22} m^{-3}
Refractive index	n	1
Pulse duration	t	200 fs

Table 2.1 A summary of the parameters used in the estimation of $\chi^{(3)}$ nonlinearity.

As shown in the Table. 2.1 are the parameters that we used in the model. We choose the value of T_1 as 1ns because of the nanosecond lifetime of $|S_1\rangle$. We choose the value of T_2 as 10 fs by analyzing the extinction coefficient of EGFP [52]. The values of μ and $\Delta\mu$ are estimated around 10 Debye, and 20 Debye based on Wan's work [70]. ω is approximated as 4.2×10^{15} Hz corresponding to a wavelength of 450 nm regarding to the two-photon absorption spectra of EGFP [52]. N is obtained according to the EGFP solution with a molar concentration of 25 mM in phosphate buffered saline. n is assumed as 1. t is chosen as 200 fs corresponding to our mode-locked regenerative amplifier (Coherent Inc., RegA-9000 seeded by Mira-900 and pumped by Verdi-10) which generates pulses with a duration of 200 fs.
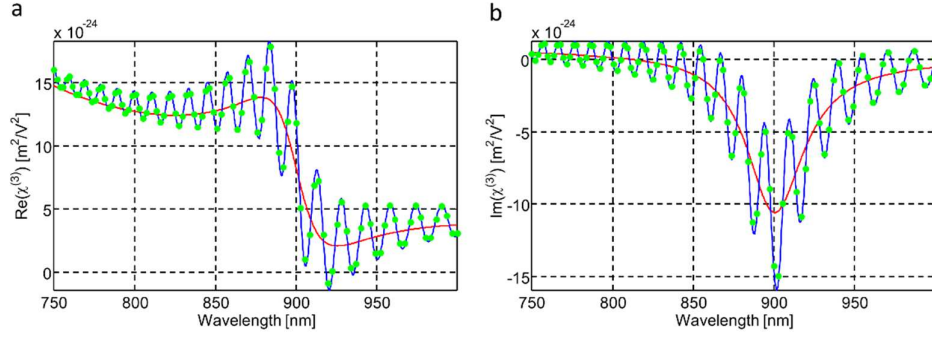
Figure 2. 4

Spectrum of $\chi^{(3)}$. (a) Real part of $\chi^{(3)}$ (b) Imaginary part of $\chi^{(3)}$. $E = 1 \times 10^5$ V/m. The red line represents the result of long-time response. The blue line represents the result from the instantaneous response. The green dot represents the numerical simulation on the instantaneous response.

We plot the $\chi^{(3)}$ nonlinearity of the system in two cases, as well as the simulated result for the instantaneous response, in Fig. 2.4a and Fig. 2.4b, demonstrating the real and imaginary parts, respectively. The results of the long-time and instantaneous responses are obtained directly from the analytical solutions, the result of the simulation is obtained by numerically integrating the Liouville equations of Fourier amplitudes over t. From the figure, we see that two types of processes contribute to the $\chi^{(3)}$ nonlinearity; the processes without involving the permanent dipole moment (see Fig. 2.2) form the base line, which is an extension of the $\chi^{(3)}$ curve near its one-photon resonance; the processes involving the permanent dipole moment (see Fig. 2.3) add the twist on top of the base line, which is the main reason for $\chi^{(3)}$ nonlinearity near two-photon resonance. The difference between the long-time and instantaneous responses originates from the fast oscillating term in Eq. 2.24, and Eq.

2.25. These oscillations are intrinsic and noticeable in the short-time scale, its amplitude is dependent on μ and $\Delta\mu$, and its phase is a function of vt.

As mentioned before, this formalism is valid when the amplitude of the electric field is lower than the upper limit. This condition holds when 1 is much greater than the first-order Fourier amplitudes, and meanwhile the first-order Fourier amplitudes are much greater than the second-order Fourier amplitudes, which are much greater than the third-order Fourier amplitudes. Therefore, with the provided parameters, the condition is

$$1 \gg \frac{\Omega_2}{\omega - v} \rightarrow E \ll 3.3 \times 10^9 \, Vm^{-1}, \tag{2.50}$$

when the choice of frequency is away from the two-photon resonance, and

$$1 \gg \frac{\Omega_2}{\gamma_2} \rightarrow E \ll 1.6 \times 10^8 \, Vm^{-1}, \tag{2.51}$$

when it's near the two-photon resonance. The reason for the difference between the two upper limits is that as the frequency approaches the two-photon resonance, the nonlinearity becomes stronger, therefore the upper limit falls lower. Fig. 2.5a and Fig. 2.5b show the result with $E = 1 \times 10^8$ V/m, and Fig. 2.6a and Fig. 2.6b show the result with $E = 5 \times 10^8$ V/m. It's obvious that as the amplitude of the electric field increases, the formalism becomes invalid sequentially from near the two-photon resonance to away from it.
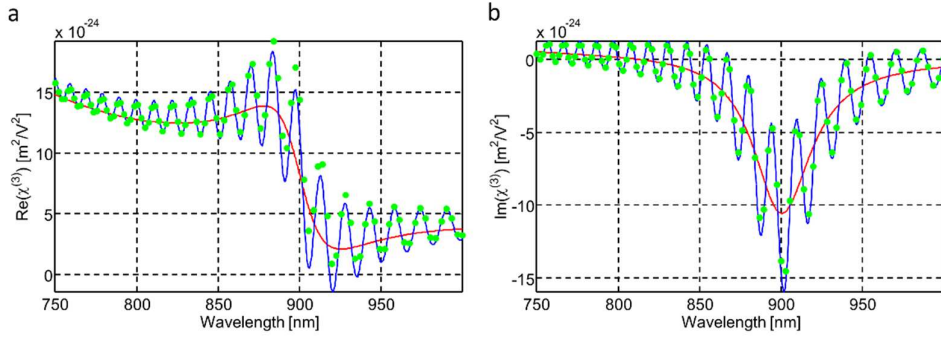
Figure 2. 5

Spectrum of $\chi^{(3)}$. (a) Real part of $\chi^{(3)}$ (b) Imaginary part of $\chi^{(3)}$. $E = 1 \times 10^8$ V/m. The red line represents the result of long-time response. The blue line represents the result from the instantaneous response. The green dot represents the numerical simulation on the instantaneous response.
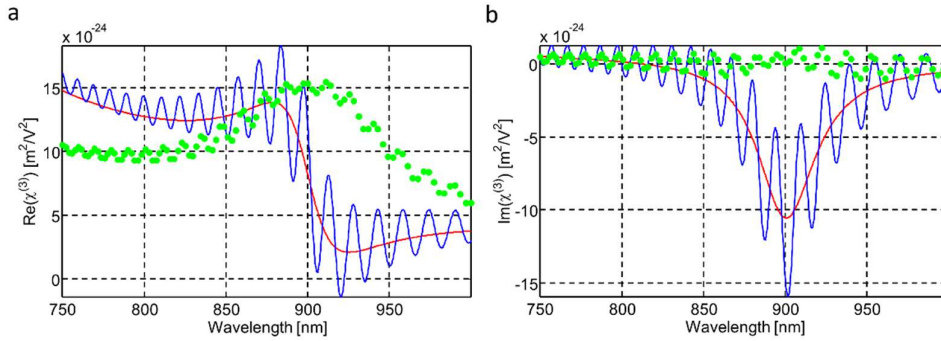
Figure 2. 6

Spectrum of $\chi^{(3)}$. (a) Real part of $\chi^{(3)}$ (b) Imaginary part of $\chi^{(3)}$. $E = 5 \times 10^8$ V/m. The red line represents the result of long-time response. The blue line represents the result from the instantaneous response. The green dot represents the numerical simulation on the instantaneous response.

The above example discusses the case when $T_2 \ll t \ll T_1$, while the formalism also covers the cases when $T_2 \sim t$ or $T_2 \gg t$. This is worth mentioning since T_2 varies from femtoseconds to picoseconds as reported in different works. Fig. 2.7a and Fig. 2.7b exhibit the $\chi^{(3)}$ in its real and imaginary components with $T_2 = 100$ fs, and other parameters unchanged. Comparing them with Fig. 2.4a and Fig. 2.4b, we see

that for the long-time response, the curves' peak amplitudes have increased, and their widths have shrunk. The change in the line shape originates from the enhancement of two types of resonances; the one-photon resonance sharpens the peak (dip) of the curve near 450 nm, which lowers the baseline, and similarly, the two-photon resonance sharpens the peak (dip) near 900 nm and lowers the baseline as well. We also observe that for the instantaneous response, the blue curves follow the same trend as the red curves, due to the resonance enhancements. However, the curves oscillate vigorously in the off-resonance region since the decays on the density matrix elements are less obvious in a shorter time frame. What's more, the amplitude of the oscillation tends to increase after T_2 has passed a certain threshold as shown in Fig. 2.7c and Fig. 2.7d, where we fix the wavelength at 785 nm. This is because the induced nonlinear polarization can continuously build up without experiencing too much decay in the time frame as T_2 increases.
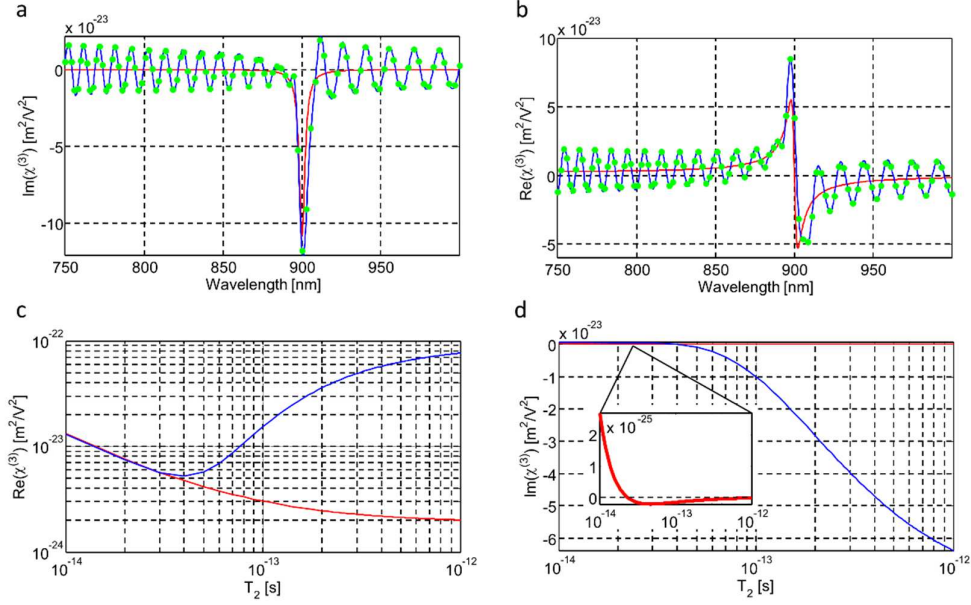
Figure 2. 7

Effects of T_2 on the spectrum of $\chi^{(3)}$. (a) Real part of $\chi^{(3)}$ with $T_2 =100$ fs. (b) Imaginary part of $\chi^{(3)}$ with $T_2 =100$ fs. (c) Real part of $\chi^{(3)}$ v.s. T_2 at 785 nm. (d) Imaginary part of $\chi^{(3)}$ v.s. T_2 at 785 nm. Inset: an enlarged figure for the long-time-response curve. The red line represents the result of long-time response. The blue line represents the result from the instantaneous response. The green dot represents the numerical simulation on the instantaneous response.

The presence of such nonlinear dispersion points towards the possibility of using naturally occurring fluorescent proteins as a medium for FWM experiments, in contrast to the engineered optical devices. What's more, with a pulsed laser, we can target the frequency region with a higher nonlinear response by referencing the oscillating pattern of the instantaneous response.

2.2.2 Four-wave Mixing

We utilize the $\chi^{(3)}$ nonlinearity of EGFP for generating photon pairs. The essential experiments are stimulated and spontaneous FWM processes. In this section, we will

gain a thorough understanding of the FWM processes. FWM process is an intermodulation phenomenon in nonlinear optics. Within the process, two or three wavelengths interact with each other to produce two or one new wavelengths while the energy and momentum of the system are conserved. In our case, for the StFWM, two pump beams and one signal beam interact in the $\chi^{(3)}$ medium to enhance the intensity of signal beam, create a new idler beam, and reduce the energy of two pump beams. We will first investigate the degenerate StFWM, where the two pump beams and one signal beam are obtained from the same laser. For the SpFWM, two pump beams interact in the $\chi^{(3)}$ medium to create both the signal and idler beams and reduce the intensity of two pump beams. We will investigate the case with continuous-wave pump beams, and then the case with pulsed pump beams. Note that in the following derivations, since the self- and cross-phase modulation processes are not strong enough to change the frequency spectrum of the pump, these two processes are ignored.

2.2.2.1   Degenerate stimulated four-wave mixing

In this section, we investigate the degenerate stimulated four-wave mixing process as described in the above section. Pump, signal, and idler fields are assumed to be plane waves propagating along axes (z_{p1}, z_{p2}, z_s and z_i) near the z-axis with the same frequency ω_0, and so that their wave vectors all equal $k_0 = \frac{\omega_0}{c}$. Therefore, the two pumps, signal and idler fields can be written as

$$E_{p1} = A_{p1}e^{i(k_0 z_{p1} - \omega_0 t)}, \qquad (2.52)$$

$$E_{p2} = A_{p2}e^{i(k_0 z_{p2} - \omega_0 t)}, \qquad (2.53)$$

$$E_s = A_s e^{i(k_0 z_s - \omega_0 t)}, \qquad (2.54)$$

$$E_i = A_i e^{i(k_0 z_i - \omega_0 t)}, \qquad (2.55)$$

Where the subscripts denote the four fields, A_{p1}, A_{p2}, A_s and A_i are the field amplitudes. We can assume the entrance surface of the sample is set at $z = 0$ and the exit surface of the sample is set as $z = L$. Since the idler field is generated inside the sample, in this case, the boundary conditions for the signal and idler fields are given as

$$A_s(0) = A_s \neq 0 \qquad (2.56)$$

$$A_i(0) = 0. \qquad (2.57)$$

Since the pumps are strong, we can assume their amplitudes (A_{p1}, A_{p2}) are constant during the whole process. During the FWM process, the variations of signal and idler fields are given as

$$\frac{dA_s}{dz} = i\Gamma A_i^*, \qquad (2.58)$$

$$\frac{dA_i}{dz} = i\Gamma A_s^*, \qquad (2.59)$$

where $\Gamma = \frac{3k_0 \chi^{(3)}}{2} A_{p1} A_{p2}$. Therefore, by applying the boundary conditions, Eq. 2.58 and Eq. 2.59 are solved as

$$A_s(z) = \frac{A_s(0)}{2}\left(e^{\Gamma z} + e^{-\Gamma z}\right), \tag{2.60}$$

$$A_i(z) = i\frac{A_s(0)}{2}\left(e^{\Gamma z} - e^{-\Gamma z}\right). \tag{2.61}$$

As expected, Eq. 2.60 and Eq. 2.61 show that the stimulated four-wave mixing can provide gains to both signal and idler fields. At the exit surface of the sample where $z = L$, the amplitudes of signal and idler become

$$A_s(L) = \frac{A_s(0)}{2}\left(e^{\Gamma L} + e^{-\Gamma L}\right), \tag{2.62}$$

$$A_i(L) = i\frac{A_s(0)}{2}\left(e^{\Gamma L} - e^{-\Gamma L}\right). \tag{2.63}$$

Since the effective length of the sample (L) is short, we can approximate the amplitudes as

$$A_s(L) \approx A_s(0)\left(1 + \Gamma^2 L^2\right), \tag{2.64}$$

$$A_i(L) \approx iA_s(0)\Gamma L. \tag{2.65}$$

We can then obtain the four-wave mixing efficiency as $\frac{\text{Intensity of idler field}}{\text{Intensity of signal field}} = \frac{|A_i(L)|^2}{|A_s(L)|^2} \approx \Gamma^2 L^2$. The FWM efficiency is usually used as a quality factor of how good the alignment is. In summary, StFWM is useful for an estimation of the $\chi^{(3)}$-nonlinearity of the sample. In addition, since the signal and idler fields are strong enough for viewing on an IR viewer card, StFWM also provides a convenient way for the alignment of the experimental setup of SpFWM where the signal and idler fields are on the single photon level.

2.2.2.2   Spontaneous four-wave mixing

SpFWM is essential for the photon-pair generation in this thesis. In this section, we will discuss SpFWM process in details. In contrast with StFWM, the signal beam is blocked. Instead, two pump beams are used to generate both signal and idler fields [71]. Here, we will work in the scheme as shown in Fig. 2.8, note that the entrance surface of the sample is now placed at $z = -L/2$ and the exit surface is then $L/2$. Two pump beams propagate in the vertical plane from $z = -\frac{L}{2}$ to $z = \frac{L}{2}$. The generated signal and idler beams are detected along $\vec{z_s}$ and $\vec{z_i}$ directions (that satisfy the phase matching condition) in the horizontal plane. In the following derivations, two scenarios are studied; (i) the pump fields are continuous waves (CW), (ii) the pump fields are pulsed wave-packet.
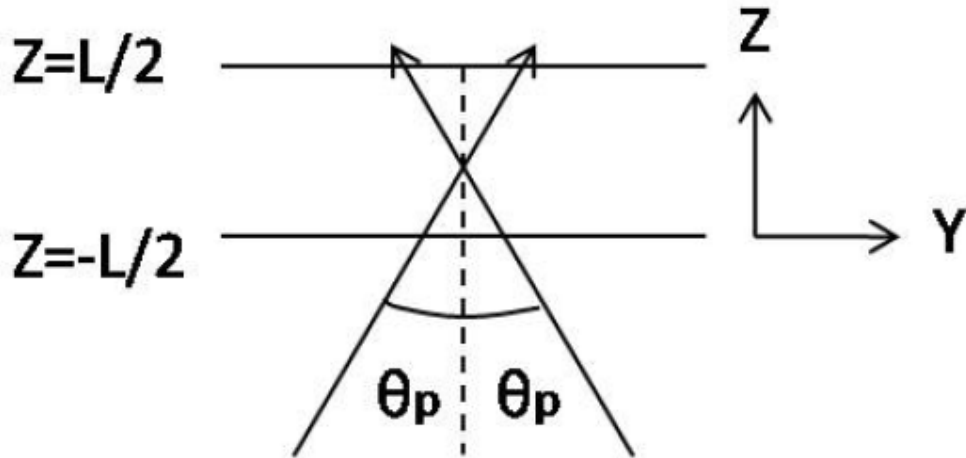
Figure 2. 8

Forward four-wave mixing geometry.

2.2.2.2.1 Continuous-wave approach

In the CW approach, we start by modeling the pump field (E_p) as a spatial Gaussian with a beam width of r_0. The pump field is propagating along the z-axis with a frequency of ω_0:

$$E_p = A_p e^{\frac{-(x^2+y^2)}{2r_0^2}} e^{i\omega_0\left(\frac{z}{c}-t\right)},$$

(2.66)

Here, A_p is the amplitude of the field. Note that in the real experiment, we can measure the pump power but not the amplitude (A_p). Since the power and the amplitude are related, we can write A_p as a function of the pump power. To do this, we can consider an arbitrary time of T, during which the energy of the pump field is given by

$$\varepsilon_0 \int\limits_{-\infty}^{\infty} dx \int\limits_{-\infty}^{\infty} dy \int\limits_{0}^{cT} dz E_p^* E_p = n\hbar\omega_0,$$

(2.67)

where c is the speed of light, n is number of photons within the space. On the left-hand side of the equation is the energy of the electric field, while on the right-hand side of the equation is the same amount of energy but represented by the number of photons. Based on the Eq. 2.67, A_p is solved as

$$A_p = \sqrt{\frac{n\hbar\omega_0}{\varepsilon_0 \pi r_0^2 cT}}.$$

(2.68)

In [Eq. 2.68](#), $\pi r_0^2 cT$ can be viewed as the volume that contains n photons. Note that the electric field is calculated in the vacuum instead of in the sample because the effect of the refractive index of the sample $(n = 1 + 0.5\chi^{(1)} \sim 1)$ can be neglected.

In the following discussion, we can assume the pump fields are plane waves, and then introduce the spatial Gaussian profile as correction terms.

We can start by writing down the analytical expressions of the four fields. In contrast with the example in degenerate StFWM, the generated signal and idler are multicolor instead of monochromatic even though the pump fields haven't changed, because the signal is not defined prior to entering the sample. The four fields are

$$E_s = \int_{-\infty}^{\infty} d\omega_s A_s(\omega_s) e^{i(k_s z_s - \omega_s t)}, \tag{2.69}$$

$$E_i = \int_{-\infty}^{\infty} d\omega_i A_i(\omega_i) e^{i(k_i z_i - \omega_i t)}, \tag{2.70}$$

$$E_{p1} = A_p e^{i(k_0 z_{p1} - \omega_0 t)}, \tag{2.71}$$

$$E_{p2} = A_p e^{i(k_0 z_{p2} - \omega_0 t)}, \tag{2.72}$$

where, $z_s = \frac{z}{\cos\theta_s}$, $z_i = \frac{z}{\cos\theta_i}$, and $z_p = \frac{z}{\cos\theta_p}$ are the principle axes for each beam, $k_s = \frac{\omega_s}{c}$ and $k_i = \frac{\omega_i}{c}$ are the wave vectors. We now consider the amplitude of each electric field as a field operator in Hilbert space [72]. The propagations of these field operators along z-axis are governed by Maxwell equations,

$$\frac{\partial \hat{A}_s(\omega_s)}{\partial z} = \frac{ik_s}{2\cos\theta_s}\chi^{(1)}\hat{A}_s(\omega_s) + \frac{3ik_s\cos^2\theta_p}{2\cos\theta_s}\chi^{(3)}A_p^2\hat{A}_i^\dagger(2\omega_0 - \omega_s)e^{i\Delta kz}, \qquad (2.73)$$

$$\frac{\partial \hat{A}_i(\omega_i)}{\partial z} = \frac{ik_i}{2\cos\theta_i}\chi^{(1)}\hat{A}_i(\omega_i) + \frac{3ik_i\cos^2\theta_p}{2\cos\theta_i}\chi^{(3)}A_p^2\hat{A}_s^\dagger(2\omega_0 - \omega_i)e^{i\Delta kz}, \qquad (2.74)$$

$$\Delta k = \frac{2k_0}{\cos\theta_p} - \frac{k_i}{\cos\theta_i} - \frac{k_s}{\cos\theta_s}. \qquad (2.75)$$

The hats in the Eq. 2.73 and Eq. 2.74 indicate that they are field operators in Hilbert space. The evolvements of field operators are induced by two processes; (i) self-phase modulation (former term), which is a first-order effect, (ii) four-wave mixing process (latter term), which is a third-order effect. The self-phase modulation can be eliminated if we use the following transformations,

$$\hat{A}_s(\omega_s, x, y, z) = \hat{A}_s^0(\omega_s)e^{\frac{ik_s\chi^{(1)}z}{2\cos\theta_s}}, \qquad (2.76)$$

$$\hat{A}_i(\omega_i, x, y, z) = \hat{A}_i^0(\omega_i)e^{\frac{ik_i\chi^{(1)}z}{2\cos\theta_i}}. \qquad (2.77)$$

We define $\Upsilon_1 = \frac{3ik_s\chi^{(3)}\cos^2\theta_p}{2\cos\theta_s}$, $\Upsilon_2 = \frac{3ik_i\chi^{(3)}\cos^2\theta_p}{2\cos\theta_i}$ and $\Upsilon = \frac{3ik_0\chi^{(3)}}{2}$. Since the angles of the beams are small ($\theta_p \approx \theta_s \approx \theta_i \approx 0$) and the wavelength of the beams are close ($k_0 \approx k_s \approx k_i$), we can use the constant $\Upsilon \approx \Upsilon_1 \approx \Upsilon_2$ to replace Υ_1 and Υ_2 in the equations. Although $\chi^{(3)}$ is wavelength dependent, we can assume that $\chi^{(3)}$ is constant because we can only detect a selected combination of signal and idler fields in the narrow bandwidth regime in the experiment. Applying the phase-matching condition $2k_0 = k_s + k_i$, the equations are arranged to become

$$\frac{\partial \tilde{A}_s^0(\omega_s)}{\partial z} \approx \Upsilon \tilde{A}_i^0 (2\omega_0 - \omega_s) A_p^2, \tag{2.78}$$

$$\frac{\partial \tilde{A}_i^0(\omega_i)}{\partial z} \approx \Upsilon^* \tilde{A}_s^0 (2\omega_0 - \omega_i) A_p^2. \tag{2.79}$$

We see that the equations have become much simpler. Now we can insert the spatial Gaussian profile to the three fields as correction terms. Eq. 2.78 and Eq. 2.79 become

$$\frac{\partial \tilde{A}_s^0(\omega_s)}{\partial z} \approx \Upsilon \tilde{A}_i^0 (2\omega_0 - \omega_s) A_p^2 e^{\frac{-2z^2\left(\tan^2\theta_s + \tan^2\theta_p\right)}{r_0^2}} e^{\frac{-z^2 \sin^2(\theta_s+\theta_i)}{r_0^2 \cos\theta_s}}, \tag{2.80}$$

$$\frac{\partial \tilde{A}_i^0(\omega_i)}{\partial z} \approx \Upsilon^* \tilde{A}_s^0 (2\omega_0 - \omega_i) A_p^2 e^{\frac{-2z^2\left(\tan^2\theta_i + \tan^2\theta_p\right)}{r_0^2}} e^{\frac{-z^2 \sin^2(\theta_i+\theta_s)}{r_0^2 \cos\theta_i}}. \tag{2.81}$$

We need to work on the integral of Eq. 2.80 and Eq. 2.81 along z-axis inside the sample to solve for the generated signal and idler fields at the exit surface of the sample. Since the third-order nonlinearity is not strong enough to change the values of the operators, we can make the following assumptions (i) when solving for the signal operator at the exit surface $\tilde{A}_s\left(\frac{L}{2}, \omega_s\right)$, we assume the idler operator $\tilde{A}_i(z, \omega_i) = \tilde{A}_i(0, \omega_i)$, (ii) when solving for the idler operator at the exit surface $\tilde{A}_i\left(\frac{L}{2}, \omega_i\right)$, we assume the signal operator $\tilde{A}_s(z, \omega_s) = \tilde{A}_s(0, \omega_s)$. These assumptions require $\Upsilon A_p^2 L \ll 1$, which implies that the field operators are almost constant. After the integrations, the two operators at the exit surface of the sample become

$$\tilde{A}_s^0\left(\frac{L}{2}, \omega_s\right) = \tilde{A}_s^0\left(-\frac{L}{2}, \omega_s\right) + \Upsilon \tilde{A}_i^0\left(-\frac{L}{2}, 2\omega_0 - \omega_s\right) A_p^2 I_1(L), \tag{2.82}$$

$$\tilde{A}_i^0\left(\frac{L}{2}, \omega_i\right) = \tilde{A}_i^0\left(-\frac{L}{2}, \omega_i\right) + \Upsilon^* \tilde{A}_s^0\left(-\frac{L}{2}, 2\omega_0 - \omega_i\right) A_p^2 I_2(L), \tag{2.83}$$

where I_1 and I_2 are two spatial integrations along z-axis inside the sample that depend on the angles of the beams (θ_i, θ_s, and θ_p).

$$I_1 = \int_{-\frac{L}{2}}^{\frac{L}{2}} dz\, e^{\frac{-2z^2\left(\tan^2\theta_s + \tan^2\theta_p\right)}{r_0^2}} \times e^{\frac{-z^2\sin^2\left(\theta_s + \theta_i\right)}{r_0^2\cos^2\theta_s}}, \tag{2.84}$$

$$I_2 = \int_{-\frac{L}{2}}^{\frac{L}{2}} dz\, e^{\frac{-2z^2\left(\tan^2\theta_i + \tan^2\theta_p\right)}{r_0^2}} \times e^{\frac{-z^2\sin^2\left(\theta_i + \theta_s\right)}{r_0^2\cos^2\theta_i}}. \tag{2.85}$$

Note that in this case, I_1 and I_2 are not equal because the phase matching condition requires $\theta_s \neq \theta_i$.

We calculate the correlation function $G^{(2)}(\tau)$ for studying the temporal correlation between signal and idler fields [71]. τ is the temporal delay between the signal and idler detectors. Two bandpass filters with a bandwidth of $\Delta\omega$ are inserted in front of the detectors for confining the spectra of signal and idler fields.

$$G^{(2)} = \int_{-T}^{T} \frac{\langle 0|\hat{A}_s^\dagger(t+\tau)\hat{A}_i^\dagger(t)\hat{A}_i(t)\hat{A}_s(t+\tau)|0\rangle}{\langle 0|\hat{A}_s^\dagger(t)\hat{A}_s(t)|0\rangle\langle 0|\hat{A}_i^\dagger(t)\hat{A}_i(t)|0\rangle} \frac{dT}{2T} = 1 + \frac{sinc^2\left(\frac{\Delta\omega\tau}{2}\right)}{\left|\Upsilon I_1\right|^2 A_p^4}. \tag{2.86}$$

The photon-pair rate is given as

$$\langle 0|\hat{A}_s^\dagger(t)\hat{A}_s(t)|0\rangle = \left|\Upsilon I_1\right|^2 A_p^4 \Delta\omega. \tag{2.87}$$
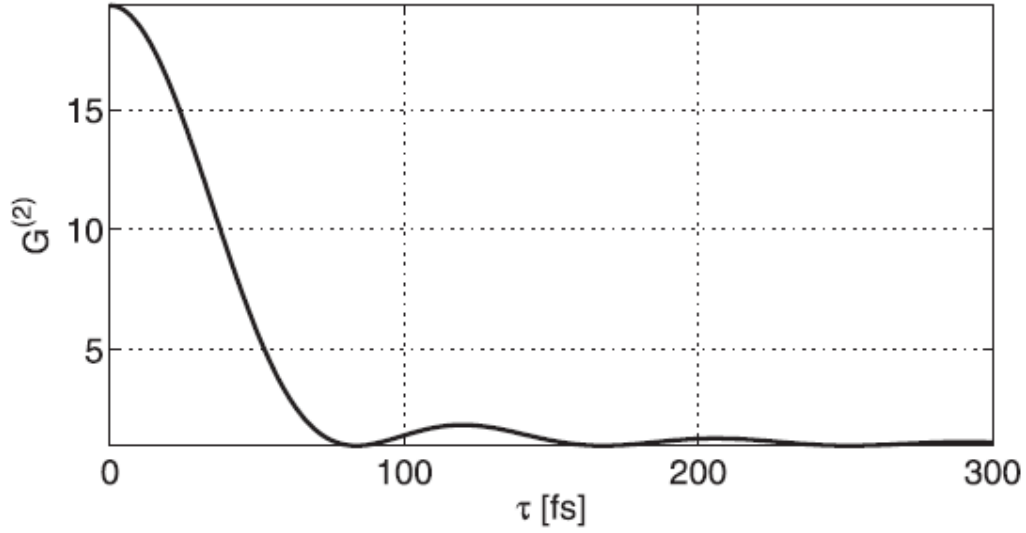
$G^{(2)}$ with respect to temporal delay τ between signal and idler beam. The bandpass filter width $\Delta\omega=20$ nm.

2.2.2.2.2   Gaussian-pulse approach

To simulate the real experimental setup, we treat the pump field as a pulse with a temporal Gaussian profile in this section. In this case, the field has a Gaussian shaped bandwidth in the frequency domain. Therefore, the pump field in the frequency domain can be written as [73]

$$E_p\left(x,y,z,t\right)=\int_{-\infty}^{\infty}d\omega_p A_p\left(\omega_p,x,y,z\right)e^{i\left(\frac{\omega_p z}{c}-\omega_p t\right)}, \tag{2.88}$$

where

$$A_p\left(\omega,x,y,z\right)=\sqrt{I_0}e^{-\frac{\left(\omega-\omega_0\right)^2}{2\sigma^2}}\times e^{-\frac{x^2+y^2}{2r_0^2}}, \tag{2.89}$$

which is a Gaussian shape centered at frequency ω_0 with a standard deviation of σ. This expression also contains a spatial Gaussian profile in the x-y plane with a standard deviation of r_0. The intensity $\tilde{I}$ is related to the energy within the pulse, therefore it's also related to the total photon numbers within pulse,

$$\grave{o}_0 \int_{-\infty}^{\infty} dx \int_{-\infty}^{\infty} dy \int_{-\infty}^{\infty} dz E_p^\dagger E_p = nh\omega_0. \tag{2.90}$$

The integration along space gives the total energy of the pump field within one pulse, which is equal to the energy of n photons within the pulse. The intensity is solved as

$$\tilde{I} = \frac{nh\omega_0}{2\pi^{2.5}\sigma r_0^2 c\grave{o}_0}. \tag{2.91}$$

We will also use the peak amplitude of the pump field ($\sqrt{I} = \sqrt{2\pi\tilde{I}\sigma^2}$) in the FWM process.

As we have treated the spatial Gaussian profile in the previous section, we use the same method in this section. So, in the following discussion, the spatial Gaussian profile of the two pump fields are ignored and inserted back as corrections terms later. We write the signal idler, and two pump fields in the frequency domain as

$$E_s = \int_{-\infty}^{\infty} d\omega_s A_s\left(\omega_s, z\right) e^{i\left(k_s z_s - \omega_s t\right)}, \tag{2.92}$$

$$E_i = \int_{-\infty}^{\infty} d\omega_i A_i\left(\omega_i, z\right) e^{i\left(k_i z_i - \omega_i t\right)}, \tag{2.93}$$

$$E_{p1} = \int_{-\infty}^{\infty} d\omega_{p1} A_{p1}(\omega_{p1}, z) e^{i(k_{p1}z_{p1} - \omega_{p1}t)}, \qquad (2.94)$$

$$E_{p2} = \int_{-\infty}^{\infty} d\omega_{p2} A_{p2}(\omega_{p2}, z) e^{i(k_{p2}z_{p2} - \omega_{p2}t)}. \qquad (2.95)$$

In the above equations, p_1 and p_2 represent the two pumps, A_{p1} and A_{p2} are the shape functions of the two pump fields, A_s and A_i are the shape functions of signal and idler fields, respectively. Although the pump fields are obtained from the same laser, they propagate along slightly different directions. Therefore, the difference between A_{p1}, A_{p2} should show the difference between the propagating directions of two pump beams. Since the pump beams are too strong to be affected by the generated signal and idler beams, we assume their amplitudes are constant in the process. Therefore, the two pump shape functions are given as

$$A_{p1}(\omega_{p1}, z) = A_{p1}(\omega_{p1}) = \sqrt{l} e^{-\frac{(\omega_{p1} - \omega_0)^2}{2\sigma^2}}, \qquad (2.96)$$

$$A_{p2}(\omega_{p2}, z) = A_{p2}(\omega_{p2}) = \sqrt{l} e^{-\frac{(\omega_{p2} - \omega_0)^2}{2\sigma^2}}, \qquad (2.97)$$

which are independent on z-axis. We use field operators instead of amplitudes to describe the signal and idler electric fields [72]. In the forward four-wave mixing geometry, the propagations of signal and idler field operators along z-axis satisfy the Maxwell's wave propagating equations

$$\frac{\partial \hat{A}_s(\omega_s, z)}{\partial z} = \frac{ik_s}{2\cos\theta_s} \chi^{(1)} \hat{A}_s(\omega_s) + \frac{3ik_s}{2\cos\theta_s} \chi^{(3)} \times$$

$$\int_{-\infty}^{\infty} d\omega_{p1} \int_{-\infty}^{\infty} d\omega_{p2} A_{p1}(\omega_{p1}) \cos\theta_p A_{p2}(\omega_{p2}) \cos\theta_p \hat{A}_i^\dagger(\omega_{p1}+\omega_{p2}-\omega_s,z) e^{i\Delta kz}, \tag{2.98}$$

$$\frac{\partial \hat{A}_i(\omega_i,z)}{\partial z} = \frac{ik_i}{2\cos\theta_i} \chi^{(1)} \hat{A}_i(\omega_i) + \frac{3ik_i}{2\cos\theta_i} \chi^{(3)} \times$$

$$\int_{-\infty}^{\infty} d\omega_{p1} \int_{-\infty}^{\infty} d\omega_{p2} A_{p1}(\omega_{p1}) \cos\theta_p A_{p2}(\omega_{p2}) \cos\theta_p \hat{A}_s^\dagger(\omega_{p1}+\omega_{p2}-\omega_i,z) e^{i\Delta kz}, \tag{2.99}$$

with

$$\Delta k = \frac{k_{p1}}{\cos\theta_p} + \frac{k_{p2}}{\cos\theta_p} - \frac{k_i}{\cos\theta_i} - \frac{k_s}{\cos\theta_s}. \tag{2.100}$$

The equations above indicate that the propagations of signal and idler field operators are driven by two processes, self-phase modulation and FWM process. The self-modulation process induces a phase change while the FWM induces an amplitude change. We separate the two processes by using the following transformations

$$\hat{A}_s(\omega_s,z) = \hat{A}_s^0(\omega_s,z) e^{\frac{ik_s\chi^{(1)}z}{2\cos\theta_s}}, \tag{2.101}$$

$$\hat{A}_i(\omega_i,z) = \hat{A}_i^0(\omega_i,z) e^{\frac{ik_i\chi^{(1)}z}{2\cos\theta_i}}, \tag{2.102}$$

$$\hat{A}_{p1}(\omega_{p1}) = \hat{A}_{p1}^0(\omega_{p1}), \tag{2.103}$$

$$\hat{A}_{p2}(\omega_{p2}) = \hat{A}_{p2}^0(\omega_{p2}). \tag{2.104}$$

By inserting Eq. 2.101 - Eq. 2.104 into Eq. 2.98, Eq. 2.99 and applying phase-matching conditions, we obtain

$$\frac{\partial \hat{A}_s^0(\omega_s, z)}{\partial z} = \Upsilon \int_{-\infty}^{\infty} d\omega_{p1} \int_{-\infty}^{\infty} d\omega_{p2} A_{p1}(\omega_{p1}) A_{p2}(\omega_{p2}) \hat{A}_i^{\dagger}(\omega_{p1} + \omega_{p2} - \omega_s, z),$$ (2.105)

$$\frac{\partial \hat{A}_i^0(\omega_i, z)}{\partial z} = \Upsilon \int_{-\infty}^{\infty} d\omega_{p1} \int_{-\infty}^{\infty} d\omega_{p2} \hat{A}_{p1}^0(\omega_{p1}) \hat{A}_{p2}^0(\omega_{p2}) \hat{A}_s^0(\omega_{p1} + \omega_{p2} - \omega_i, z),$$ (2.106)

where $\Upsilon = \frac{3i\omega_0}{2c}\chi^{(3)}$ is a constant. The above equations contain only the effect of the third-order nonlinearity because the self-phase modulation terms are contained inside the signal and idler operators. We can apply the spatial Gaussian profile of the fields as correction terms into equations Eq. 2.105 and Eq. 2.106. By doing the integral, we obtain the signal and idler operators at the exit surface of the sample as

$$\hat{A}_s^0\left(\omega_s, \frac{L}{2}\right) = \hat{A}_s^0\left(\omega_s, -\frac{L}{2}\right) + \Upsilon \times$$

$$\int_{-\infty}^{\infty} d\omega_{p1} \int_{-\infty}^{\infty} d\omega_{p2} \tilde{A}_{p1}(\omega_{p1}) \tilde{A}_{p2}(\omega_{p2}) \hat{A}_i^{\dagger}\left(\omega_{p1} + \omega_{p2} - \omega_s, -\frac{L}{2}\right) I_1(L),$$ (2.107)

$$\hat{A}_i^0\left(\omega_i, \frac{L}{2}\right) = \hat{A}_i^0\left(\omega_i, -\frac{L}{2}\right) + \Upsilon^* \times$$

$$\int_{-\infty}^{\infty} d\omega_{p1} \int_{-\infty}^{\infty} d\omega_{p2} \hat{A}_{p1}^0(\omega_{p1}) \hat{A}_{p2}^0(\omega_{p2}) \hat{A}_s^0\left(\omega_{p1} + \omega_{p2} - \omega_i, -\frac{L}{2}\right) I_2(L).$$ (2.108)

with two spatial integrations

$$I_1 = \int_{-\frac{L}{2}}^{\frac{L}{2}} dz e^{\frac{-2z^2\left(\tan^2\theta_s + \tan^2\theta_p\right)}{r_0^2}} \times e^{\frac{-z^2\sin^2(\theta_s + \theta_i)}{r_0^2\cos^2\theta_s}},$$ (2.109)

$$I_2 = \int_{-\frac{L}{2}}^{\frac{L}{2}} dz e^{\frac{-2z^2\left(\tan^2\theta_i + \tan^2\theta_p\right)}{r_0^2}} \times e^{\frac{-z^2\sin^2(\theta_i + \theta_s)}{r_0^2\cos^2\theta_i}}.$$ (2.1130)

Note that the two integrations are the same as in the previous section.

We use the temporal correlation function $(G^{(2)}(\tau))$ to characterize the correlation between signal and idler beams with a temporal difference of τ [71].

$$G^{(2)} = \int_{-T}^{T} \frac{\langle 0|\hat{A}_s^{\dagger}(t+\tau)\hat{A}_i^{\dagger}(t)\hat{A}_i(t)\hat{A}_s(t+\tau)|0\rangle}{\langle 0|\hat{A}_s^{\dagger}(t)\hat{A}_s(t)|0\rangle\langle 0|\hat{A}_i^{\dagger}(t)\hat{A}_i(t)|0\rangle} \frac{dT}{2T} \tag{2.111}$$

In the <u>Eq. 2.111</u>, $\hat{A}_i(t)$ destroys (detects) an idler photon at time t, while $\hat{A}_s(t+\tau)$ on the other hand, destroys (detects) a signal photon at time $t + \tau$. These operators act on the vacuum state $|0\rangle$ because no signal/idler photons are introduced in the SpFWM process. Since the bandpass filters are inserted to confine the bandwidth of the generated photons on each arm, $G^{(2)}$ can be calculated as

$$G^{(2)} = 1 + \frac{sinc^2\left(\dfrac{\Delta\omega\tau}{2}\right)}{4\left|\Upsilon \mathit{l}_0\right|^2 \pi^2\sigma^4} \frac{1}{2T}\int_{-T}^{T} e^{4\sigma^2 t^2} e^{-2(A-t)^2\sigma^2} dt. \tag{2.112}$$

Where $\Delta\omega$ is the bandwidth. The number of the photon-pair per pulse is

$$\int_{-\infty}^{\infty}\langle 0|\hat{A}_s^{\dagger}(t)\hat{A}_s(t)|0\rangle dt = \int_{-\infty}^{\infty} 4\left|\Upsilon \mathit{l}_0\right|^2 \Delta\omega\pi^2\sigma^4 e^{-2\sigma^2 t^2} dt = \frac{4\sqrt{\pi}}{\sqrt{2}}\left|\Upsilon \mathit{l}_0\right|^2 \Delta\omega\pi^2\sigma^3. \tag{2.113}$$

The temporal correlation function $G^{(2)}(\tau)$ behaves differently in the two cases with (i) continuous-wave field and (ii) Gaussian-pulse field. The difference is caused by the temporal integration. We calculate the photon-pair per pulse as 0.4353 per pulse.
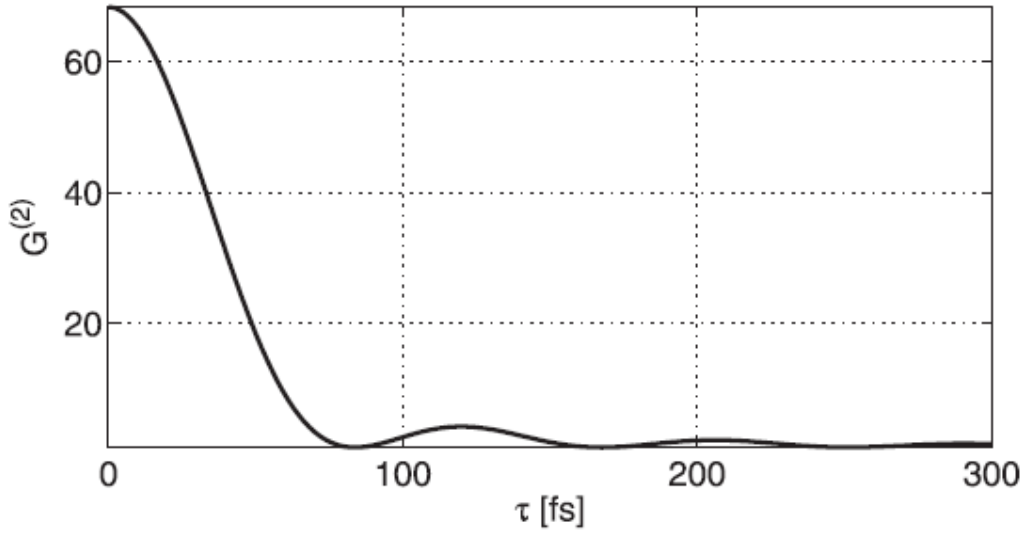
$G^{(2)}$ with respect to temporal delay τ between signal and idler beam. For pulsed case, we detect photons in a limited time interval of 200 fs (FWHM of one pulse), rather than continuously detect photons as in CW case. The bandpass filter width $\Delta\omega=20$ nm.

2.2.2.2.3 Single counts in spontaneous four-wave mixing

In the frequency domain representation, if the pump is Gaussian with a peak intensity of E_{p0} and variance $\sigma = 2\sqrt{ln4}/\Delta\omega_p$, where $\Delta\omega_p$ is the bandwidth of the pump, then the single count of the signal is given as [74]

$$N_s = \left(\frac{SIL}{2}\right)^2 \left(\frac{\sqrt{\pi}}{\sigma}\right)^2 \iint sinc^2 \left(\frac{\Delta kL}{2}\right)^2 exp\left(-\frac{|\Delta\omega_s+\Delta\omega_i|^2\sigma^2}{2}\right) \frac{d\Delta\omega_s}{v_{gs}} \frac{d\Delta\omega_i}{v_{gi}}, \qquad (2.114)$$

where $S = \epsilon_0\chi^{(3)}\frac{E_{p0}^2}{4}\sqrt{\frac{\omega_s\omega_i}{4\epsilon_s\epsilon_i}}$ is the gain parameter, I is a normalized factor, $\Delta\omega_s$ and $\Delta\omega_i$ represent the frequency detuning in the signal and idler channels, v_{gs} and v_{gi} are the group velocities, respectively. Note that the $\chi^{(3)}$ in the nondegenerate SpFWM is different from the $\chi^{(3)}$ in the degenerate StFWM. However, their values

are close since the nonlinearity is based on a two-photon resonance in a two-level system without other resonances which may occur from an intermediate level. Therefore, we assume the value of $\chi^{(3)}$ in SpFWM is also on the order of 10^{-23} m^{2}V^{-2}, corresponding to that in the degenerate case. In our experiment, $sinc^2 \left(\frac{\Delta kL}{2} \right)^2 \ll 1$, the signal is centered at 730 nm with a bandwidth of 20 nm, and the idler is centered at 849 nm with a bandwidth of 20 nm. If we assume $\epsilon_s = \epsilon_i = \epsilon_0$, for estimation purposes, then $N_s = 0.05$ per pulse when the pump power is 5 mW. It corresponds to a rate of 2000 pairs per second, which is much greater than 0.2 pairs per second according to the experimental result under similar conditions cite [75]. The difference mainly depends on two reasons. First, we targeted a small portion (~0.1%) of photon pairs on the phase-matching cone. Second, the low detection efficiencies (~50% on each arm) result in even less (~25%) photon-pair rates.

In conclusion, we have investigated a theoretical model that can explain the instantaneous $\chi^{(3)}$ nonlinearity of a two-level system with permanent dipole moments in response to ultrashort pulses. The results match the numerical simulation if the amplitude of the electric field is within the limit. Moreover, the model could estimate the strength of the nonlinearity as observed in the experimental discoveries.

2.2.3   Two Photon Absorption
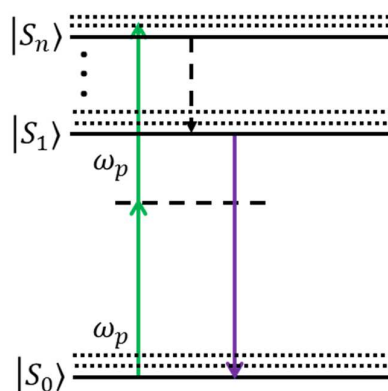
The two-photon absorption in the energy-level diagram of EGFP. The solid lines represent energy levels, the dotted lines represent vibronic levels, and the dashed lines represent the virtual states. The green arrows represent the pump photons with a frequency of ω_p, and the purple arrow represents the fluorescence.

Along with the FWM process are some other nonlinear effects that can induce noise to the generated photon pairs. The major nonlinear noisy processes are two photon absorption (TPA) and Raman scattering. In this section, we study TPA. TPA is the process of simultaneously absorbing two photons of same or different frequencies to excite a molecule from one electronic state (usually the ground state) to a higher electronic state. Accompanying the TPA is the fluorescence. According to Vavilov-Kasha's rule, the fluorescence of polyatomic molecules always occurs from the lowest excited state (S_1) to the ground state (S_0). This is because the higher excited electronic state ($S_{n>1}$) decays non-radiatively to the S_1 on a picosecond time scale, S_1 then decays radiatively to S_0 on a nanosecond time scale with an emitted photon (fluorescence) as shown in Fig. 2.11. The probability of TPA is characterized by the

two-photon absorption cross section (σ_2), which is measured in Goeppert-Mayer units with 1 GM = 10^{-50} cm^{4}s. TPA can occur in a three-level system, or in a two-level system with permanent dipole moments. For the three-level model [52],

$$\sigma_2(v) = \frac{Av^2|\mu_{n1}|^2|\mu_{10}|^2 g_2(v)}{(v_{10} - v)^2},$$ (2.115)

Where A is a constant, v is the excitation frequency, μ_{n1} and μ_{10} are the dipole moments between S$_n$ and S$_1$, and S$_1$ and S$_0$, respectively, $g_2(v)$ is the TPA line-shape function, v_{10} is the frequency difference between S$_1$ and S$_0$. TPA can be very strong in the region if μ_{n1} and μ_{10} are large, and if resonance enhancement occurs when the excitation frequency is close to v_{10}. For the two-level system [52],

$$\sigma_2(v) = A|\Delta\mu_{10}|^2|\mu_{10}|^2 g_2'(v),$$ (2.116)

Where $\Delta\mu_{10}$ is the difference permanent dipole moments of S$_1$ and S$_0$, and $g_2'(v)$ is the TPA line-shape function. In our experiment, the center excitation wavelength is 785 nm, thus we should use the two-level model for describing TPA. We see that the term "$|\Delta\mu_{10}|^2|\mu_{10}|^2$" also occurs in our third-order nonlinearity in the "two-level system" section, that's because the imaginary part of the third-order nonlinearity is responsible for the TPA. TPA is a major noisy process in our photon-pair generation experiment because of two reasons. First, the fluorescence photons may leak into the photodetectors that dilute the generated photon pairs. Second, the fluorophores that participate in the TPA cannot undergo the SpFWM process.

Although TPA can reduce the purity of photon pairs generated in our experiment, it has significant applications in imaging living systems. For example, researchers use two-photon laser scanning microscopy (2PLSM) [76, 77] of cells and tissues expressing fluorescent proteins for biological studies. 2PLSM can help obtain better optical recordings of ion concentration and cell signaling with genetically targeted sensors [24, 59]. The potential advantages of TPA can also be achieved in the genetically targeted deep photodynamic therapy, chromophore-assisted light inactivation [59], three-dimensional optical memory [45], and super-resolution imaging techniques (such as stimulated emission depletion [78], photoactivated localization microscopy and stochastic optical reconstruction microscopy [79]).

What's more, people use TPA in microfabrication and lithography because the absorption rate of light by a molecule depends on the square of the power of the laser. Therefore, if the material is cut with a high-power laser beam, the rate of material removal decreases very sharply from the center of the beam to its periphery. Thus, the "pit" created with TPA is sharper and better resolved than using normal absorption.

2.2.4   Raman Scattering

$$\omega_v = \omega_p - \omega_S \qquad \omega_v' = \omega_a - \omega_p$$
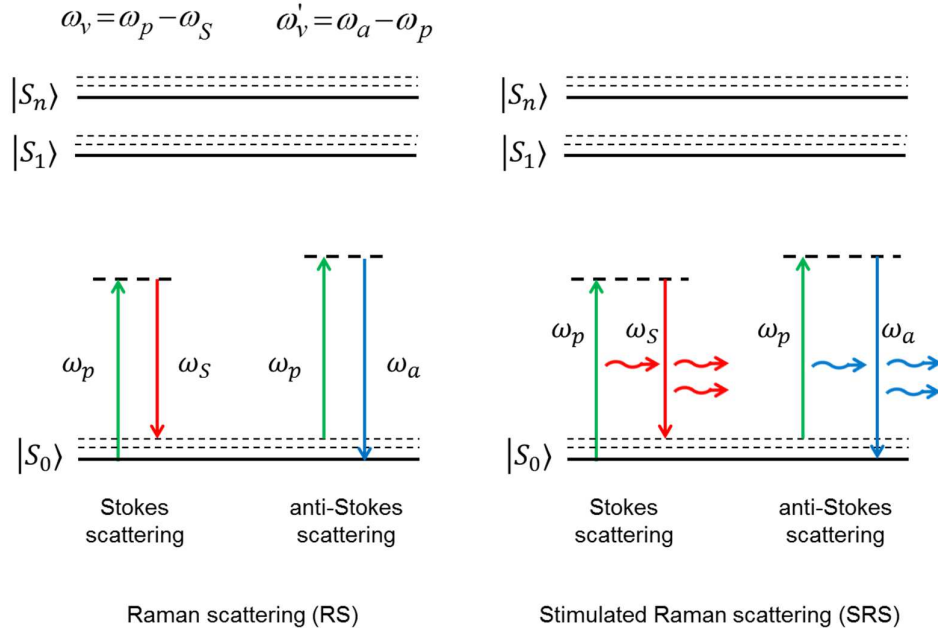
Raman scattering and stimulated Raman scattering on the electronic states of EGFP. The green arrow represents the pump photon (ω_p), the red arrow represents the Stokes photon (ω_S), and the blue arrow represents the anti-Stokes photon (ω_a). The curved arrow represents the stimulated process.

In this section, we study the Raman scattering (RS) and Stimulated Raman Scattering (SRS) because they can induce noise in the photon pairs generated in the experiment. In our system, RS may occur due to one pump photon scatters inelastically by annihilating (anti-Stokes process) or creating (Stokes process) a vibrational phonon as shown in the left part of Fig. 2.12. Stokes scattering can incur noise in the idler channel where the wavelength is longer than the pump photons. In a similar way, anti-Stokes scattering can incur noise in the signal channel where the wavelength is shorter than the pump photons. Although most pump photons scatter elastically (Rayleigh scattering) such that they retain their energy (frequency and wavelength),

there's still a small fraction of the pump photons that scatters inelastically. This can be a concern if the number of incident pump photons is huge as is the case in our experiment where we use high-energy pump pulses. Of the two processes, stokes scattering is much more common than anti-Stokes scattering because of Boltzmann distribution of the vibronic states, where the lower energy states are more often occupied than the higher ones. Therefore, RS incurs more noise in the idler channel than in the signal channel. To reduce the noise incurred by RS in the signal/idler channel, we can use polarization filtering. This is because the photon pairs generated from SpFWM are co-polarized with the pump photons, while Raman photons are not co-polarized with pump photons. The polarization filtering can reduce about half of the Raman photons in the signal/idler channel.

If the previously generated Stokes/anti-Stokes photons participate in the RS, then the stimulated Raman scattering (SRS) can occur in the system as shown in the right part of Fig 2.12. The Stokes field (anti-Stokes field) at frequency $\omega_s = \omega_p - \omega_v$ ($\omega_a = \omega_p + \omega_v$) can beat with the pump field to produce a modulation of the total electric-field intensity. The modulated field contains a frequency component of ω_v, which leads to a stronger molecular vibration. The stronger molecular vibration then leads to a stronger Stokes field, which in turn leads to a stronger molecular vibration. In this case, more pump photons are converted into Raman photons than in the Raman scattering. Therefore, SRS amplifies the Stokes (anti-Stokes) scattering in the presence of the pump field, adding more noise photons in the idler (signal) channel.

Note that SRS is more effective in the idler channel than in the signal channel due to more Stokes photons are created than the anti-Stokes photons in the RS process. Unfortunately, the polarization filtering cannot effectively distinguish SRS photons from the FWM photons because both processes create photons with the same polarization as the pump photons.

Note that the Raman effect intrinsically differs from the process of fluorescence. In fluorescence, the incident light is completely absorbed, and the system is transferred to an excited state from which it can go to various lower states only after a certain resonance lifetime. However, the Raman effect can take place for any frequency of incident light. In contrast to the fluorescence effect, the Raman effect is not a resonant effect. Therefore, the fluorescence peak is always anchored at a specific frequency depending on the energy difference between the first excited state and the ground state, while the Raman peak maintains a constant separation from the excitation frequency. Although RS and SRS can reduce the purity of the photon pairs generated from SpFWM process in our experiment, Raman spectroscopy can be very useful in some applications such as material identification and analysis. SRS is exploited in Raman amplifiers and Raman lasers.

2.3   Z-scan technique

A careful measurement of the third-order nonlinearity, both its real and imaginary parts, is required to predict the performance of the photon-pair source in our

experiment. The z-scan technique has been widely used for measuring such nonlinearities of nonlinear media [80].

(a)

Open-aperture scheme

$$\zeta = \frac{z}{2z_0}$$

(b)

Closed-aperture scheme

$$\zeta = \frac{z}{2z_0}$$
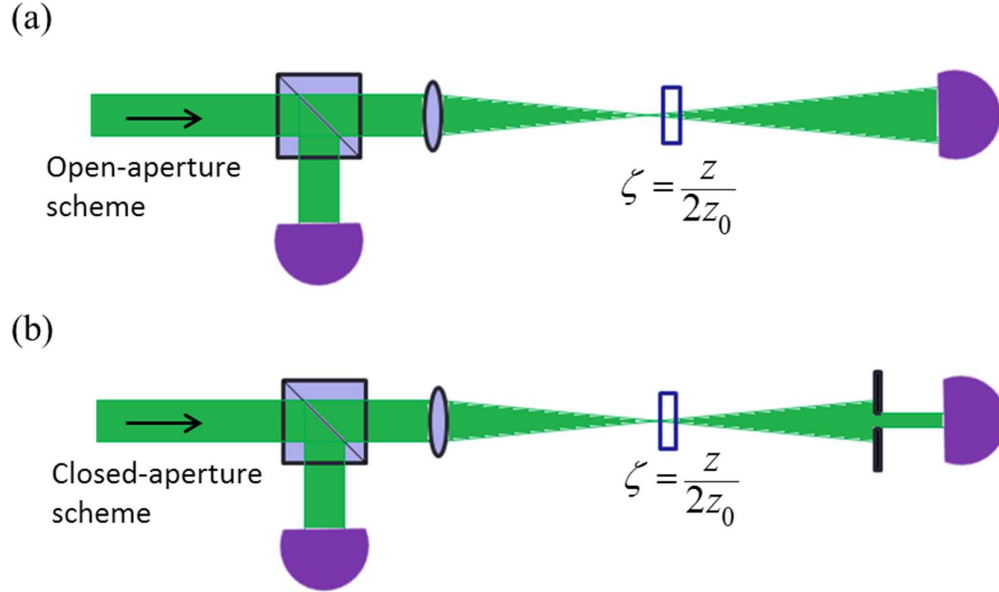
Figure 2. 13

Z-scan schemes. (a) open-aperture z-scan. (b) closed-aperture z-scan. The laser is split by a beam splitter and then focused into a cuvette that is free to move on the z-axis. The transmitted light is sent into a detector with/without an aperture.

In practice, the z-scan technique relies on moving the nonlinear sample along a well-defined Gaussian beam on the z-axis for recording the transmitted power in two schemes as shown in Fig. 2.13; one with an open aperture in front of the end detector, the other with a closed aperture in front of the end detector. In the open-aperture scheme, we assume all the transmitted power are captured by the detector. Therefore, the change of the transmitted power with respect to the sample position is directly related to the nonlinear absorption of the Gaussian beam at different positions. In the closed-aperture scheme, only the center part of the power is measured. In other word,

the measured intensity is related to the beam radius. Therefore, in the closed aperture scheme, measuring the power is equivalent as measuring the beam radius as a function of the sample position. Due to the self-focusing effect induced by the $\chi^{(3)}$ nonlinearity, the sample can be viewed as a lens. For example, if the nonlinear refractive index is positive, the sample is equivalent as a convex lens; self-focusing can increase the beam divergence if the sample is placed in front of the focus and thus reduce the measured intensity, self-focusing can reduce beam divergence if the sample is placed behind the focus and thus increase the measured intensity. If the nonlinear refractive index is negative, the sample can be treated as a concave lens. Therefore, it is possible to calculate the value of the nonlinear refractive index by measuring the dependence of the intensity on the sample position. Note that the open-aperture scheme is also used in conjunction with the closed-aperture scheme to correct the calculated value of $\chi^{(3)}$ because the nonlinear absorption can affect the measurement of the nonlinear refractive index. In summary, the z-scan technique can provide clues for speculating the nonlinear absorption and the nonlinear refraction of light inside the medium to obtain the value of $\chi^{(3)}$. In this section, we study the intricate z-scan theory and discuss the measurement of the third-order nonlinearity of EGFP.

2.3.1   Gaussian-beam approach of z-scan technique

To obtain an expression of the electric field, we can start from the Maxwell equation

$$\frac{1}{c^2}\frac{\partial^2 E}{\partial t^2} - \nabla^2 E = 0 \qquad (2.117)$$

where E is the electric field, c is the speed of light. In the z-scan technique, the paraxial approximation is applied such that the complex field is approximated as

$$E(x,y,z) \approx A(x,y,z)e^{ikz-i\omega t}. \qquad (2.118)$$

where $k = \frac{2\pi}{\lambda}$ is the wave vector and λ is the wavelength. We can apply the slowly varying envelope approximation (SVEA) to solve Eq. 2.117. The SVEA is valid when the envelope of the electric field $A(x,y,z)$, varies slowly in time and space compared to one period or wavelength, which is the case in our experimental setup. By applying the SVEA, we can simplify the Helmholtz equation Eq. 2.117 into

$$\nabla_\perp^2 A + 2ik\frac{\partial A}{\partial z} = 0. \qquad (2.119)$$

The above differential equation has an infinite set of solutions. Among the solution set, the Gaussian expression is the lowest-order one. In fact, Gaussian expression turns out to be a good approximation for most laser beams [81]. Therefore, we consider our laser as a well-defined Gaussian beam and thoroughly study its behaviors under the third-order nonlinearity in this section. The first order solution (Gaussian expression) of the electric field is written as

$$E(z,r,t) = E_0(t)\frac{w_0}{w(z)}\exp\left(-\frac{r^2}{w^2(z)} - \frac{ikr^2}{2R(z)}\right)e^{-i\phi(z,t)}, \qquad (2.120)$$

where w_0 is the beam waist; $w(z) = w_0\sqrt{1 + \frac{z^2}{z_0^2}}$, is the beam radius at z, $R(z) =$ $z\left(1 + \frac{z_0^2}{z^2}\right)$ is the radius of curvature of the wavefront at z, $z_0 = \frac{kw_0^2}{2}$ is the diffraction length of the beam. $E_0(t)$ is the radiation electric field at the focal point where $z = 0$ that contains temporal information of the Gaussian beam. $e^{-i\phi(z,t)}$ is a phase factor that contains all the radially uniform phase variations.

In the z-scan technique, the beam radius will change due to diffraction or nonlinear refraction inside the sample. However, if the sample is thin enough, then the change of the beam radius is negligible. The "thin sample" assumption is valid when the length of the sample $L \ll z_0$. The assumption is also valid when $L \ll \frac{z_0}{\Delta\phi(0)}$, where $\Delta\phi(0)$ is the radial phase variation. Since our experimental setup qualifies the criteria, we apply the "Thin sample" assumption in the following discussions.

The third-order nonlinearity contains real and imaginary parts. The real part modulates the phase ϕ of the electric field, while the imaginary part induces nonlinear absorption. Therefore, the intensity I and the phase ϕ of the electric field are expressed as a function of z' as shown below:

$$\frac{d\Delta\phi}{dz'} = \Delta n(I)k, \tag{2.121}$$

$$\frac{dI}{dz'} = -\alpha(I)I, \tag{2.122}$$

where z' is the propagation length inside the sample, $\alpha(I)$ is an absorption term which includes both linear and nonlinear absorption terms. The linear absorption term

α is a constant. The third-order nonlinear absorption term βI is intensity dependent, with β being a constant. If the third-order nonlinear absorption term βI is negligible, then $\alpha(I) \approx \alpha$. In this case, Eq. 2.121 and Eq. 2.122 are solved as

$$I(z') = I(0)e^{-\alpha z'}, \tag{2.123}$$

$$\Delta\phi(z') = kn_2 I(0)\int_0^{z'} e^{-\alpha z'} dz' = kn_2 I(0)\frac{1}{\alpha}\left(1-e^{-\alpha z'}\right), \tag{2.124}$$

where $I(0)$ is the electric field intensity at the entrance surface of the sample. We can solve the intensity and phase of the electric field at the exit surface of the sample as a function of space and time by using the Gaussian expression as shown below,

$$I(z,r,t) = \frac{I_0(t)}{1+\frac{z^2}{z_0^2}} e^{-\frac{2r^2}{w^2(z)}} e^{-\alpha L}, \tag{2.125}$$

$$\Delta\phi(z,r,t) = \frac{kn_2 I_0(t) L_{eff}}{1+\frac{z^2}{z_0^2}} e^{-\frac{2r^2}{w^2(z)}}, \tag{2.126}$$

where

$$L_{eff} = \frac{L}{\alpha}\left(1-e^{-\alpha z'}\right). \tag{2.127}$$

$I_0(t)$ is the on-axis irradiance at the focal point ($z = 0$). The electric field at the exit surface of the sample E_e contains both linear absorption term and phase distortion term

$$E_e(z,r,t) = E(z,r,t)e^{-\frac{\alpha L}{2}} e^{i\Delta\phi(z,r,t)}. \tag{2.128}$$

[Eq. 2.128](#) is no longer a Gaussian beam due to the phase distortion term $e^{i\Delta\phi(z,r,t)}$. This non-Gaussian expression gives trouble on solving the propagation of the electric field at the detector end. We can use Taylor expansion to simplify this problem by decomposing the electric field into an infinite series of Gaussian beams with increasing orders. The Taylor expansion of the phase distortion is expressed as

$$e^{i\Delta\phi(z,r,t)} = \sum_{m=0}^{\infty} \frac{\left[i\Delta\phi_0\left(z,t\right)\right]^m}{m!} e^{-\frac{2mr^2}{w^2(z)}}. \qquad (2.129)$$

where

$$\Delta\phi_0\left(z,t\right) = \frac{k\gamma I_0\left(t\right)L_{eff}}{1+\dfrac{z^2}{z_0^2}}, \qquad (2.130)$$

$$\Delta\phi\left(z,r,t\right) = \Delta\phi_0\left(z,t\right)e^{-\frac{2r^2}{w^2(z)}}. \qquad (2.131)$$

As a result, the phase distortion induced by the third-order nonlinearity has transformed the fundamental TEM$_{00}$ mode Gaussian beam into a series of Gaussian beams with a beam width of $w_m(z) = \frac{w(z)}{\sqrt{2m+1}}$. Each Gaussian beam travels independently and reconstructs at the detector end. We discuss two cases (a) the beam waist w_0 is relatively large and (b) the beam waist w_0 is not relatively large.

When the beam waist w_0 is relatively large, the mth Gaussian beam at distance z becomes:

$$E_m(z,r,t) = E_0(t) e^{-\frac{\alpha L}{2}} \frac{\left[i\Delta\phi_0(z,t)\right]^m}{m!} \frac{w_m(0)}{w_m(z)} exp\left(-\frac{r^2}{w_m^2(z)} - \frac{ikr^2}{2R_m(z)} - i\Theta_m(z)\right) e^{-i\phi(z,t)},$$

(2.132)

where the diffraction length of the beam $z_m = \frac{kw_m^2(0)}{2}$, the curvature of the wave front

$R_m(z) = z\left(1 + \frac{z_m^2}{z^2}\right)$, and $\Theta_m(z) = -\tan^{-1}\frac{z}{z_m}$.

In the case where w_0 is not relatively large, the electric field at the aperture becomes

$$E_a(r,t) = E(z, r=0, t) e^{-\frac{\alpha L}{2}} \sum_{m=0}^{\infty} \frac{\left[i\Delta\phi_0(z,t)\right]^m}{m!} \frac{w_m(0)}{w_m(z)} exp\left(-\frac{r^2}{w_m^2(z)} - \frac{ikr^2}{2R_m(z)} - i\theta_m\right). (2.133)$$

where d is the distance between the sample and the detector. With the definition of

$g = 1 + \dfrac{d}{R(z)}$, the remaining parameters in the Eq. 2.133 are:

$$w_{m0} = \frac{w(z)}{\sqrt{2m+1}},$$

(2.134)

$$d_m = \frac{kw_m^2(0)}{2},$$

(2.135)

$$w_m^2 = w_{m0}^2\left(g^2 + \frac{d^2}{d_m^2}\right),$$

(2.136)

$$R_m = d\left(1 - \frac{g}{g^2 + d^2/d_m^2}\right)^{-1},$$

(2.137)

$$\theta_m = \tan^{-1}\frac{d/d_m}{g}.$$

(2.138)

Once the electric field at the detector is obtained, we can immediately calculate the

power that transmitted to the detector by working out an integral with respect to the

aperture area to estimate the nonlinear refractive index and the nonlinear absorption coefficient.

2.3.2 The Normalized z-scan transmittance

In practice, we measure the normalized z-scan transmittance to speculate the third-order nonlinearity. The normalized z-scan transmittance is defined as the ratio between the transmitted power with and without the sample. However, the two transmitted powers cannot be simultaneously obtained. We split the laser beam into two parts to solve this problem. One part goes into a detector after passing through the sample while the other part goes into another detector without passing through the sample. The transmittance $T(z)$ is given as:

$$T(z) = \frac{\int_{-\infty}^{\infty} P_T\left(\Delta\Phi_0(t)\right)dt}{S\int_{-\infty}^{\infty} P_i(t)dt}, \qquad (2.139)$$

where

$$P_T\left(\Delta\Phi_0(t)\right) = c\epsilon_0 n_0 \pi \int_0^{r_a} \left|E_a(r,t)\right|^2 rdr, \qquad (2.140)$$

$$P_i(t) = \frac{\pi w_0^2 I_0(t)}{2}, \qquad (2.141)$$

$$S = 1 - e^{-\frac{2r_a^2}{w_a^2}}. \qquad (2.142)$$

$P_T\left(\Delta\Phi_0(t)\right)$ is the transmitted power through an aperture with radius r_a, $P_i(t)$ is the instantaneous input power, and S is the aperture linear transmittance.

The value of β can be obtained by open aperture z-scan measurement. In open aperture z-scan measurement ($S = 1$), the normalized transmittance is rewritten as

$$T\left(z, S = 1\right) = \frac{1}{\sqrt{\pi} q_0\left(z, 0\right)} \int_{-\infty}^{\infty} ln\left[1 + q_0\left(z, 0\right) e^{-\tau^2}\right] d\tau \qquad (2.143)$$

where

$$q_0\left(z, 0\right) = \frac{\beta I_0\left(t\right) L_{eff}}{1 + \dfrac{z^2}{z_0^2}}. \qquad (2.144)$$

As a result, we can speculate the nonlinear absorption coefficient β by numerically fitting the measured open aperture z-scan transmittance data with the theoretical value in Eq. 2.143. When $|q_0(z, 0)| < 1$, Eq. 2.143 is further simplified by using Taylor expansion with respect to $q_0(z, 0)$, which has the advantage in numerical evaluation.

$$T\left(z, S = 1\right) = \sum_{m=0}^{\infty} \frac{\left[-q_0\left(z, 0\right)\right]^m}{\left(m + 1\right)^{1.5}}. \qquad (2.145)$$

In conclusion, the value of nonlinear absorption coefficient β can be clearly determined by fitting the open aperture z-scan transmittance to Eq. 2.143 or Eq. 2.145.

On the other hand, we obtain n_2 with a closed aperture z-scan measurement. We divide the closed aperture z-scan transmittance by the open aperture z-scan transmittance [82]. The divided result appears to be a z-scan transmittance without nonlinear absorption process. In fact, the result agrees to the z-scan transmittance

from a purely refractive z-scan within 10% error. Finally, we fit the divided result to

obtain n_2 by using the well-established formula

$$T(x) = 1 + \frac{4x\Delta\Phi}{\left(1+x^2\right)\left(9+x^2\right)} + \frac{4\left(3x^2-5\right)\Delta\Phi^2}{\left(1+x^2\right)^2\left(9+x^2\right)\left(25+x^2\right)} + \frac{32\left(3x^2-11\right)x\Delta\Phi^3}{\left(1+x^2\right)^3\left(9+x^2\right)\left(25+x^2\right)\left(49+x^2\right)}.$$

(2.146)

In Eq. 2.146, $T(x)$ is the normalized transmittance, $x = \frac{z}{z_0}$ is the normalized position

of the sample, $\Delta\Phi = kn_2 I_0(t)L_{eff}$ is the on-axis nonlinear phase shift at the focal

point.

In conclusion, we have thoroughly outlined the theory of the z-scan technique. Based

on that study, we reviewed the method for speculating the third-order nonlinearity of a

thin sample. In our experiment as discussed in Chapter 3, we apply the z-scan

technique to obtain the nonlinear refractive index of EGFP.

2.4 Quantum State Tomography

We generate the polarization-entangled two-photon state $\left(|HH\rangle + e^{i\phi}|VV\rangle\right)/\sqrt{2}$

through a four-wave mixing process in EGFP. We then use the standard method of

quantum state tomography (QST) to characterize the state. QST is the process of

reconstructing the density matrix for a source of quantum systems by measurements

on the systems coming from the source. The measurements must be tomographically

complete to uniquely identify the state. In other words, the measured operators must

form an operator basis on the Hilbert space of the system, providing all the information about the state.

In our case, to characterize the photonic state, we need 15 unknown parameters that determine a 4×4 density matrix, and 1 unknown real parameter, which is a constant that related to the detector efficiency and light intensity. Therefore, we need a total of 16 measurements to perform the QST. One possible tomographic analysis states used in our experiments is shown in the table below. For each setting of waveplates, we measure the coincidence counts (CC) and accidentals (AC). Using the maximum likelihood estimation, we can reconstruct the 4×4 density matrix ρ^{HV} in the horizontal-vertical (HV) basis.

number	Mode$_s$	Mode$_i$	HWP$_s$	QWP$_s$	HWP$_i$	QWP$_i$
1	$|H\rangle$	$|H\rangle$	0°	0°	0°	0°
2	$|H\rangle$	$|V\rangle$	0°	0°	45°	0°
3	$|V\rangle$	$|V\rangle$	45°	0°	45°	0°
4	$|V\rangle$	$|H\rangle$	45°	0°	0°	0°
5	$|R\rangle$	$|H\rangle$	22.5°	90°	0°	0°
6	$|R\rangle$	$|V\rangle$	22.5°	90°	45°	0°
7	$|D\rangle$	$|V\rangle$	22.5°	45°	45°	0°

8	$|D\rangle$	$|H\rangle$	22.5°	45°	0°	0°
9	$|D\rangle$	$|R\rangle$	22.5°	45°	22.5°	90°
10	$|D\rangle$	$|D\rangle$	22.5°	45°	22.5°	45°
11	$|R\rangle$	$|D\rangle$	22.5°	90°	22.5°	45°
12	$|H\rangle$	$|D\rangle$	0°	0°	22.5°	45°
13	$|V\rangle$	$|D\rangle$	45°	0°	22.5°	45°
14	$|V\rangle$	$|L\rangle$	45°	0°	22.5°	0°
15	$|H\rangle$	$|L\rangle$	0°	0°	22.5°	0°
16	$|V\rangle$	$|L\rangle$	45°	0°	22.5°	0°

Table 2.2 The tomographic analysis states used in the experiments. QWP$_\mathrm{s}$ (HWP$_\mathrm{s}$): quarter (half) waveplate on signal arm, QWP$_\mathrm{i}$ (HWP$_\mathrm{i}$): quarter (half) waveplate on idler arm. $|D\rangle = (|H\rangle + |V\rangle)/\sqrt{2}$, $|R\rangle = (|H\rangle + i|V\rangle)/\sqrt{2}$ and $|L\rangle = (|H\rangle - i|V\rangle)/\sqrt{2}$.

2.5 Correlations

In the previous sections, we have studied the generation of photon pairs via SpFWM from the EGFP, the noise processes, and the z-scan technique for characterizing the $\chi^{(3)}$ nonlinearity. Here in this section, we move forward to characterize the properties of the photon pairs because of two reasons. First, the photon pairs can reflect the quantum mechanical properties within the system. Second, the photon pairs may have different applications depending on their properties. For example, if the

photon pairs can exhibit quantum correlations, then it not only indicates the preservation of quantum superposition and coherence within the EGFP, but also potentially develops novel quantum spectroscopic techniques in biological studies. For this purpose, our priority is to distinguish the classical information and quantum information carried by photon pairs. Specifically, we focus on the correlations within a bipartite state.

So how do we quantify or determine the correlation between two systems? One way to view this question is to consider the amount of information contained in each system, and the total amount of information contained in the two systems. We can look at three examples. In the first case, if the two systems are uncorrelated, meaning that they are completely independent with one another, then the total amount of information in the two systems should equal the sum of information in each individual system. In the second case, if the two systems are completely correlated with each other, then the information in one system is totally predictable if the information in the other system is measured. This suggests the total amount of information in the two systems equals the amount of information in each system. In the last case, if the two systems are partially correlated, then the measured information in one system can partially dictate the information in the other system, leaving some uncertainties in the whole. The total amount of information is less than the sum of information in each system. Therefore, in summary, if we can quantify the amount of information in a system, then we can define the correlation of two systems based on it.

Information entropy is a measure of the average amount of information produced by a stochastic source of data. The more unpredictable the system is, the higher its entropy is. In the classical information theory, people use Shannon entropy ($H(X) \equiv -\sum_i p_i \log_2 p_i$) to quantify the information of a source X that produces outcome $\{X_i\}$ with a probability $\{p_i\}$. To understand the rationale behind this definition, we can consider the Shannon entropy as the average minimum amount of "yes or no" questions to be asked to determine the result of a measurement of X. For example, if the probability of getting X_i is p_i, then we need to ask at least $\log_2(\frac{1}{p_i}) = -\log_2 p_i$ questions to get the answer X_i, and the probability of asking $-\log_2 p_i$ questions is p_i. Therefore, if we sum up all the weighed possible outcomes, we can get the information entropy as $-\sum_i p_i \log_2 p_i$. Now consider we have another system Y that produces messages $\{Y_j\}$ with a probability q_j, then the Shannon entropy of Y is $H(Y)$, and the Shannon entropy of the combination of the two systems is $H(X, Y) = -\sum_i p_{ij} \log_2 p_{ij}$, where p_{ij} is the joint probability of outcomes X_i and Y_j both occurring. Therefore, in accordance with our qualitative discussion of correlation between two systems, we can define the mutual information between the two systems as $H(X : Y) = H(X) + H(Y) - H(X, Y)$. This mutual information indicates the amount of information shared by the two systems; the higher the value, the more correlated the two systems are. If the two systems are independent, then $H(X) + H(Y) = H(X, Y)$, meaning that the mutual information is 0.

Note that the above discussion is based on the classical information theory, where the outcomes of a system are deterministic with some probabilities. In the quantum regime, however, since the outcome of a measurement may occupy multiple classical results simultaneously, people use quantum mechanics to describe the physics. In quantum mechanics, a measurement is represented as an operator $(\hat{A})$ on a state, which is represented by a density matrix ρ. The result of the measurement is represented by eigenvectors of $\hat{A}\rho$ with probabilities of their eigenvalues. To quantify the entropy of a quantum system, we can use the Von Neumann entropy $(S(\rho))$, where $S(\rho) = -\text{Tr}(\rho \log \rho)$. In this definition, the density matrix ρ is diagonalized. We can see that if the density matrix represents a classical state, then the eigenstates of the density matrix are just the classical outcomes with probabilities equaling their eigenvalues, therefore, the Von Neumann entropy equals the Shannon entropy. We can also see that if the density matrix represents a pure quantum state, then its information entropy based on the classical measurement will be greater than 0 because the measurement will give multiple outcomes. However, its information entropy based on the quantum measurement will be 0 because the state is pure $(S(\rho) = 1 \log 1 = 0)$; the state is a superposition of different classical states. The difference between the classical theory and the quantum theory originates from the special correlations between the classical states; the information entropy of the system decreases due to the additional special correlations between the classical states. We can define this special correlation as quantum correlation.

We can use the Von Neumann entropy to study the correlation between two systems (A and B). Assuming the density matrix of each individual system is ρ_A and ρ_B, then the Von Neumann entropy for the two systems are $S(\rho_A)$ and $S(\rho_B)$. And the Von Neumann entropy of the combination of the two systems is $S(\rho_{AB})$, where ρ_{AB} is the density matrix of the composite system. Then the correlation (mutual information) between the two systems is $I(\rho_{A:B}) = S(\rho_A) + S(\rho_B) - S(\rho_{AB})$ [83]. Note that this definition is in accordance with the mutual information in the classical case as discussed above. In the quantum case, since the Von Neumann entropy is equal or smaller than the Shannon entropy, the mutual information is greater or equal than its classical representation due to the possible quantum correlation. Therefore, this leads to the subject of characterizing the classical correlation and quantum correlation within the mutual information among systems. Also, the characterization has significant practical implications as the classical and quantum correlations of various systems can lead to the potential applications in different subjects.

As far as we know, the mutual information (I) contains two and only two parts, namely the classical correlation (C) and quantum correlation (Q). We can also quantify the mutual information. Therefore, if we can find a way to quantify the classical correlation, then we can obtain the quantum correlation based on the simple relation $Q = I - C$. The classical correlation is the intersection of the information in subsystems A and B. We know the amount of information in subsystem A is $S(\rho_A)$. If we measure the subsystem B in an arbitrary basis B_i, where $B_i^\dagger B_i$ is a

positive-operator valued measure (POVM), then the amount of information in the post-measurement state of the subsystem A is $\sum_i p_i S(\rho_A^i)$, where $\rho_A^i = \mathrm{Tr}_B(B_i \rho_{AB} B_i^\dagger)/\mathrm{Tr}_{AB}(B_i \rho_{AB} B_i^\dagger)$ is the post-measurement state of the subsystem A after obtaining the outcome i with probability p_i on the subsystem B. Imagine a maximally correlated classical state $(|H_A H_B\rangle + |V_A V_B\rangle)/2$ is measured in the diagonal-antidiagonal basis, the classical correlation is still contained in the post-measurement state of the subsystem A. Therefore, to fully recognize the classical correlation, researchers have proposed a measure of classical correlation between two systems (A and B) as [83]

$$C(\rho_{AB}) = \max_{B_i^\dagger B_i} \left[S(\rho_A) - \sum_i p_i S(\rho_A^i) \right], \qquad (2.147)$$

In this definition, the maximum of the set indicates that the classical correlation is found by performing the POVM $B_i^\dagger B_i$. Therefore, the quantum information is directly obtained by the relation $Q = I - C$.

We are extremely interested in a special type of quantum correlation, namely the entanglement (E_n) because it's a crucial criterion for realizing quantum information protocols in a decohering environment. Entanglement between two subsystems quantifies how distinguishable the whole system is from the "nearest" separable state, as given by [83]

$$E_n = \min_{\sigma_{AB} \in D} [S(\rho_{AB}) - \mathrm{Tr}(\rho_{AB} \log \sigma_{AB})], \qquad (2.148)$$

where D represents the set of all separable or disentangled states.

Here we will be studying some examples of bipartite systems. First, we characterize the correlation of an uncorrelated state

$$\rho_0 = (|H_A H_B\rangle\langle H_A H_B| + |H_A H_B\rangle\langle V_A V_B| + |V_A V_B\rangle\langle H_A H_B| + |V_A V_B\rangle\langle V_A V_B|)/4, \quad (2.149)$$

where A and B are the two subsystems. Then we study the correlations of classical and quantum states, including

$$\rho_1 = (|H_A H_B\rangle\langle H_A H_B| + |V_A V_B\rangle\langle V_A V_B|)/2, \quad\quad (2.150)$$

And

$$\rho_2 = |\Phi^+\rangle\langle\Phi^+|, \quad\quad (2.151)$$

where $|\Phi^+\rangle = (|H_A H_B\rangle + |V_A V_B\rangle)/\sqrt{2}$, is a maximally entangled pure state (Bell state).

For ρ_0, clearly, the mutual information, classical correlation, and quantum correlations are 0, because the two subsystems are completely independent with each other. For ρ_1, $I = C = 1, Q = 0$. We see that if A gives the outcome $|H_A\rangle$ ($|V_A\rangle$), then B must give $|H_B\rangle$ ($|V_B\rangle$), and that A (B) must be deterministic in one of the state, hence no superposition which means the state is classic. For ρ_2, however, $I = 2, C = Q = 1$. The difference between ρ_1 and ρ_2 is that the state can be $|H_A H_B\rangle$ and $|V_A V_B\rangle$ in the same time, which is described by the quantum correlation.

3 Chapter3. Experiments and Results

In this chapter, we will talk about the way we measure the $\chi^{(3)}$ nonlinearity of EGFP through the z-scan measurement, the way we create photon pairs via SpFWM, and the way we generate and characterize the entanglement from the created photon pairs. Here are some key results; in the z-scan measurement, we obtain the two-photon absorption coefficient $\beta = 0.05 \pm 0.03$ cm/GW and the nonlinear refractive index $\gamma = 10^{-19}$ m^2/W at 785 nm. In the SpFWM, we observed high-purity correlated photon pairs with a coincidence-to-accidental ratio (CAR) of ~147 from the EGFP, which is much greater than that from other laser dyes. We also created high-fidelity two-photon polarization-entangled state from the correlated photon pairs.

3.1 Z-scan measurement
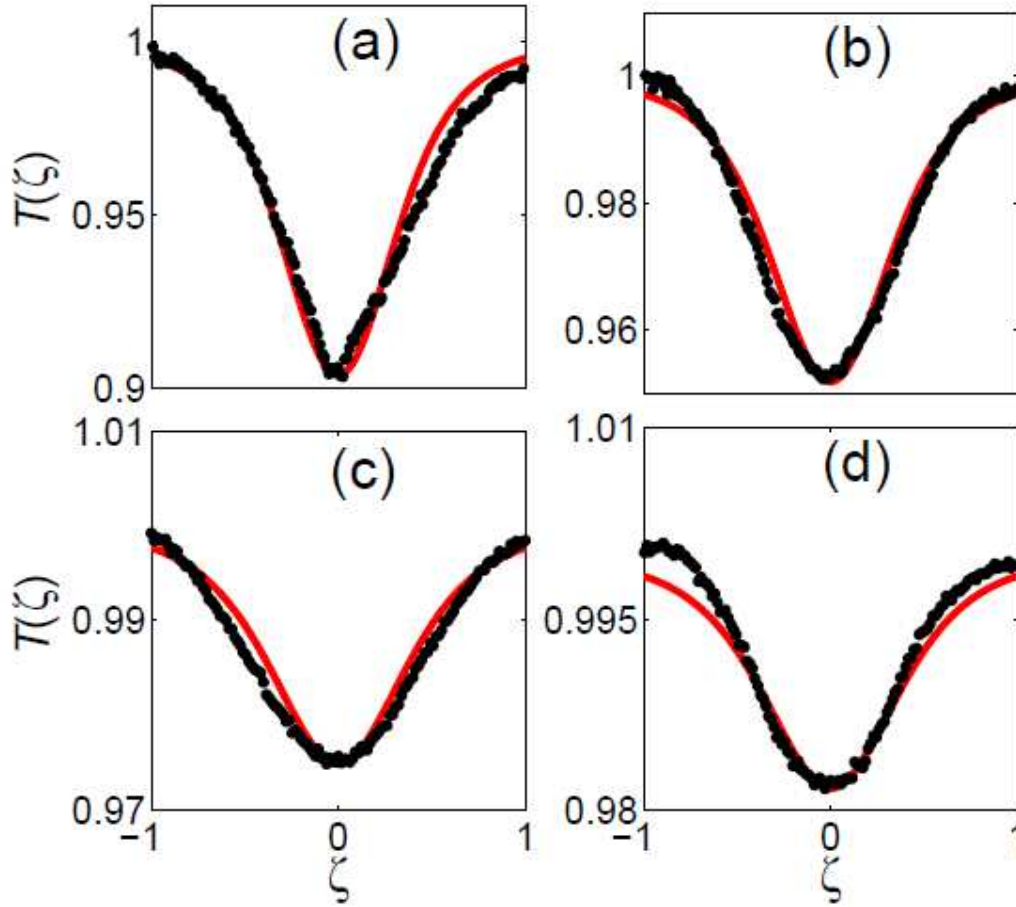
The transmittance of the z-scan as a function of $\zeta=z/2z_0$ with open aperture at different peak intensities: (a) I_p=60 GW/cm^2, (b) I_p=120 GW/cm^2, (c) I_p=180 GW/cm^2 and (d) I_p=240 GW/cm^2. Solid red curves are least square fit to the data.

To utilize the $\chi^{(3)}$ nonlinearity of EGFP through SpFWM for photon-pair generation, we need to perform the z-scan measurement for carefully characterizing its nonlinearity. As discussed in chapter 2, the z-scan measurement contains both the open and closed aperture schemes for estimating the real and imaginary part of $\chi^{(3)}$. The success of z-scan technique relies on focusing a well-defined Gaussian beam onto the nonlinear sample. In our experiment, we use a mode-locked regenerative amplifier

(Coherent, Model RegA-9000 seeded by Mira-900, and pumped by Verdi-10) that

emits a Gaussian-shaped pulse centered at 785 nm, with a width of 200 fs and a

repetition rate of 13 KHz. In both experiments, we use two detectors for detecting the

transmitted beam and for detecting the reference beam that comes from the beam

splitter. The reference beam is used for recording the jittering of the incoming beam

to compensate for the power fluctuation of the transmitted beam. The beam is then

transmitted through the sample (EGFP) with a molar concentration of 30 μM stored

in a spectroscopic quartz cuvette (thickness L = 1 mm) mounted on a

computer-controlled motorized translation stage. At the focal point, the beam waist of

laser is measured as $\omega_0 = 40 \pm 2$ μm, which correspond to a confocal parameter

(twice the Rayleigh range) of $z_0 = 13.9$ mm. Therefore, the thickness of the cuvette,

relative to the confocal parameter of the laser beam, satisfies the thin sample criterion

(L $\ll z_0$). In each experiment, we translate the sample along the beam through the

focal point and measure the transmittance. Note that the real experiment may not be

as ideal as the theory predicts due to various sources of errors. For example, in this

z-scan measurement, the thermal effect is a major concern. Since we use

high-intensity laser pulses with peak irradiance of ~200 GW/cm^2 to have an

observable effect, if the EGFP is pumped too frequently, then the protein may be

photochemically altered and permanently unable to fluoresce. This effect is known as

photobleaching (sometimes termed fading) and is harmful for photon-pair generation

as well as the characterization of $\chi^{(3)}$. Therefore, we need to operate the pumping

frequency below the threshold of 80 kHz when photobleaching becomes effective [84, 85]. That's why we choose to operate the laser at a relatively low repetition rate of about 13 kHz.

For the open-aperture scheme, we vary the laser peak power and record the beam's transmittance with respect to the normalized sample position ($\zeta = \frac{z}{2z_0}$) as shown in Fig. 3.1. As expected, we can see all four figures show dips around the focal point due to the process of two-photon absorption which reduces the transmittance of the pump power. We also see an interesting phenomenon when comparing the depth of the valleys of the four cases. Ideally, as we increase the laser peak power, we would expect a stronger absorption of pump pulses since the rate of TPA is proportional to the square of the field intensity, thus the depth of the dip will deepen according to the increasing power. However, Fig. 3.1 clearly shows that the depth of dip decreases as we increase the pump power. This interesting phenomenon tells us that the absorption of the pump displays a saturation behavior, which means that the TPA coefficient β is dependent on the pump power as given by

$$\beta(I) = \beta(0)/\sqrt{1 + I^2/I_s^2}, \tag{3.1}$$

where I is the irradiance, I_s is the saturation intensity, and $\beta(0)$ is the unsaturated TPA coefficient. The origin of this phenomenon is that the fluorophores cannot respond to the high pump power effectively because they have already been excited via the TPA process. Therefore, we can obtain the saturation intensity I_s and the

TPA coefficient β based on Fig. 3.1. By using the numerical curve fitting, we obtain

$I_{sat} = 10 \pm 1$ GW/cm^2 and the TPA coefficient $\beta = 0.05 \pm 0.03$ cm/GW. These

values are consistent with the measurements reported in [86].
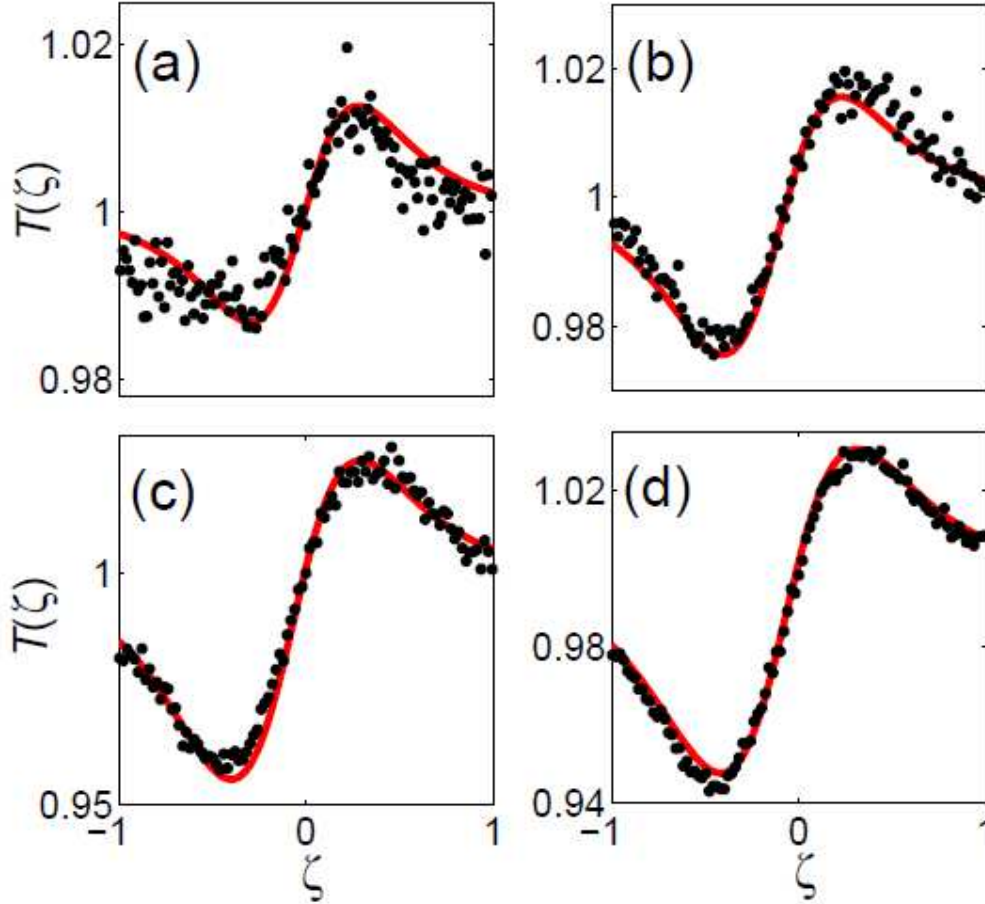
Figure 3. 2

The transmittance of the z-scan as a function of $\zeta=z/2z_0$ with closed aperture at different peak
intensities. (a) I_p=60 GW/cm^2, (b) I_p=120 GW/cm^2, (c) I_p=180 GW/cm^2 and (d) I_p=240 GW/cm^2. Solid
red curves are theoretical fits to the data.

Next, we move on to estimate the real part of the $\chi^{(3)}$ by comparing the pump

transmittance in the closed-aperture scheme to that in the open-aperture scheme. Fig.

3.2 shows the pump transmittance of the z-scan with closed-aperture scheme at

different pump peak intensities corresponding to the open-aperture scheme. The valley-peak transmittance pattern indicates that the sample works as a convex lens, which means the real part of $\chi^{(3)}$ is positive. In the absence of TPA, the data are symmetric with respect to the peak and the valley. However, in the presence of TPA the valley becomes deeper and the peak is correspondingly reduced. To estimate the pure refractive z-scan transmittance from the experimental results for curve fitting, we divide the closed aperture z-scan transmittance by the open aperture z-scan transmittance. The divided result appears to be a z-scan transmittance without nonlinear absorption process. In fact, the result agrees to the z-scan transmittance from a purely refractive z-scan within 10% error. We numerically fit the divided result and obtain the nonlinear refractive index $n_2 = 10^{-19}$ m^2/W.

3.2 Stimulated four-wave mixing

Our core objective is to generate entanglement from the biological system through SpFWM. As a pre-step, we need to study the StFWM for two reasons. First, StFWM process is a good test for characterizing the nonlinear responses of the samples because a good photon-pair source would require a relatively large $\chi^{(3)}$ response. Second, the experimental setup of StFWM serves as the foundation of the SpFWM experiment since the alignment of optical components for SpFWM depends largely on the alignment for the StFWM process. Therefore, before we discuss the generation of photon-pair through SpFWM process, we focus on the study of StFWM process. In

this section, we first demonstrate the experimental setup, then we characterize the

efficiency of StFWM for 5 different organic molecules.

3.2.1 Experimental setup
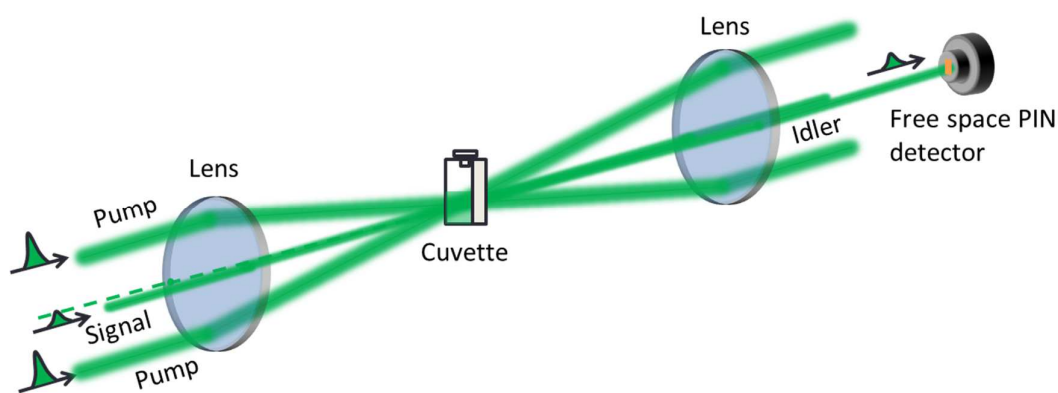
Experiment setup for the stimulated four-wave mixing. Two pump pulses and one signal pulse interact in the sample to create an idler pulse that is detected by a free-space PIN detector.

The experimental setup is shown in Fig. 3.3. The laser system consists of a

Titanium:Sapphire modelocked oscillator (Mira 900), a Titanium:Sapphire

regenerative amplifier (RegA 9000), a diode-pumped CW laser (Verdi-V8) that

pumps the Mira 900, and another diode-pumped CW laser (Verdi-V10) that pumps

the RegA 9000. The Mira 900 produces the 76 MHz laser pulse train with a typical

pulse duration of 200 fs at the center wavelength of 785 nm. Then, the 76 MHz

laser pulse train is sent to RegA 9000 for amplification. In details, the amplification

process contains three steps. First, the 76 MHz photodiode signal from the Mira 900

is used to generate a 38 MHz master clock for the timing of all the RegA 9000 RF pulses. The controller box of the RegA 9000 divides this 38 MHz clock so that we can operate the amplified laser at the repetition rate of 10 to 300 KHz. Second, an acousto-optic modulator, which is part of the Q-switching component, is used to prevent lasing in the RegA 9000 cavity until a pulse from the Mira 900 is injected. The Q-switch helps store energy for the amplification of the injected pulses. Last, another acousto-optic modulator for cavity dumper is used to inject and eject the single pulses in the RegA 9000 cavity. Through this amplification process, we operate the laser system to emit high-power laser pulses centered at 785 nm with a repetition rate of 40 kHz, and a pulse duration of 200 fs.

The emitted laser is then split into two pump beams and one probe beam by using beam splitters. The two pump beams are of similar power (~50 mW) while the probe beam is much weaker (~100 μW). We control the power of the three beams by using a half-wave plate (HWP) and a polarizing beam splitter (PBS, not shown in Fig. 3.3). The three spatially separated and co-polarized beams are focused inside the sample by using a lens of $f_1 = 50$ cm. The beam waist for each beam is about 40 μm. Two delay-lines, one for probe beam and one for pump beams (not shown in Fig. 3.3), are used to compensate the path differences among the three beams so that they arrive at the focal point simultaneously to participate in the StFWM. Behind the sample, a lens ($f_2 = 2f_1 = 100$ cm) is used to collect and collimate the generated idler photons for detection. The probe arm is defined as the signal arm, and the opposite arm is defined

as the idler arm. The signal and idler photons must satisfy both the energy and momentum conservation laws as pictured in a phase-matching cone in <u>Fig. 3.4</u>. We see that the energy conservation law and phase-matching condition require the idler beam to be centered at 785 nm and propagate along the same cone with the other three beams. Since the two pump beams propagate in a vertical plane and the signal propagate in a horizontal plane, the idler beam must propagate in the horizontal plane symmetric to the signal beams.

Phase matching cone
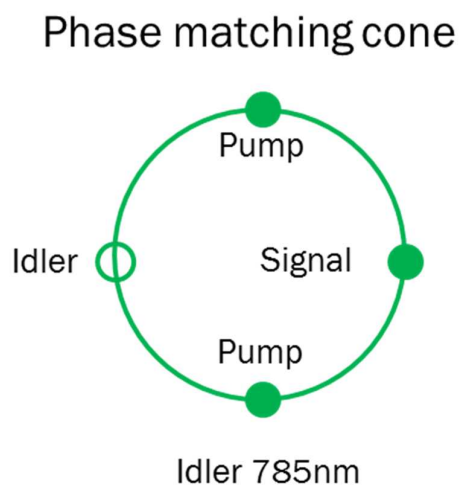
Figure 3. 4

Phase matching cone of the stimulated four-wave mixing with the degenerate wavelengths i.e. $\omega_p = \omega_i = \omega_s$

In this experiment, a sample is kept in a 5-mm long cuvette. The cuvette is fixed on a motorized translation stage with two degrees of freedom; one is along the z-axis and defined as the normal line to the surface of the cuvette, and the other is along the y-axis and defined as the vertical direction. Since the three beams are spatially

separated in front of the lens, the sample needs to be precisely located in their focal region. To locate the sample in the proper place, we characterize the focal region is measured in the following way. We scan the translation stage along the z-axis and record the power of the idler beam with respect to z. We expect the power to be greater when the sample is nearer to the focal point. Experimentally, we can see the power increases and then decreases as we scan the sample, showing a Gaussian-shaped curve. By fitting the curve with a Gaussian function, we obtain its full width at half maximum (FWHM) of around 14 mm. Since the cuvette is 5 mm long, the effective focal region is calculated to be around 9 mm, which is longer than the cuvette. With the help of the characterization, we can place the sample at z=0 for the experiment.

The major noise in this experiment originates from the scattering of pump beams into the detector since the pump power is too strong, even a little amount of scattering may be comparable to the power in the idler beam. To reduce the scattering of pump beams into signal/idler arms, we use the spatial filtering (as shown in Fig. 3.3) because the spectral filtering will block the idler beam too. In addition, we use the experimental techniques for reducing the scattering. That is, we block the signal beam while leaving two pump beams passing through the sample. In this scenario, what we detect in the idler channel is the pure pump scatterings. Then, if we slightly adjust the position of the sample along the x-axis and the y-axis, we could reduce the scattering even more. As a result, we can reduce the pump scattering by spatial filtering and

experimental techniques so that the power of pump scattering is much less than that of

the generated idler beam.

3.2.2 Result
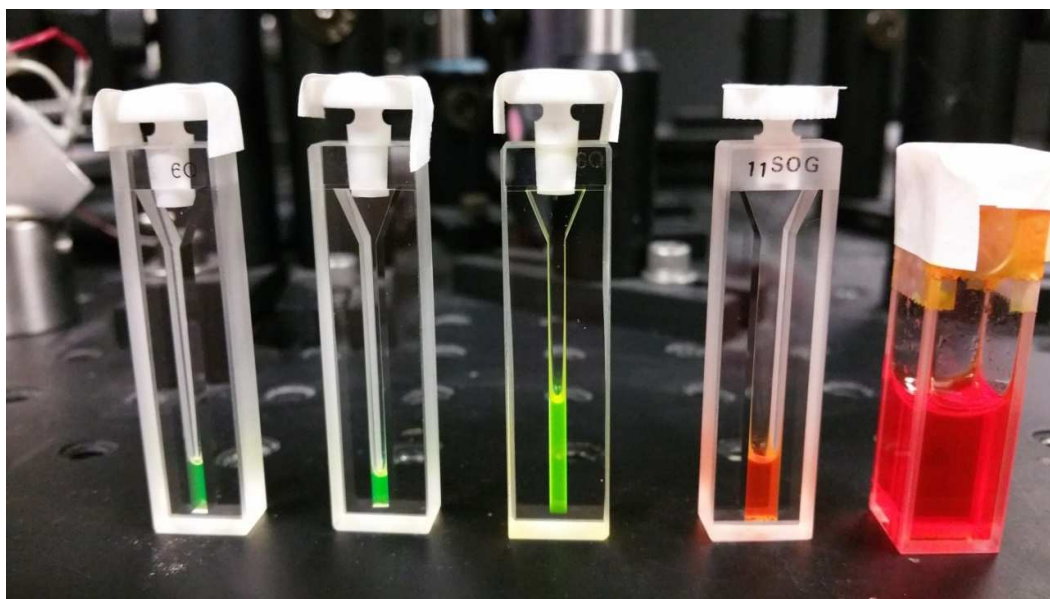
Figure 3. 5

The 5 samples used in experiments. They are (from left to right) GFP with a molar concentration of 25.5 μM in phosphate buffered saline, pyrromethene 546 with a molar concentration of 250 μM in methanol, pyrromethene 556 with a molar concentration of 4.3 mM in ethylene glycol (EG), DCM with a molar concentration of 0.99 mM in ethanol and DCM with a molar concentration of 1.5 mM in mixed solution of benzyl alcohol/ethylene glycol (BzOH/EG) with a ratio of 2/3.

We characterize the efficiency of five different samples, including (1) EGFP with a

molar concentration of 25.5 μM in phosphate buffered saline solution, (2)

pyrromethene 546 with a molar concentration of 250 μM in methanol solution, (3)

pyrromethene 556 with a molar concentration of 4.3 mM in ethylene glycol (EG)

solution, (4) DCM with a molar concentration of 0.99 mM in ethanol solution and (5)

DCM with a molar concentration of 1.5 mM in mixed solution of benzyl alcohol/ethylene glycol (BzOH/EG) solution with a ratio of 2/3. We prepare each sample with a concentration according to the vendors. The solvents (phosphate buffered saline, ethanol, BzOH/EG, EG and methanol) do not contribute to FWM efficiency. The reason that we choose these five samples are two folds. First, their fluorescent peaks are different; roughly saying, DCMs emit red light, pyrromethene 556 emits yellowy green light, while the pyrromethene 546 and EGFP emit green light. Second, EGFP has a unique protective β-barrel structure that the other dyes don't have. In details, the EGFP fluorophores are enclosed in the protective shell (β-barrel) that consists of eleven beta-sheets. Each beta-barrel sheet is 2.4 nm in diameter and 4.2 nm in height as shown in Fig. 3.6. Researches show that at high molar concentrations, the fluorophores of synthetic dyes without the structure tend to collide/aggregate, leading to self-quenching by unproductive donor-donor transfer [87]. The process can be harmful to the efficiency of the FWM process. In contrast, biologically produced fluorescent proteins seem to immune the colliding/aggregating thanks to the β-barrel structure; they retain their high brightness even at the highest molar concentration in solid state. The reason is that the β-barrel structure acts as bumpers to prevent close contact between fluorophores; it provides optimal balance between high protein molar concentration and low resonance energy transfer self-quenching[53]. Specifically, the EGFP is effective for a molar concentration that is higher than 1 mM [53]. We can compare this critical molar concentration (1 mM) to

our samples. This critical value is much higher than that of EGFP (25.5 μM), and higher than that of pyrromethene 546 (250 μM), but close to the 0.99 mM for DCM in ethanol, 1.5 mM for DCM in BzOH/EG, and the pyrromethene 556 (4.3 mM). We may experience some self-quenching in DCM samples and pyrromethene 556, but not in EGFP or pyrromethene 546. In summary, we have learnt that the β-barrel structure can prevent the fluorophores from close contact with each other. In the next several sections, we will observe that the fluorescent peaks and the β-barrel structure can render other properties to the generated photon pairs which we will discuss later.
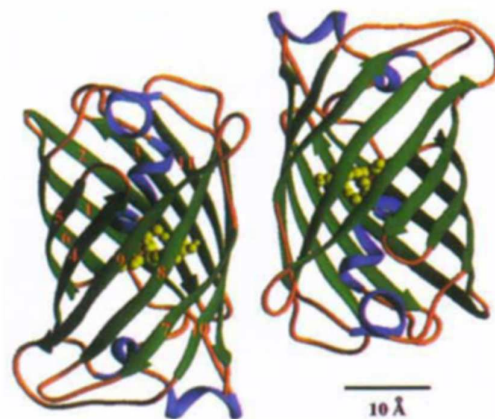
Figure 3. 6

The **β**-barrel structure of the EGFP.

We contain every sample in the 5-mm long quartz cuvette as shown in Fig. 3.5 for comparing their StFWM efficiencies, which is defined as the power of idler over the power of signal. We expect the efficiency to be proportional to the square of the pump power as StFWM is a $\chi^{(3)}$ process. We plot the efficiencies of the StFWM process of the five samples with respect to the pump power as shown in Fig. 3.7. We observe

that each sample possesses a considerable large $\chi^{(3)}$ nonlinearity at around 785 nm which confirm that four-wave mixing process occurs in all these samples. Our measured efficiencies of these samples are comparable to the efficiency of dyes in thin films [srep25–28] ranging from 0.01% to 1%. Of all the 5 samples, DCM with BzOH/EG has the highest efficiency. The rest four samples exhibit similar $\chi^{(3)}$. Note that despite the molecular aggregation, the StFWM efficiency should be proportional to the molar concentration of each sample, since every fluorophore can only participate once in the StFWM process during one cycle of pulses. This means that the higher the concentration, the more fluorophores are involved in the process, and the higher the efficiency of the StFWM. Therefore, even if the EGFP sample shows the lowest efficiency, it still exhibits the highest efficiency per fluorophore. The reason is that the EGFP sample has the lowest molar concentration (25.5 μM), which is around one-to-two orders of magnitude less compared to the other four samples (250 μM for pyrromethene 546, 0.99 mM for DCM in ethanol, 1.5 mM for DCM in BzOH/EG, and 4.3 mM for pyrromethene 556).
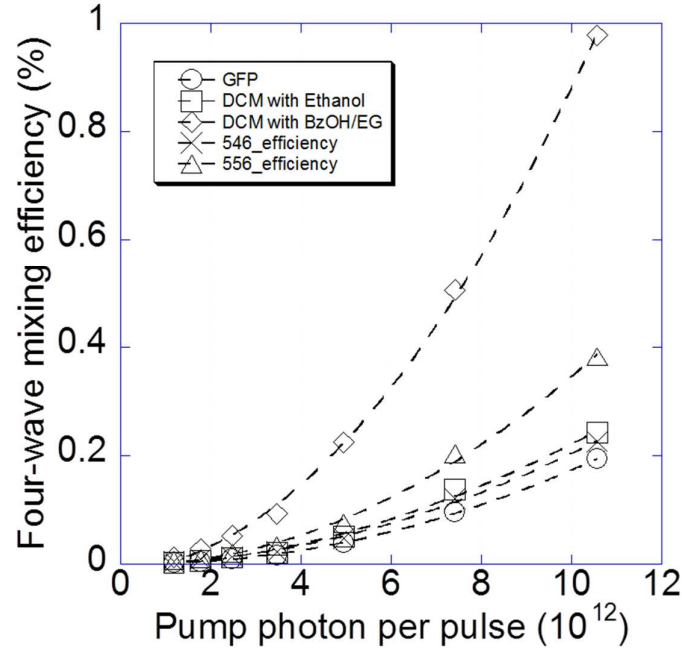
Stimulated four-wave mixing efficiencies of 5 samples

3.3 Spontaneous four-wave mixing

In the previous section, we have observed that the DCM sample shows a higher FWM efficiency than that of the EGFP. But how about the quality of the photon pairs generated through the SpFWM? Will the DCM sample proven to be better than the EGFP sample? In this section, we specifically investigate the SpFWM process to answer this question. First, we will introduce the experimental setup. Then, we will briefly talk about the alignment procedure. And then, we will describe our detection

system. Lastly, we will analyze the properties of the photon pairs obtained from each

sample.

3.3.1 Experimental setup
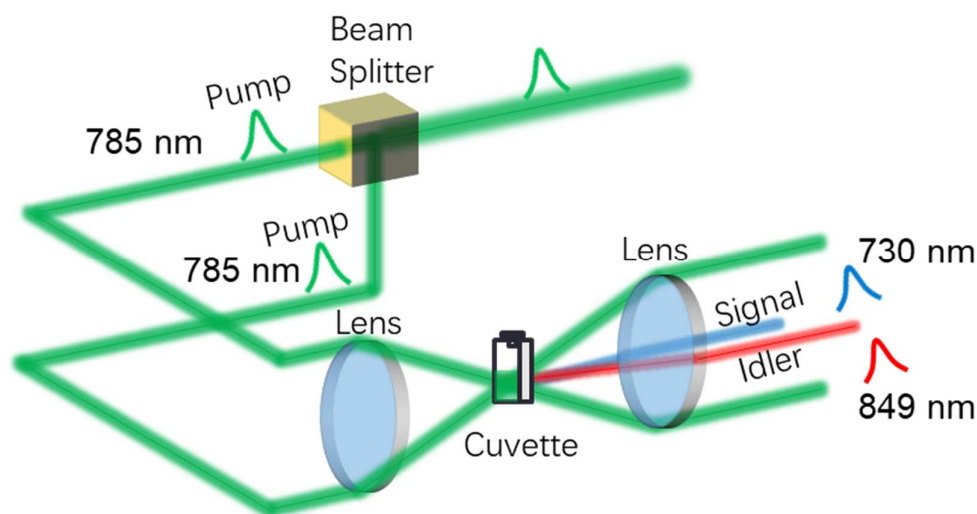
The experiment setup for the spontaneous four-wave mixing process

The experimental setup for the SpFWM process is shown in Fig. 3.8. In contrast with

the StFWM as shown in Fig. 3.3, we block the probe beam in front of the sample and

use only two pump beams for generating the signal and idler beams, which are chosen

on purpose to be non-degenerate so that we can apply the spectral filtering to reduce

the pump scattering in the signal and idler arms. In the SpFWM process, two pump

photons are annihilated to create signal and idler photons while conserving their

momentum ($2k_p = k_s + k_i$) and energy ($2\omega_p = \omega_s + \omega_i$). To reduce the chances of

capturing scattered pump photons in the single-photon detectors (SPCM-AQR-16

from PerkinElmer, dark count probability $\sim 10^{-5}$) in the signal and idler, we select the far-detuned signal and idler photons at the center wavelengths of $\lambda_s = 730$ nm and $\lambda_i = 849$ nm ,respectively. Due to the momentum conservation, the signal with a shorter wavelength propagates along its path at an angle near the z-axis, while the idler with a longer wavelength propagates along its path at an angle far from the z-axis as shown in the phase-matching cone in Fig. 3.9. After the sample, a notch filter (NF) with a 3dB-bandwidth of 33 nm at center wavelength of 785 nm is inserted to block the pump photons scattered into both signal and idler channels. As introduced before, a lens of $f_2 = 2f_1 = 100$ cm is used to collect and collimate the signal and idler. Doubling the focal length increases the spatial separation between the pump and the signal/idler by a factor of two. This enlarged spatial separation can keep the large amount of leaked pump photons away from signal and idler paths. More spectral isolations from tunable bandpass filters (TBFs) with a 3dB-bandwidth of 20 nm and single-pass transmission of 97% on each arm are introduced. The transmission wavelength of the TBFs can be tuned by changing the angle of incidence. To maximize spectral isolation two cascaded TBFs are placed on a rotation stage in signal and idler paths. As a result, the double-passing scheme with a retro-reflector provides an isolation > 140 dB from the pump photons.

Phase matching cone
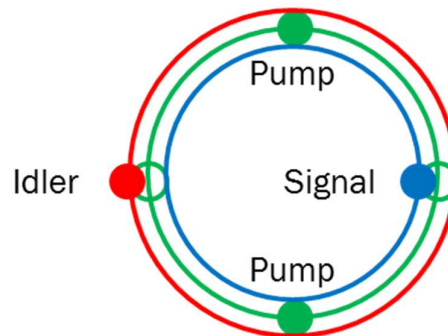
Figure 3. 9

The phase matching cone. Green dots represent the locations of two pump pulses. Green circles represent locations of the signal and idler pulses in the degenerate scenario. Red dot represents the location of the idler photon, and the blue dot represents the location of the signal photon.

3.3.2 Optical alignment for signal and idler paths

The alignment of signal and idler arms requires some tricks and efforts. Since the generated signal and idler are at the single photon level with a broad spectrum, we cannot use them for alignment, instead, we need to use two continuous wave (CW) lasers at 730 nm and 849 nm for the alignment. In addition, we need to tune the TBF in the right angles for exactly capturing the 730 nm photon in the signal arm and the 849 nm photon in the idler arm. For the signal channel, the TBF is tuned to roughly transmitting 730 nm CW laser and then coupling into an optical spectrum analyzer (OSA). Then, we precisely setting the angle of the TBF for the 730 nm photons by relying on the recorded spectrum while we scan the angle of TBF. In a similar way, the angle of the TBF on idler arm can be tuned with the help of the 849 nm CW laser.

Once the TBFs are ready, our objective becomes to send the signal/idler to the SPCMs with a high coupling efficiency through the free-space-to-fiber collimator. As shown in the phase-matching cone, the signal and idler paths are predictable in the horizontal plane. Therefore, by shifting the signal and idler beams along the horizontal plane, we can find the proper location for detecting the generated photons with high coupling efficiencies. Therefore, we can use the translation stages that hold the retro-reflectors to shift the beam paths as desired. As a result, the signal and idler paths can be shifted to overlap with their classical counterparts. We summarize the brief alignment procedures as three steps. Firstly, we perform the classical StFWM experiment and align the classical signal and idler paths into the fiber collimator with the coupling efficiencies greater than 90%. Secondly, we block the probe beam and run the SpFWM experiment. Note that since the collimators are aligned for the classical signal and idler paths, we have extremely low photon counts due to the TBFs. Thirdly, we shift the translation stages in the correct directions and observe increasing photon counts on each arm. The reason is that, according to the phase matching condition, the shift of the translation stage is equivalent to the shift of the spectrum that is detectable by the SPCM. When the detectors' spectrums match the spectrums of TBFs, or in other words, the photon counts reach their peak values, the experimental setup is aligned properly. After the alignment, we measure the total detection efficiencies for the signal and idler photons as 27% and 23%, respectively.

3.3.3 Detection system
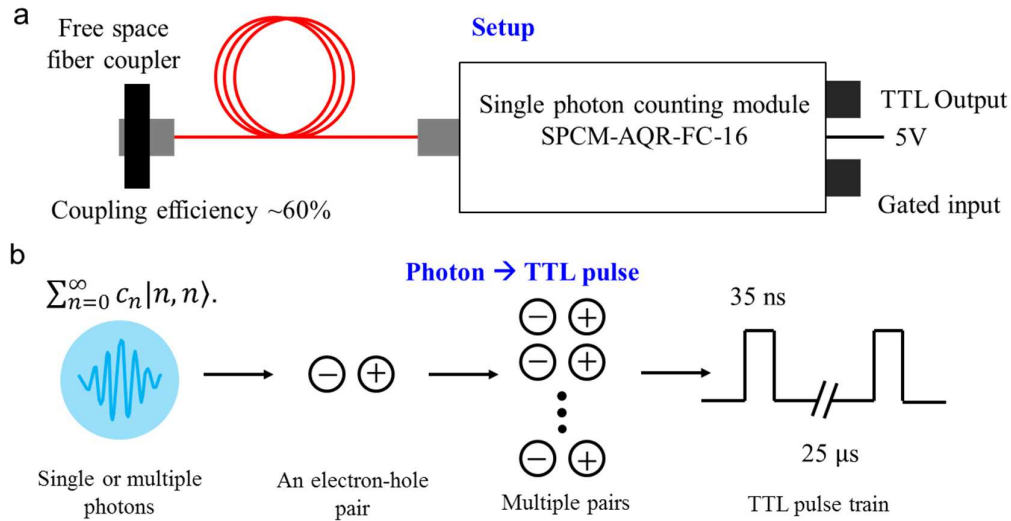
Figure 3. 10

a. An illustration of the photon counting system. Photons are coupled into the single photon counting module (SPCM) via a free-space fiber coupler with a coupling efficiency of ~60%. The SPCM is powered by a 5V DC power supply.

b. The process of converting a photon to a TTL pulse. The SPCM uses a silicon avalanche photodiode with a circular active area for capturing the photon. As each photon is detected, a TTL pulse of 2.5V (minimum) high in a 50Ω load and 35ns wide is output at the rear BNC connector.

The generated photonic state from the SpFWM process is a joint thermal state $\sum_{n=0}^{\infty} c_n |n, n\rangle$, with $c_n = \frac{1}{\bar{n}+1}\left(\frac{\bar{n}}{\bar{n}+1}\right)^n$, where $\bar{n}$ is the average number of photons. The correlation between the photons in signal and idler arms is obvious, meaning that they will always come as a pair or multiple pairs. In our experiment, even with an average pump power of 50 mW (which is the highest power we used) on each arm, $\bar{n}$ is on the order of 0.001, suggesting that there is a high probability (~0.999) of not generating any photon, a low probability (~0.001) of generating a photon pair, and an extremely low probability (~0.000001) of generating multiple photon pairs. As shown

in [Fig 3.10](#) a and b, the photon pairs are then coupled into the single photon counting modules (SPCM-AQR-FC-16) via the free-space fiber coupler with a coupling efficiency of ~60% on each arm. The core part of the SPCM is a reverse-biased P-N junction that builds an avalanche photodiode. Within the detector, the absorbed photons will create an electron-hole pair that leads to multiple electron-hole pairs, which result in a measurable current. The circuit board in the SPCM will then convert the current to a TTL pulse train with a rising time ~1ns and a width of 35ns. The specifications of the SPCM can be found in the manual. The important parameters for our experiment are listed in the following table.

Photon detection efficiency	65% (at 730 nm), 45% (at 849 nm)
Dead time	50 ns
Dark count rate	25 counts/sec

The dead time of 50 ns means that the SPCM can only report the detection of a single photon within 50 ns, regardless of how many photons are within the 50 ns duration. This will have negligible effect our result because we have an extremely low probability of having multiple photons within one cycle. Also, since the laser operates at a repetition rate of 40 kHz, the dead time (50 ns) is much shorter than the temporal interval of adjacent photon pairs (25 μs), meaning that the detector is ready to detect the next incoming photon. However, the dark count rate could be high enough to affect our result because the single-counts rate is expected to be ~200/sec at

maximum pump power. Therefore, to reduce the dark counts, we use the following AND logic gate to filter the unexpected noise photons between the two SpFWM cycles.
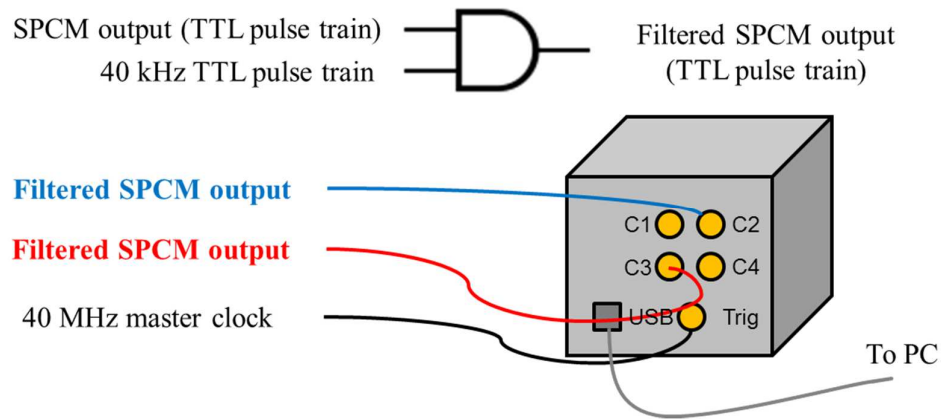
Figure 3. 11

The AND logic gate and the detection system. The AND function with a 40 kHz TTL pulse train as one input will block the noise photons when there are no generated photon pairs. The correlator will count the coincidence between the photons from the two filtered SPD output ports.

Here are the details of how to create a cleaner TTL pulse train with the help of the AND logic gate. In the experiment, we use the Correlated Photon Detection System (CPDS, Nucrypt llc) as shown in Fig. 3.11 for measuring the correlation of photon pairs. We generate the photon pairs at a repetition rate of 40 KHz, corresponding to the repetition rate of the laser system, which happens one time in every 1000 cycles of the master clock at 40 MHz. Although we wanted to trigger the CPDS at 40 KHz, the CPDS can only be triggered with MHz signals, therefore we decide to trigger it with a 40 MHz master clock. As a result, the detector dark counts and background photons are registered at a rate of 40 MHz. However, the photon pairs are generated

and registered by the correlator at a rate of 40 KHz. The difference in the repetition rates introduces 1000 times more noise photons to the photon pairs. To reduce the noise photons, we design the AND logic circuits for both detectors. The AND logic circuit has two inputs and one output. One of the inputs is a 40 KHz TTL pulse train generated via a delay generator (Stanford Research Inc, Model DG535). The delay generator is triggered by 40 KHz signal from the "Repetition Rate Synch Out" connector of the RegA 9000, which is synchronized with the laser pulse train. The other input is the output TTL pulse from the SPCM. Then the output of the AND logic circuit is connected to CPDS. These AND logic circuits isolate noise counts that arriving at 40 MHz, thus the noise count level is greatly reduced. The circuit can help to block the photons from entering the CPDS when the system is no pump pulses. As a result, the "real" counting frequency of the CPDS is reduced to 40 KHz, which is in good match with the rate of the photon pairs.

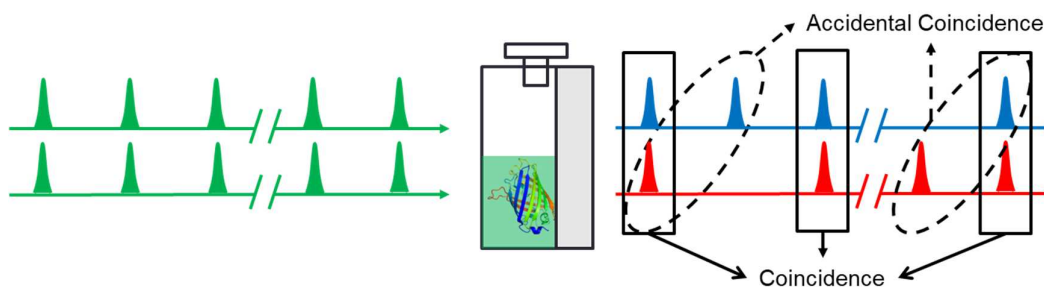### 3.3.4 Results and discussions

3.3.4.1   EGFP

Figure 3. 12

Illustration of coincidence counts and accidental coincidence counts. The signal (blue) and idler (red) pulses contain generated photon pairs and noise photons in the two detection channels. The solid rectangular loop demonstrates the coincidence counts, and the dashed oval loop demonstrates the accidental-coincidence counts.

We characterize the purity of photon pairs by measuring the coincidence-to-accidental ratio (CAR). In our detection system, a coincidence count is recorded when both SPCMs detect a photon in the same gated time interval, while an accidental coincidence count is recorded when both SPCMs detect a photon in the adjacent gated time interval as shown in Fig. 3.12. The CAR is plotted as a function of pump power (10^{12} photons/pulse) in Fig. 3.13. In Fig. 3.13a the CAR without background subtraction is shown as circles, the CAR with background subtracted is shown as crosses. Here, the background includes the detector dark counts and the environmental photons. We can obtain the background photons by blocking the laser. The peak of the CAR without background subtraction is 36, with 146 coincidence counts and 4 accidental counts. The CAR next to the peak is 31, with 282 coincidence counts and 9 accidental counts. After subtracting the background counts, we obtain a maximum CAR of about 70 at a photon-pair production rate of 10^{-5}. The peak CAR occurs at 0.5×10^{12} pump photon per pulse. The data around the peak value is taken with an integration time of 30 min. A CAR of 70 can lead to a two-photon interference (TPI) with the visibility of 96%. The signal and idler are recorded as shown in Fig. 3.13b The photon detection rates for the signal and idler (after background subtraction) are plotted with respect to pump photon per pulse. The blue data points represent the signal and the red data points represent the idler,

respectively. The photon detection rates for the signal and idler at the maximum CAR

are 0.8×10^{-4} per pulse and 2×10^{-4} per pulse, respectively.
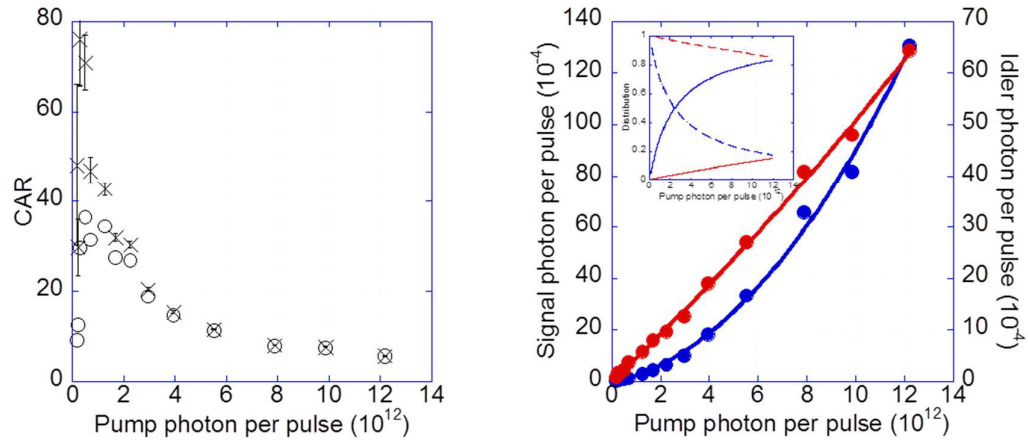
a. Coincidence to accidence ratio of GFP b. Photon detection rate of signal arm (blue) and idler arm (red)

With the help of the CAR measurement and the detailed single counts, we can explore

the quantum nonlinear interaction processes inside the EGFP during the experiment.

The detected signal and idler photons can be classified by the way they are produced.

There are background photons, Raman photons, fluorescence photons from

two-photon absorption, and photon pairs from spontaneous four-wave mixing. The

rate of background noise photons is constant. The rate of Raman photons is

proportional to the pump power. The rate of fluorescence photons is quadratically

dependent on the pump power because it is mainly induced by the TPA. And the rate

of spontaneous four-wave mixing photons are quadratically dependent on the pump power as well.

Next, we study how will the photons from different sources affect the CAR. The coincidence count is corresponding to the photon pairs generated from the spontaneous four-wave mixing, which means that the single counts in both arms are quadratically dependent on the pump power and are correlated with each other. Therefore, the coincidence counts are quadratically dependent on the pump power. The accidental is corresponding to the uncorrelated photons. We evaluate the accidental counts in two scenarios; one without the background subtraction, and the other with the background subtraction. In the first case where background photons play a role, the accidental counts can occur between the same or different sources of photons, including the fluorescence photons, background photons, Raman photons, and even the SpFWM photons. Therefore, it contains different terms ranging from 0th order to 4th order with respect to the pump power. In the second case where background is subtracted, the accidental contains less terms, but still contains different terms ranging from 2nd order to 4th order with respect to the pump power.

A proper way to start analyzing the CAR would be to fit the single counts in both channels [88]. We fit the measured signal/idler counts with the equation $N_{s(i)} = S_1 N_p + S_2 N_p^2$, where N_p is the pump photon per pulse, where S_1 and S_2 are the linear and quadratic power-dependent scattering coefficients. By fitting the data

points, we can separate the Raman photons from the photons from the TPA and SpFWM processes. We then plot the curves of $S_2 N_p^2 / N_{s(i)}$ and $S_1 N_p / N_{s(i)}$ for comparing the numbers of photons produced by the SpFWM/TPA and Raman scattering, as shown in Fig. 3.13b. The solid blue line ($S_2 N_p^2 / N_s$) and the dashed blue line ($S_1 N_p / N_s$) are for the signal arm. The solid and dashed red lines are for the photons in the idler arm. It is clearly seen that the total strength of the S_2 processes is stronger than the strength of the S_1 process at higher pump powers, especially in the signal arm, and that the strength of S_1 process is stronger than the strength of S_2 processes at lower pump powers. This phenomenon is predicted by the difference in power dependencies of different processes. What's more interesting is that the total strength of the S_2 processes are stronger in the signal channel than in the idler channel. This difference tells us that the signal contains more fluorescence and SpFWM photons than the idler channel. Because the number of photons generated from the SpFWM process is equal in both the signal and idler channels, and the detection efficiencies are similar for the two arms, we can safely conclude that more fluorescence photons are detected by the signal detector. This is in accordance with the emission spectrum of EGFP, which is centering at 510 nm with a FWHM of around 40 nm; the fluorescence photons are more easily leaked into the signal channel (~730 nm) than the idler channel (~849 nm). Therefore, we see more fluorescence in the signal than in the idler. The other interesting observation is that the strength of S_1 process in the idler channel is stronger than that in the signal channel. This is due to

more Raman photons (from Stokes scattering) are produced in idler channel than in the signal channel (from anti-Stokes scattering).
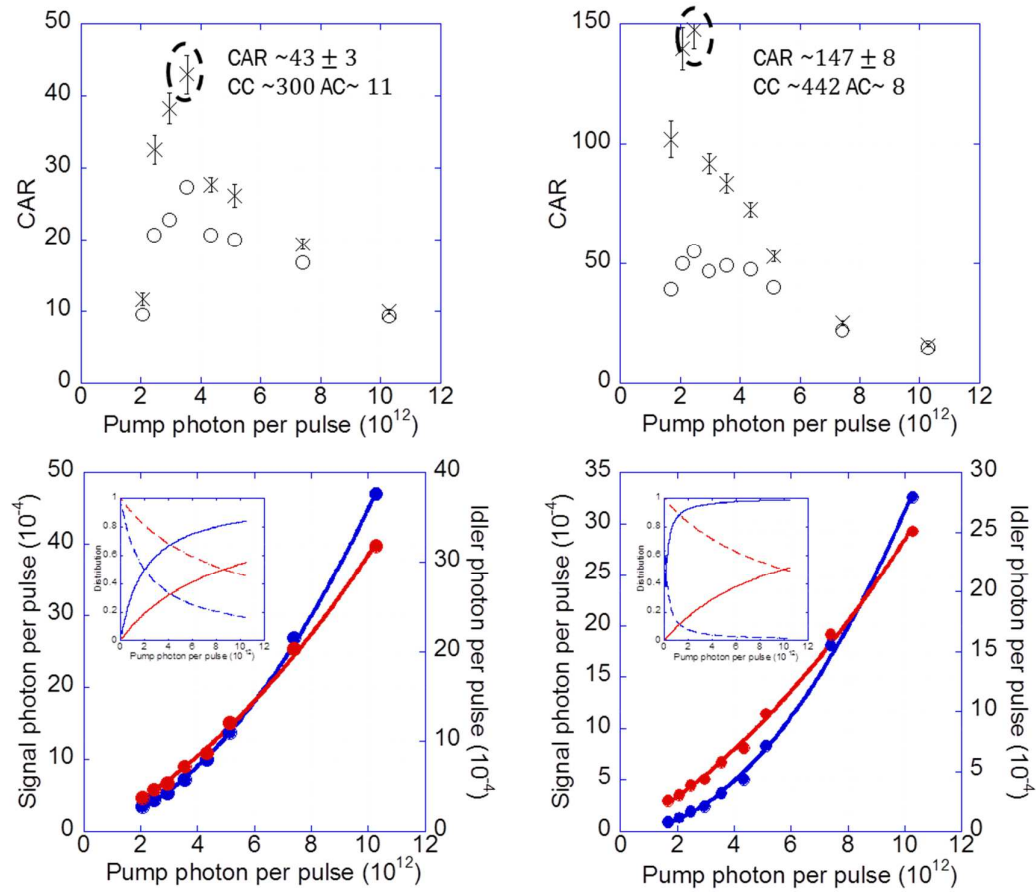
Figure 3. 14

a. Coincidence to accidence ratio of GFP without PBSs. b. Coincidence to accidence ratio of GFP with PBSs. c. Photon detection rate of signal arm (blue) and idler arm (red) without PBSs. d. Photon detection rate of signal arm (blue) and idler arm (red) with PBSs.

To increase the CAR, we can utilize the following method to introduce the polarization filtering. If both pump beams are set vertically-polarized, then the photon pairs from the SpFWM process are also vertically-polarized; however, the

fluorescence, Raman photons and background photons are always non-polarized. By using a polarizer in front of the detector, the number of noise photons can be reduced, thus increasing the CAR. Therefore, we design a new experimental scheme with the polarization filtering. Firstly, we use half-wave plates (HWPs) and quarter-wave plates (QWPs) to properly adjust both pump beams to be vertically polarized. Secondly, we introduce HWPs and QWPs on each arm to compensate the birefringence. Lastly, we insert the polarization beam splitters (PBS) in front of both SPCMs as a polarization filter to block the horizontally polarized photons which must come from the noise sources. The purity of the photon pairs in this scheme can be characterized by using the CAR measurement as shown in Fig. 3.14. In contrast with the previous result without the polarization filtering, it is clearly seen that the peak of the CAR (without background subtraction) jumps from 27 to 55. More astonishingly, after the background subtraction, the CAR leaps from 43 to 147, which is more than 3 times increment. We then break the single counts down into $S_2 N_p^2 / N_{s(i)}$ and $S_1 N_p / N_{s(i)}$ as plotted in Fig. 3.14 for understanding the processes involved in this experiment. Clearly, having the PBSs in front of the detectors will reduce the counts from fluorescence and Raman photon in the detectors by around half. As a result, $S_2 N_p^2 / N_s$ has increased in signal arm because it contains the photons from SpFWM process that is unaffected by the polarization filtering. However, for the idler arm, $S_2 N_p^2 / N_i$ remains the same with or without the polarization filtering. It implies that we may have stimulated Raman photons in the idler arm that are unaffected by the

polarization filtering. This stimulated Raman photon cannot be blocked by PBS as they are vertically polarized and therefore preventing $S_2 N_p^2 / N_i$ from increasing in the idler arm. The stimulated Raman photon is much less in the signal channel because the strength of Raman effect is much stronger in the idler channel than in the signal channel.
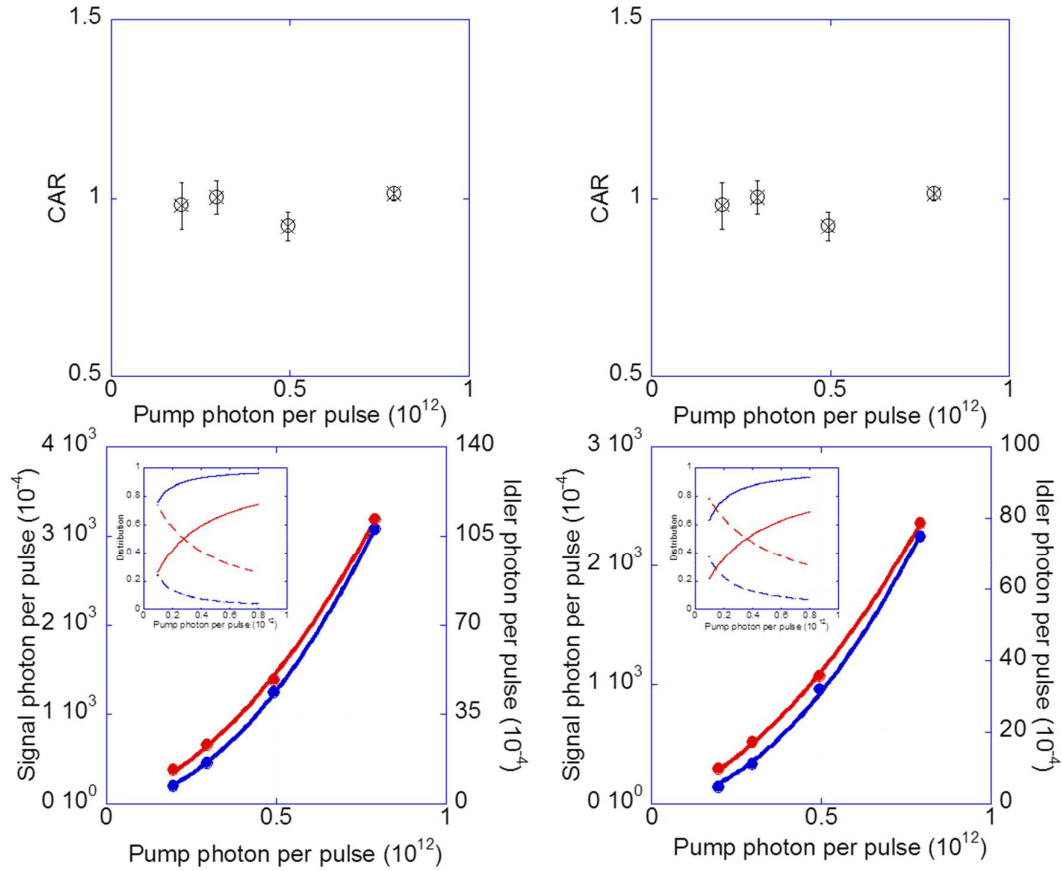
3.3.4.2   DCM in BzOH/EG

Figure 3. 15

a. Coincidence to accidence ratio of DCM in BzOH/EG without PBSs. b. Coincidence to accidence ratio of DCM inBzOH/EG with PBSs. c. Photon detection rate of signal arm (blue) and idler arm (red) without PBSs. d. Photon detection rate of signal arm (blue) and idler arm (red) with PBSs

So far, we have developed a good understanding of the strength of different processes in the EGFP sample. To further analyze the mechanics in the EGFP, we characterize the purity of photon pairs from the other four samples by applying the same CAR measurements with and without using the polarization filtering as comparisons. Here we first investigate the DCM in BzOH/EG since it exhibits the best efficiency in the StFWM process. The CAR of the photon pairs from the DCM in BzOH/EG is shown in Fig. 3.15. We see that although the efficiency of StFWM of DCM in BzOH/EG is the highest among the five, the purity of the photon pairs generated from SpFWM process is very low. At high pump power, the number of single counts in the signal detector is saturated. Therefore, we start recording the data from below 1×10^{12} pump photon per pulse. A CAR of around 1 with (Fig. 3.15a) or without (Fig. 3.15b) using the polarization filtering are shown. Both the coincident and accidental counts per pulse are around 0.003 at 0.8×10^{12} pump photons per pulse. The photon pairs generated via the SpFWM process are buried in the large fluctuation of the accidental photons. Therefore, we cannot have high purity photon pairs from DCM in BzOH/EG using the current setup. To analyze the processes in the sample, we plot Fig. 3.15c and Fig. 3.15d showing the single counts corresponding to the results obtained in Fig. 3.15a and Fig. 3.15b, respectively. The S_2 processes dominate on both arms, especially on the signal arm. And of the two S_2 processes, fluorescence is the dominating one because the CAR provides no evidence for correlated photon pairs generated from the SpFWM process. Then, we insert the polarization filtering to

reduce the fluorescence, but it is still not enough filtering for us to distinguish the photon pairs from the noise photons. We observe that in <u>Fig. 3.15d</u>, $S_2 N_p^2/N_{s(i)}$ is almost invariant with or without using the polarization filtering. This invariance adds further evidence that the SpFWM process is much more weaker comparing to the TPA because the number of correlated photon pairs is negligible when comparing to the fluorescence photons. As a result, the numerator and denominator of $S_2 N_p^2/N_{s(i)}$ will both reduce by half when we insert the polarization filtering, leading to an invariance to the fraction. The reason that we have observed strong fluorescence is that the fluorescence spectrum of DCM in BzOH/EG is centered at 655 nm. It is very close to 730 nm where we collect the signal photons. The large amount of fluorescence will lower the purity of the photon pairs generated from the SpFWM process. In conclusion, the DCM in BzOH/EG does not qualify as a good photon pair source due to its fluorescence spectrum.

3.3.4.3 DCM in ethanol
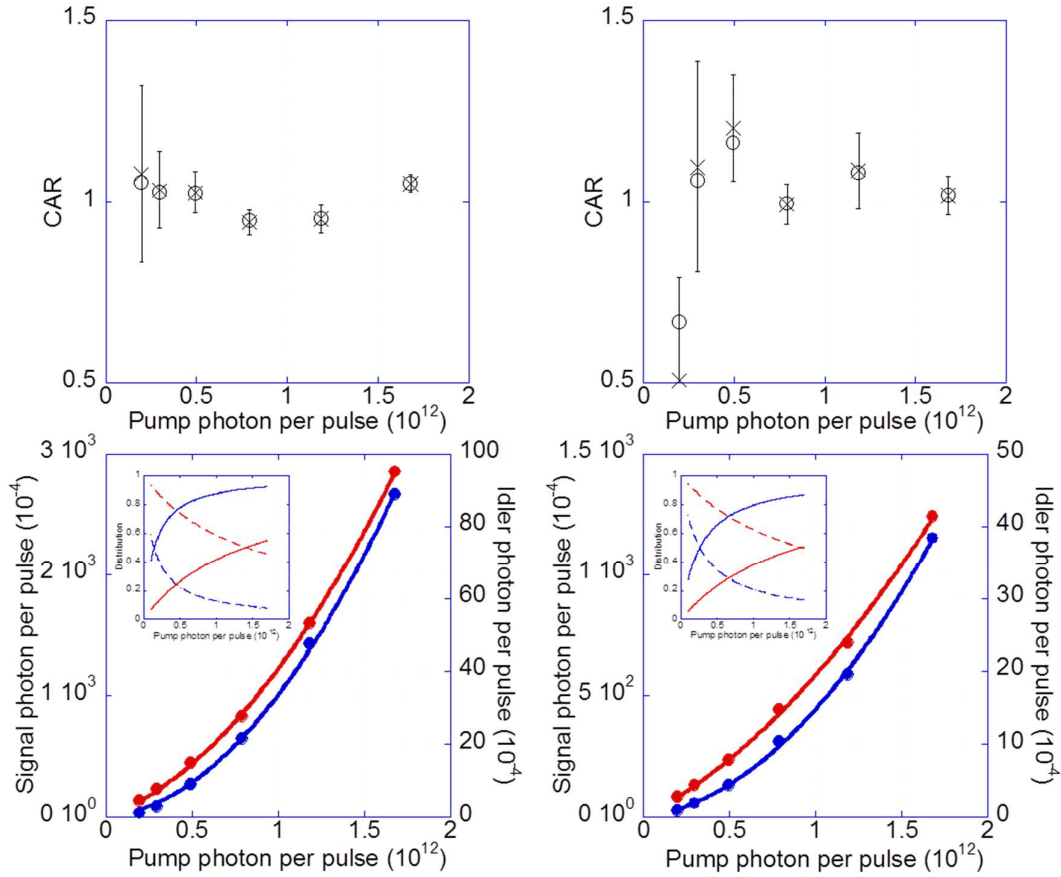
a. Coincidence to accidence ratio of DCM in ethanol without PBSs. b. Coincidence to accidence ratio of DCM in ethanol with PBSs. c. Photon detection rate of signal arm (blue) and idler arm (red) without PBSs. d. Photon detection rate of signal arm (blue) and idler arm (red) with PBSs.

The DCM in ethanol has a fluorescent peak centering at 627 nm [89], which is 100 nm away from signal band. We expect to detect less fluorescence from this sample than the previous one. We use same way to characterize the purity of the photon pairs generated in this sample, the results are shown in Fig. 3.16. Although we observe less photons than the previous example, unfortunately, it's still too much fluorescence. At

high pump power, the signal detector is saturated so that we record data from below 2×10^{12} pump photon per pulse. The coincident and accidental photon pairs per pulse are both around 2×10^{-4} at 0.8×10^{12} pump photon per pulse, which gives a CAR of 1. The result with the polarization filtering is used for comparison as shown in Fig. 3.16b and Fig. 3.16d. Unfortunately, the filtering is not strong enough to reduce the huge fluorescence background. We conclude that although the fluorescence has decreased comparing to DCM in BzOH/EG, the amount is still too large for us to observe any photon pair from spontaneous four-wave mixing.

3.3.4.4 Pyrromethene 546

Figure 3. 17

a. Coincidence to accidence ratio of pyrromethene 546 without PBSs. b. Coincidence to accidence ratio of pyrromethene 546 with PBSs. c. Photon detection rate of signal arm (blue) and idler arm (red) without PBSs. d. Photon detection rate of signal arm (blue) and idler arm (red) with PBSs.

Since the fluorescence is the main obstacle to achieve high purity photon pairs, Pyrromethene 546 and pyrromethene 556 with similar fluorescent spectrum as EGFP are under investigation. For pyrromethene 546, the fluorescence peak is at 505 nm[90], 225 nm away from the signal band. We use the same method to characterize the purity of the photon pairs. The results are shown in Fig. 3.17. A CAR with a

maximum value of 6 without the polarization filtering and 10 with the polarization filtering are obtained. This is better than the DCM samples due to a better fluorescence spectrum, but worse than the EGFP sample either due to less coincidence photons or more accidental photons. Therefore, we compare the coincident photons per pulse for pyrromethene 546 and EGFP. For pyrromethene, the coincident photons per pulse is 1.7×10^{-5} at 3.5×10^{12} pump photon per pulse at the peak CAR. For EGFP, we find that the coincident photons per pulse at the same pump power is 1.5×10^{-5}, which is very close to the value in pyrromethene. So, the reason that we see a higher CAR in EGFP must be less accidental photons. We want to discover the reason behind it. Comparing Fig. 3.14c (EGFP) with Fig. 3.17c (pyrromethene 546), we obtain almost the same single counts in the signal channel for both samples, however, more single counts are detected in the idler arm for pyrromethene 546. Also, $S_2 N_p^2 / N_i$ of pyrromethene 546 in the idler arm is much less than that of the EGFP. This suggest that the Raman photons contribute more in the pyrromethene 546 than in the EGFP. And the invariance of the $S_2 N_p^2 / N_i$ in the idler arm before and after the polarization filtering adds further evidence that the stimulated Raman photons contribute most to the accidental counts because the accidental counts cannot be blocked by the polarization filtering. So, we can safely conclude that EGFP is better than pyrromethene 546 due to less Raman photons.

3.3.4.5   Pyrromethene 556
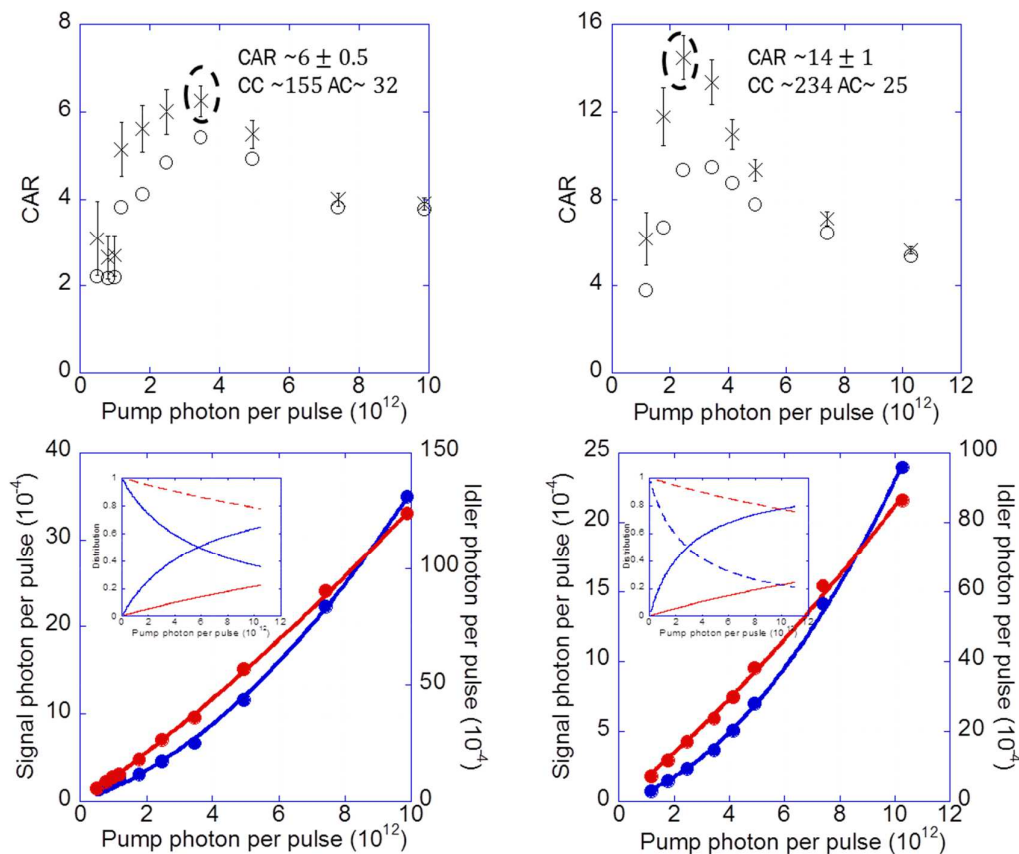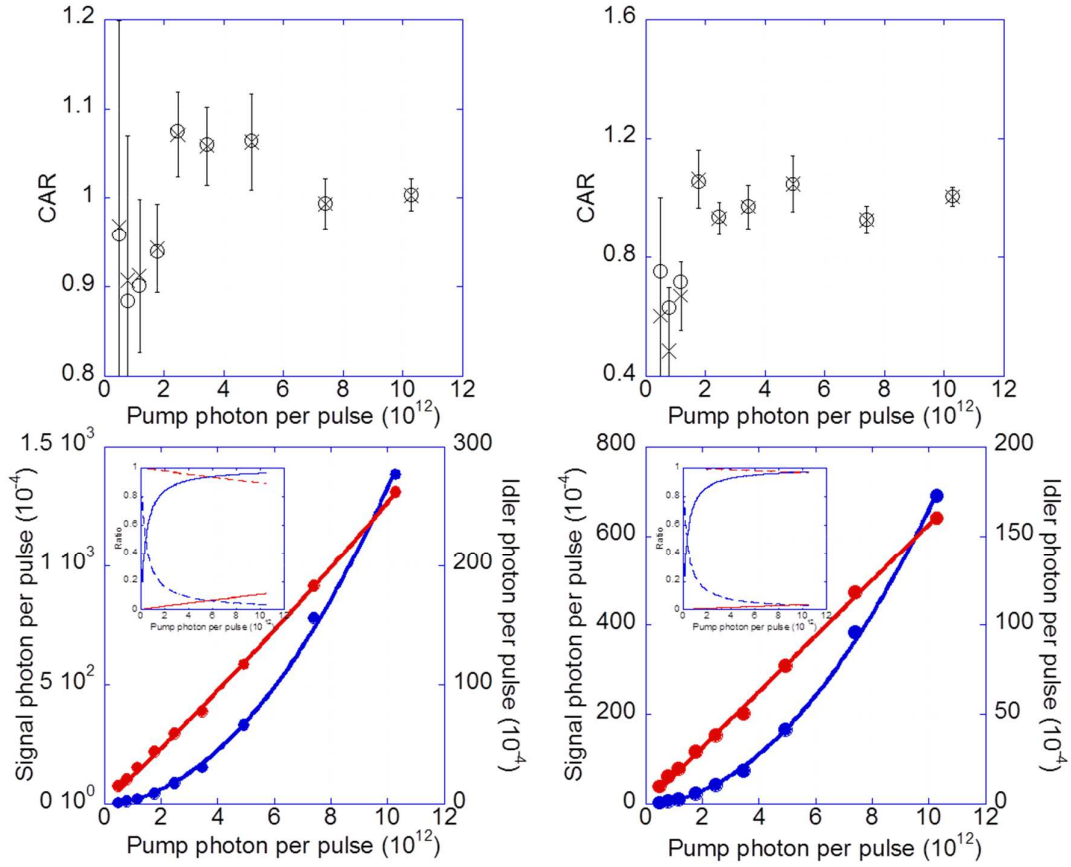
a. Coincidence to accidence ratio of pyrromethene 556 without PBSs. b. Coincidence to accidence ratio of pyrromethene 556 with PBSs. c. Single counts of signal arm (blue) and idler arm (red) without PBSs. d. Single counts of signal arm (blue) and idler arm (red) with PBSs.

Here, we move on to study the last sample. Fig. 3.18 shows the result of the CAR measurement of photon pairs generated in pyrromethene 556. The fluorescence spectrum of pyrromethene 556 is centered at 535 nm[91], which is longer than the EGFP (505 nm), but much shorter than the DCM samples (> 600 nm). However, very much like the DCM samples, we are unable to distinguish the photon pairs from

the accidental as the CAR fluctuates around 1 with/without the polarization filtering. Although the signal detector is not saturated at high pump power as occurred in the experiments with DCM samples, the fluorescence might still be the main reason of the accidental counts. By comparing Fig. 3.14c (EGFP) with Fig. 3.18c (pyrromethene 556), clearly, we see that 30 times more single counts are detected in the signal arm in the pyrromethene 556 than that in the EGFP. The large amount of single counts (contributed by the fluorescence) in the pyrromethene 556 leads to the increment of the accidental counts. Therefore, we see that although the fluorescence emission spectrum of pyrromethene 546 and 556 are close, the minor difference between the two spectra can result in a huge difference in the purity of photon pairs. When comparing the components of the single counts with/without the polarization filtering as shown in Fig. 3.18c and Fig. 3.18d, we see that fluorescence dominates the signal channel and stimulated Raman scattering dominates the idler channel.

3.3.5 Dominant processes in 5 samples

Sample	Maximum CAR	Dominant process (signal)	Dominant process (idler)
DCM in BzOH/EG	1	FL, SE, SRS	FL, SE, SRS
DCM in ethanol	1	FL, SE, SRS	FL, SE, SRS
Pyrromethene 556	1	FL, SE, SpRS	FL, SE, SRS

Pyrromethene 546	15	FWM, SpRS	FWM, SRS
EGFP	145	FWM, SpRS	FWM, SRS

Table 3.1 A summary of the maximum CAR and dominant processes of 5 organic fluorophores.

Here, we summarize the nonlinear processes occurring in each sample as shown in the table. We obtain the maximum CAR values of 145 and 15 for the EGFP and the pyrromethene 546 with the polarization filtering scheme, respectively. At the peak pump power ($\sim 2.5 \times 10^6$ W), we obtain the photon production rate at around 7×10^{-4} per pulse for the signal channel and 1.0×10^{-3} per pulse for the idler channel, respectively. However, we cannot observe distinguishable correlated photon pairs from the other three samples due to the fluorescence and Raman scattering. Of all the organic fluorophores tested, the EGFP sample emits the highest-quality, broadband (20 nm) photon pairs, characterized by the correlation measurement (CAR $\sim$145). This can be attributed to the spectrum of the fluorescence and possibly the unique β-barrel structure, which prevent the fluorophores from molecular aggregation that can lead to fluorescence quenching, collision quenching, and fluorescence polarization between two adjacent fluorescent proteins.

In conclusion, our results indicate that the generation of photon pairs in EGFP occurs in the less noisy environment compared to other fluorophores. The EGFP has proven its superiority as a correlated photon-pair source due to its relatively large $\chi^{(3)}$, green fluorescence that is away from the photon pairs, and the less Raman scatterings

probably due to its unique β-barrel structure. The CAR of 145 obtained in the EGFP

is comparable to the results obtained in fibers [92-96] and on chips.

3.4 Two-photon interference

Polarization-entangled photon pairs are desire for quantum communication

applications. Being able to produce high purity correlated photon pairs, we can try to

configure the source to generate the polarization-entangled photon pairs. In this

section, we will outline an experiment to observe generate the two-photon

polarization-entangled state $|H_s H_i\rangle + e^{i2\phi}|V_s V_i\rangle$ and test the quantumness of the

state via the two-photon interference. We propose two different experimental setups

for the generation of the state by using (i) narrow filters, and (ii) unbalanced

polarization interferometers.

3.4.1   Narrow-filter scheme

The experimental setup for generating two-photon polarization entangled state

$|H_s H_i\rangle + e^{i2\phi}|V_s V_i\rangle$ in the narrow filter scheme is shown in Fig. 3.19, where $|H_s H_i\rangle$

and $|V_s V_i\rangle$ represents horizontal and vertical components, and the ϕ is the pump

phase.
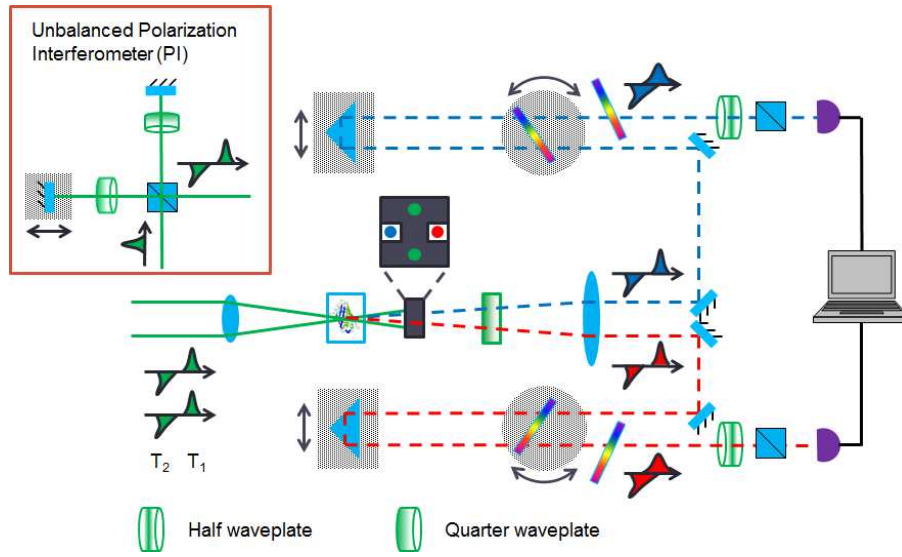
Figure 3. 19

Experimental setup for creating and observing the two-photon interference with narrow-bandwidth filters

We made three changes to the previous experimental setup. First, one of the tunable

bandpass filters is moved from the rotation stage to a fixed position in both the signal

and idler paths to control the passing bandwidths of the photons. Second, both

polarization interferometers in the signal and the idler arms are removed because in

this scheme, we rely on the "stretching" on the temporal shape of the photons to

create the superposition. Last, a half-wave plate and a polarization beam splitter are

introduced in front of the fiber coupler in the signal/idler arm.

A polarization interferometer in the pump path is used to create the horizontally and vertically polarized two-pump beams at two times slots T_1 and T_2, respectively. The Horizontally polarized pump beams generate the $|H_s H_i⟩$ state while the vertically polarized pump beams generate the $|V_s V_i⟩$ state. The generated polarized signal and idler photons are temporally separated with the same time interval as the pump pulses. The combination of the two tunable bandpass filters forms an equivalent bandpass filter with 2 nm bandwidth in the signal and idler. Therefore, the wave packets of the signal and idler are temporally stretched to 1000 fs from their original duration of 200 fs. The "stretching" could help to compensate the time difference between T_1 and T_2 so that the wave packets with different polarizations can be maximumly partially overlapped. Once the wave packets are overlapped, we use the half-wave plates and the polarization beam splitters to control the relative polarization angles of the signal and idler photons and then record the coincidence counts. We obtain the two-photon interference by plotting the coincidences as a function of the relative polarization angles of the signal and idler as shown in Fig. 3.20.
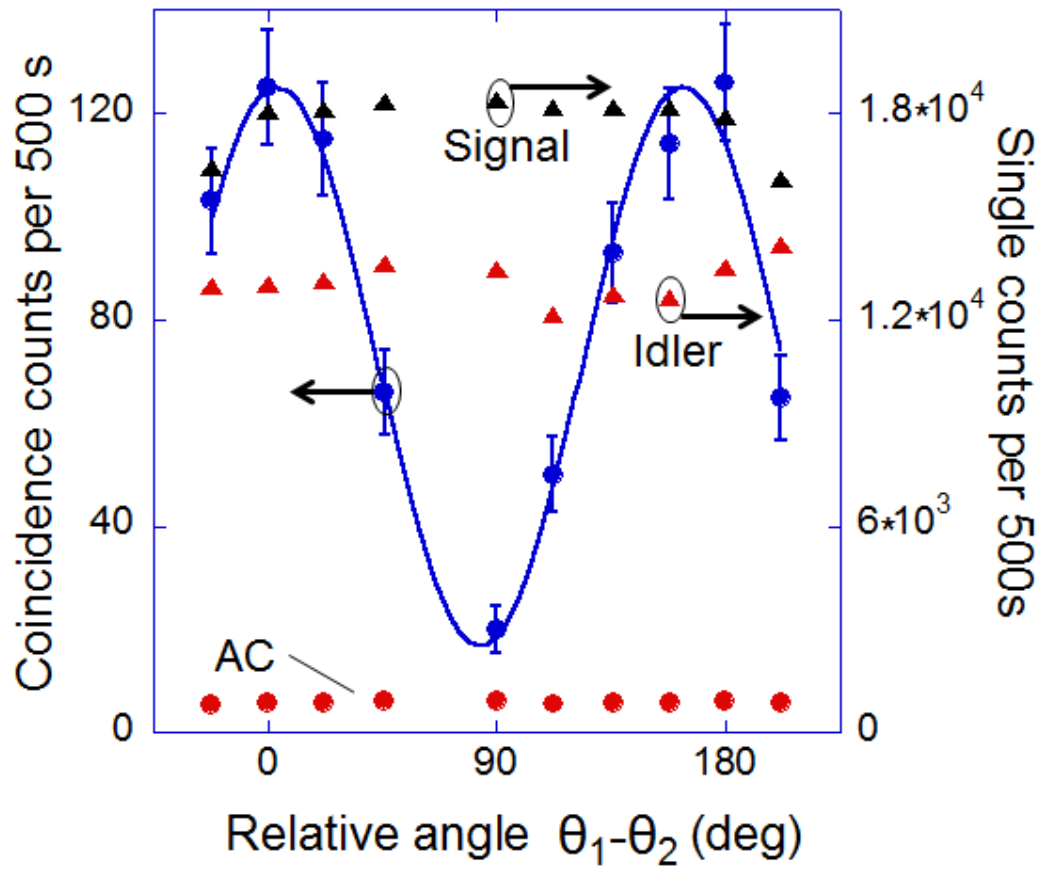
Figure 3. 20

Two-photon interference with the visibility of 76% as a function of relative polarization angle of the signal and idler. The blue dots represent the coincidence counts while the red dots represent the accidental-coincidence counts. The blue curve is the fit for the coincidence counts. The black and red triangles represent the single counts in the signal and idler channels, respectively.

We observe the two-photon interference with a visibility (V) of 76%, which is defined

as $V = \text{TPI visibility} = \frac{CC_{max}-CC_{min}}{CC_{max}+CC_{min}}$, where CC_{max} and CC_{min} represent the

maximum and minimum of the fitting curve for the coincidence counts in Fig. 3.19.

The visibility corresponds to a CAR of ~10, which is much lower than the peak CAR

(43) of the EGFP sample. We can see the imperfection of this experiment; the low

visibility is mainly due to the partial temporal overlapping of the horizontal and vertical polarized wave packets in the signal and idler channels.

3.4.2   Unbalanced polarization interferometer

To improve the visibility of the two-photon interference, we need to solve the above problems. A better way to create the entanglement would be to use the unbalanced polarization interferometer. Therefore, we will build the experimental setup as shown in Fig. 3.21 for perfectly overlapping the horizontally and vertically polarized wave packets of the signal and idler.

Figure 3. 21

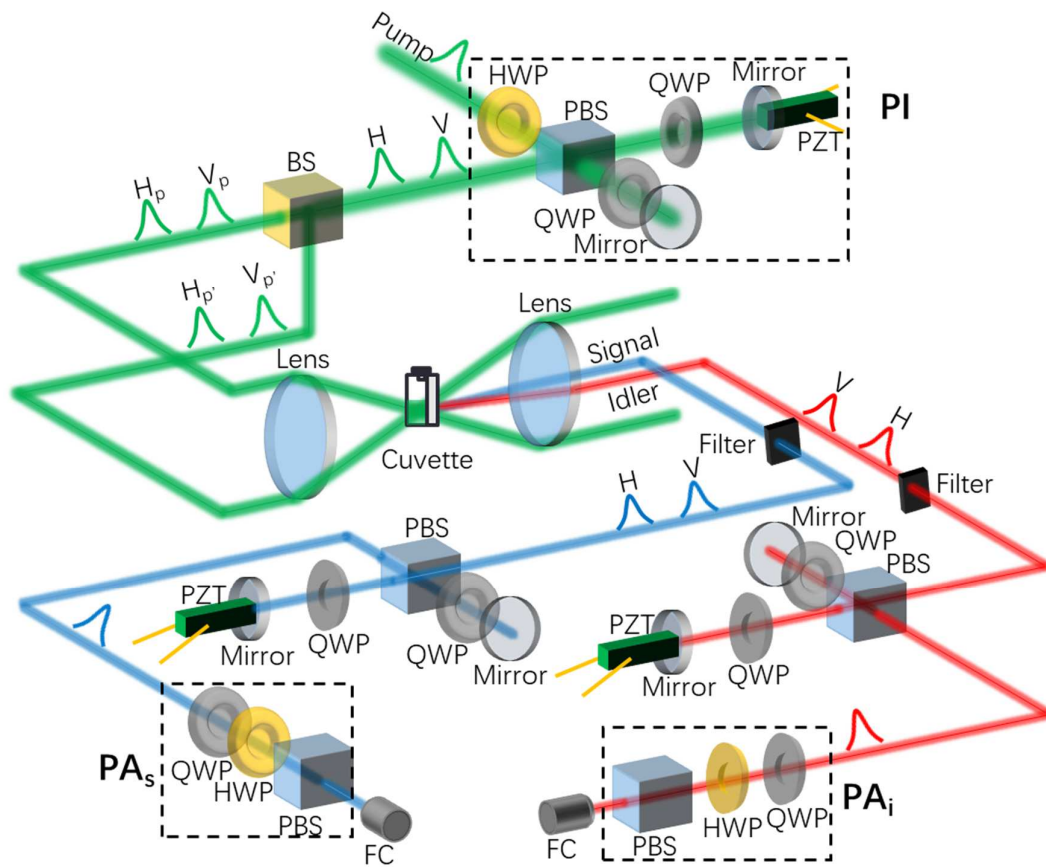The experiment setup for the two-photon interference by using unbalanced polarization interferometers in the signal and idler channels. Polarization analyzers (PA$_s$ and PA$_i$) are introduced to manipulate the state for detection.

In this setup, since the narrow filter is not required, we return the tunable bandpass filters back on the rotation stages. In addition, we insert the polarization interferometers right after the tunable bandpass filter sets. These two polarization interferometers will compensate the time difference (T_1 and T_2) of the two wave packets in the signal and idler, respectively. Although this scheme in theory could perfectly superpose the two states, however, we will be facing two new experimental challenges. First, we need to ensure the stability of the newly introduced interferometers. Second, it is challenging for spatially overlapping the two generated wave packets in the transverse plane. We will address the two challenges one by one.

To study the stability of the interferometer, we can monitor the stability of the interference pattern created by it. Since the power of the generated photons are on the single-photon level, we use the pump beams for generating the interference pattern. In details, we split the pump beam into two additional parts. One part is guided to the path of the generated signal, the other part is guided to the idler, i.e. the dashed blue and red lines in Fig. 3.21. After they go through the polarization interferometers, the beams are then coupled to the fiber couplers, which is connected to a power meter. We attach a PZT in one arm of the polarization interferometer for changing the path difference of the polarization interferometer. We observe a clear interference pattern by applying the voltage to the PZT. The interference patterns are plotted as a function

of the PZT voltage as shown in . The data points are recorded every 2 minutes. We fit the obtained data with a sinusoidal function. The good fitting curves indicate that both interferometers are stable in about 20 minutes.
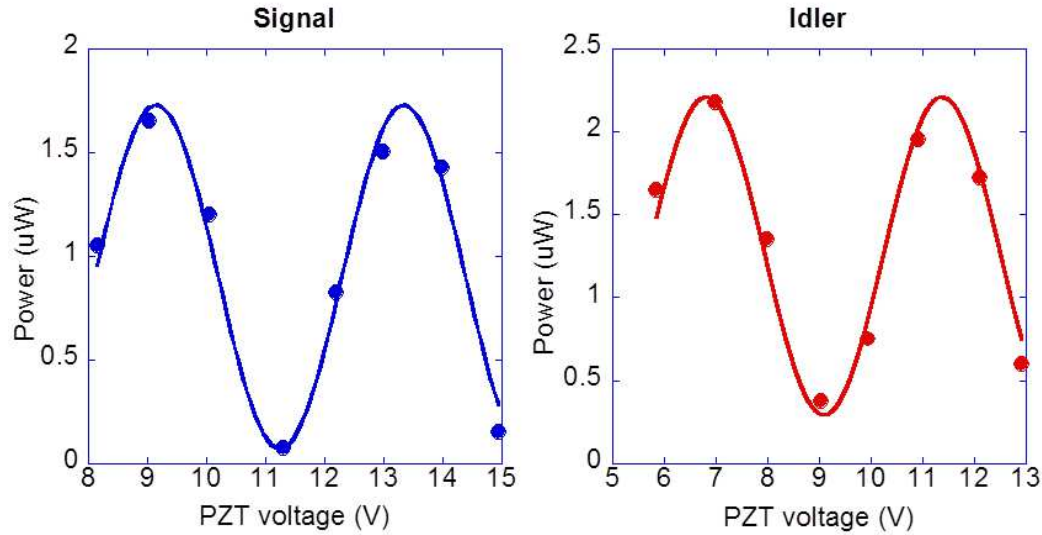
Figure 3. 22

Classical single beam interference with respect to the PZT voltage

To adjust the temporal and spatial alignment of the polarization interferometer, we perform the single photon interference with the scattered pump photons. In this experiment, the signal beam and one of the pump beams are blocked, so that only one pump beam can pass through the sample. In this case, the spontaneous four-wave mixing processes or two-photon absorption won't happen. Also, we remove the notch filter and tunable bandpass filters as we are detecting the pump beam. Since the power of the scattered pump photons are too strong, we insert the neutral density filters for attenuating the pump power. Then, we use the single photon detector for measuring

the attenuated scattered pump photons and look for the single-photon interference by adjusting the voltage of the PZT. We observe the interference pattern as shown in Fig. 3.22, indicating that the two cross-polarized wave packets in the polarization interferometers are overlapped.
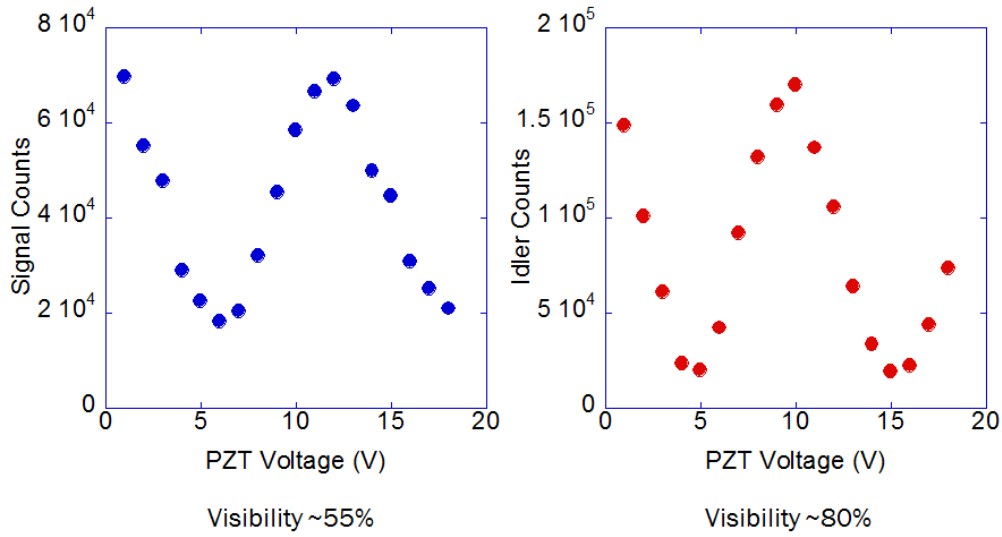
Figure 3. 23

Single photon interference with pump scatterings

The visibility of the single-photon interference for the signal (idler) is about 55% (80 %). With the low visibilities, especially on the signal arm, we are not able to achieve a two-photon interference with visibility better than 76% as obtained in the narrow-filter scheme. However, the polarization interferometer scheme has the potential to achieve a better visibility than 76% if we can improve the alignment, which is the afore mentioned second challenge for us. We can optimize the the temporal alignment by using the PZT during the photon-pair generation process based

on the interference pattern. Therefore, the challenge is to optimize the spatial alignment, which we cannot easily optimize during the experiment.

The most important procedure in the spatial alignment is to improve the overlapping of the pump beams with different polarizations since the phase-matching condition will automatically align the generated signal and idler beams afterward. We use a design as shown in Fig. 3.24 for ensuring the overlapping of the horizontally and vertically polarized pump beams.
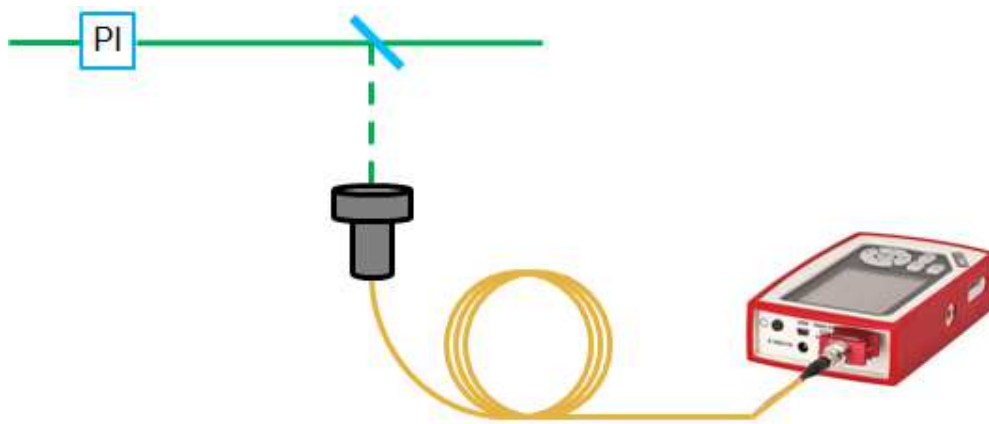
Figure 3. 24

Alignment assistance with single mode fiber.

Before the pump is split to three beams (two pump beams and one probe beam), we insert a glass slide right after the polarization interferometer. The glass slide reflects a small portion of pump beam into a 785 nm single mode fiber. The coupling efficiencies of the horizontally and vertically polarized beams will indicate how close they are spatially overlapped. Therefore, by optimizing the coupling efficiencies of both polarizations, we can align the spatial overlapping of the horizontally and

vertically polarized beams. Using the methods mentioned above, we have optimized the interferometric visibility of polarization interferometers in the signal and idler arms (both are around 99%). This will set an upper limit on the measurable two-photon-interference visibility of 98% in our experiment.
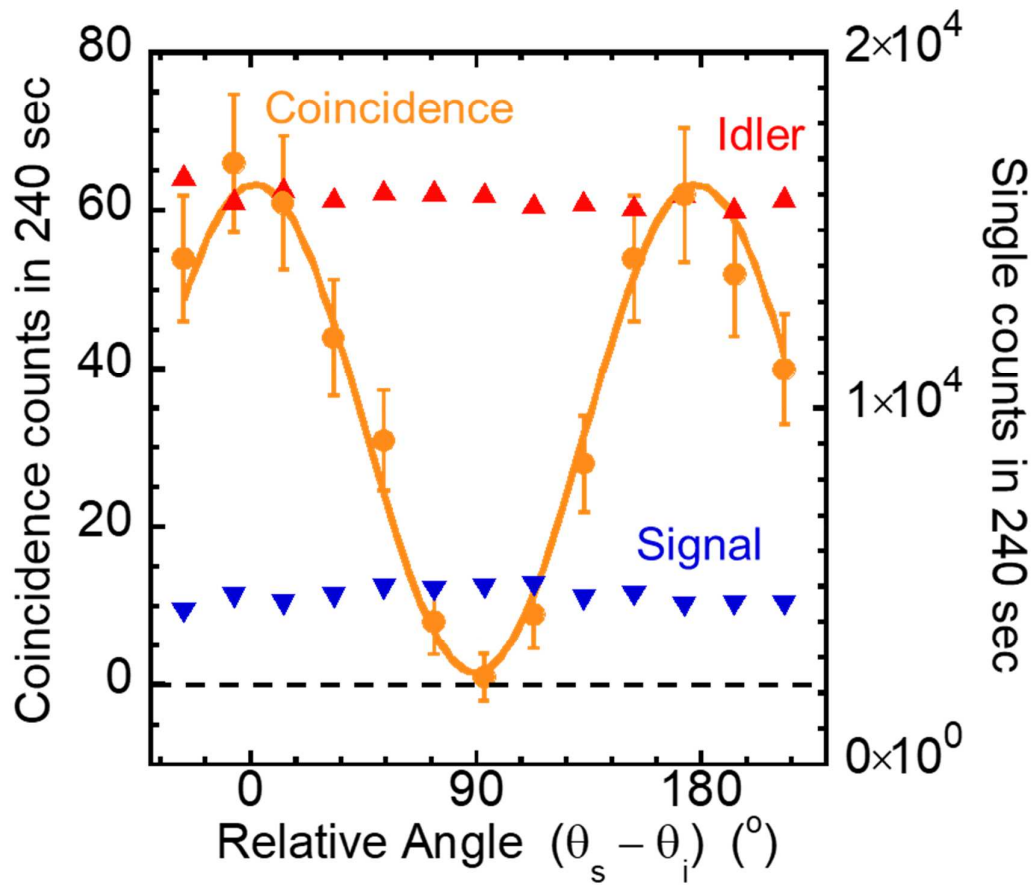

Figure 3. 25

Two-photon interference with the visibility of 98% as a function of the relative polarization angle between the signal and idler. The orange dots represent the coincidence counts with the subtraction of accidental-coincidence counts. The solid orange curve is the fit for the orange dots. The blue and red

triangles represent the single counts in the signal and idler channels. The error bars are calculated based on the standard deviation of photon counts using Poisson statistics.

We measure the two-photon interference pattern with respect to the relative polarization angle between the polarization analyzers on the signal (θ_s) and idler (θ_i) arms as shown in Fig. 3.25. The obtained interference pattern is a sinusoidal curve of the coincidence counts vs. the difference between the polarization angles ($\theta_s - \theta_i$). With an integration time of 4 min for each data point, where the pump phase (ϕ_p) is kept fixed, we obtain a fringe visibility of 98% (85%) with (without) the subtraction of the accidental coincidence counts, which agrees with the upper limit of the two-photon-interference visibility of 98%, much better than the visibility in the narrow-filter scheme (76%). This means that our alignment is very well optimized. Therefore, the probability amplitudes of $|H_s H_i\rangle$ and $|V_s V_i\rangle$ are subject to the dynamic decoherence environment inside the EGFP because the photon pairs are generated in an ensemble of excited fluorophores at two different time slots.

3.5 Quantum state tomography

To fully characterize the Bell state $(|H_s H_i\rangle + e^{i\phi_p}|V_s V_i\rangle)/\sqrt{2}$ where we set $\phi_p = 0$, we employ the standard method of quantum state tomography. We record the coincidence counts with 16 measurement settings in different basis by adjusting the polarization analyzers in the signal and idler arms. Each measurement will project the quantum state to a basis that will reveal a distinct aspect of the quantum state's reality.

For each setting, we collect the coincidence counts and accidental counts with an integration time of 2 minutes.
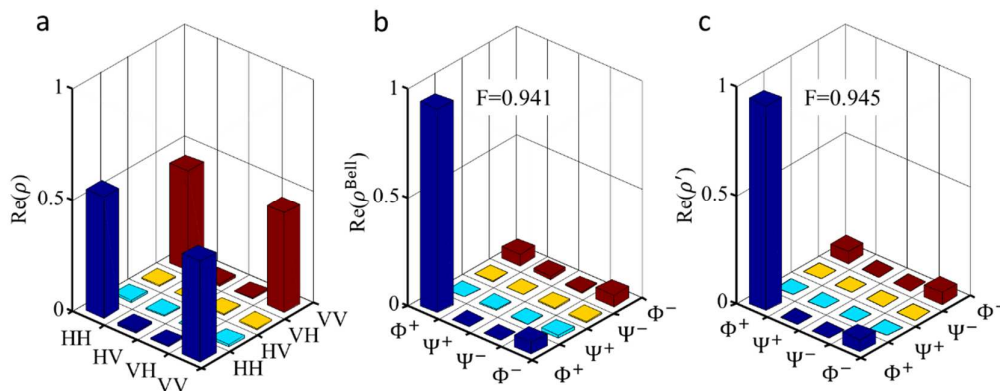
Figure 3. 26

Measured density matrix of the entangled photonic state. (a) The reconstructed state in the horizontal-vertical basis. (b) The reconstructed state in the Bell-state basis. (c) The estimated state in the Bell-state basis. Measured density matrix of the entangled photonic state.

We then use the maximum-likelihood estimation algorithm to reconstruct the 4×4 density matrix (ρ) of our state. The obtained density matrix has a fidelity (F = $\sqrt{\langle \phi^+ | \rho | \phi^+ \rangle}$) of 0.94 ± 0.05 in the horizontal–vertical (HV) basis as shown in Fig. 3.26a. With the help of the measured density matrix, we can understand many aspects of the experiment, including both the quality of the experimental setup and the effects of decoherence inside the EGFP. For example, the small imaginary components indicate that the polarization interferometers are stable; within the duration of the experiment (~30 min), they introduce little phase drift between the $|H_s H_i\rangle$ and $|V_s V_i\rangle$ amplitudes. The four distinct peaks with a relation of $\rho_{\mathrm{HHHH}} > \rho_{\mathrm{HHVV}} = \rho_{\mathrm{VVHH}} \approx \rho_{\mathrm{VVVV}}$ suggests that we generate a mixture of the target Bell state and the

unwanted $|H_sH_i\rangle$ state. It's clearer to view the matrix on the Bell-state basis (ρ^{Bell}) as shown in [Fig. 3.26b](#), where $\rho^{\text{Bell}}_{\phi^+\phi^+} = 0.941$ is the dominating component and $\rho^{\text{Bell}}_{\phi^+\phi^-} = \rho^{\text{Bell}}_{\phi^-\phi^+} = \rho^{\text{Bell}}_{\phi^-\phi^-} \approx 0.052$. If we neglect the other much smaller components in the non-corner locations, we can approximate the density matrix as $\rho'(p) = p|\phi^+\rangle\langle\phi^+| + (1-p)|H_sH_i\rangle\langle H_sH_i|$, which is a mixed state. We fit the measured density matrix with a probability $p = 0.89$ using the approximation, where the corresponding fidelity of $\rho'(0.89)$ is 0.945, close to the fidelity of the measured density matrix (0.941). We plot the approximated state as shown in [Fig. 3.26c](#) in comparison with the original measured state. In addition to this measurement, we perform another two quantum state tomography measurements with integration times of 4 and 6 min (for each setting) to reduce the fluctuations in the coincidence counts. They also result in similar mixed states. The decoherence effect in our experiment is the mixture of the Bell state and the $|H_sH_i\rangle$ state, which may be unavoidable in the current experimental setup.

The above result is achieved by studying the experimental scenario as shown in [Fig 3.27](#), where the horizontally-polarized pump pulse leads the vertically-polarized pump pulse by 1 ps. The quantum superposition and coherence within the ensemble of excited fluorophores at the two time slots lasts approximately 1ps [109], therefore, we expect to see some decoherence characterized by p_2 and p_3.
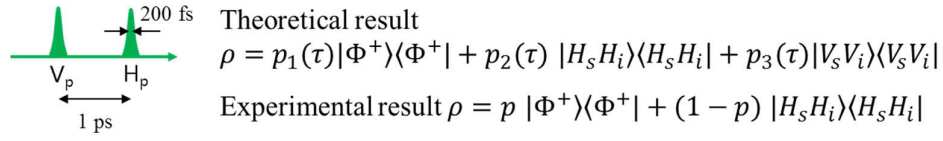
Figure 3. 27

The theoretical and experimental results of the photonic state in our experimental scenario. The horizontally-polarized pump pulse (FWHM ~200fs) leads the vertically-polarized pump pulse (FWHM ~200fs) by 1 ps.

In fact, the future experiments could be designed to change the temporal delay between the pump pulses to gather more information about the quantum coherence and superposition within the ensemble of fluorophores as shown in Fig. 3.28.

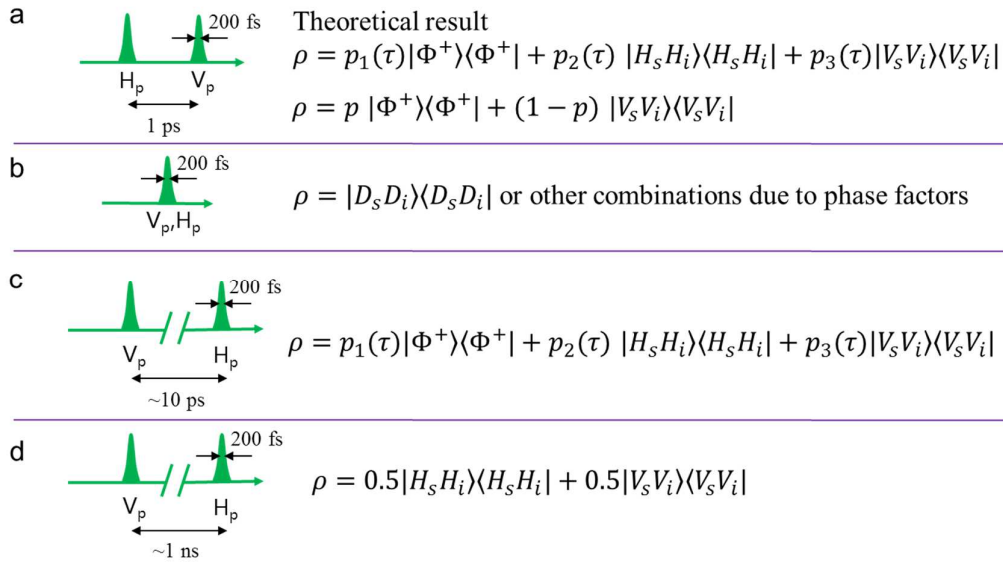**Figure 3. 28**

The predicted results of the photonic state in our experimental scenario. a. the vertically-polarized pump pulse (FWHM ~200fs) leads the horizontally-polarized pump pulse (FWHM ~200fs) by 1 ps. b. the vertically-polarized pump pulse (FWHM ~200fs) and the horizontally-polarized pump pulse (FWHM ~200fs) overlaps. c. the horizontally-polarized pump pulse (FWHM ~200fs) leads

the vertically-polarized pump pulse (FWHM ~200fs) by 10 ps. d. the horizontally-polarized pump pulse (FWHM ~200fs) leads the vertically-polarized pump pulse (FWHM ~200fs) by 1 ns.

The predicted results are based on the current understanding of the lifetime of quantum superposition and coherence within the system. In Fig. 3.28a, an additional $|V_sV_i\rangle\langle V_sV_i|$ component is expected to appear as opposed to the case in Fig. 3.27 where we have measured an additional $|H_sH_i\rangle\langle H_sH_i|$ component. In Fig. 3.28b, obviously, the generated state would be a pure state because of the overlap. In Fig. 3.29c, p_2 and p_3 are expected to increase with an increasing τ. In Fig. 3.29d, the entanglement will disappear because of the delay is much longer than the lifetime of the quantum coherence within the system, therefore, $p_2 = p_3 = 0.5$. Note that the above assumptions need to be tested by designing the experiments accordingly.

3.6 Quantumness of the state

To explore the origin of this decoherence effect, we want to study the quantumness of the state. In a decohering environment, we can use the degree of entanglement and the degree of purity as crucial criteria for realizing the quantum information protocols of a quantum system. We use the entanglement of formation (En) [97] for quantifying the degree of entanglement and the linear entropy (SL) [98] for quantifying the degree of purity of our two-photon polarization-entangled system. According to the previous chapter, the analytical expression for E_n is given as:

$$E_n = H\left(\frac{1 + \sqrt{1 - \gamma^2}}{2}\right),$$
(3.2)

where the function $H(x) = -x \log_2 x - (1-x) \log_2(1-x)$. The concurrence $\gamma = \max\{0, \lambda_1 - \lambda_2 - \lambda_3 - \lambda_4\}$, where the λ_is are the square roots of the eigenvalues of the matrix $\rho(\sigma_y \times \sigma_y)\rho^*(\sigma_y \times \sigma_y)$, in a decreasing order. σ_y is the second Pauli matrix, and ρ^* is the complex conjugate of ρ. For the approximated matrix ρ', $\gamma = 1 - 2p$.

The analytical expression for S_L is given as:

$$S_L = \frac{4(1 - \mathrm{tr}(\rho))^2}{3}. \tag{3.3}$$

For the approximated matrix, $S_L = 8p(1-p)/3$.

The entanglement of formation (E_n) and the linear entropy (S_L) forms a characteristic plane for the two-qubit states. We place the measured state ρ and the approximated state ρ' on the plane as shown in Fig. 3.26a. On the plane, the grey region represents the physically impossible combinations of E_n and S_L. Therefore, the maximally entangled mixed states [97], which exhibit the maximized entanglement for a given linear entropy, lie on the boundary between the white and gray regions. Some states are worth to mention. For example, a pure unentangled state lies at (0, 0); a pure maximally entangled state lies at (0, 1); a maximally mixed and unentangled state lies at (1, 0). In our study, $\rho'(p)$ (red solid curve) varies along the curve from the pure maximally entangled state (0, 1) to the pure unentangled state (0, 0) as p decreases

from 1 to 0. Our experimentally generated state (black circle) lies on the red curve

at (0.14, 0.83).
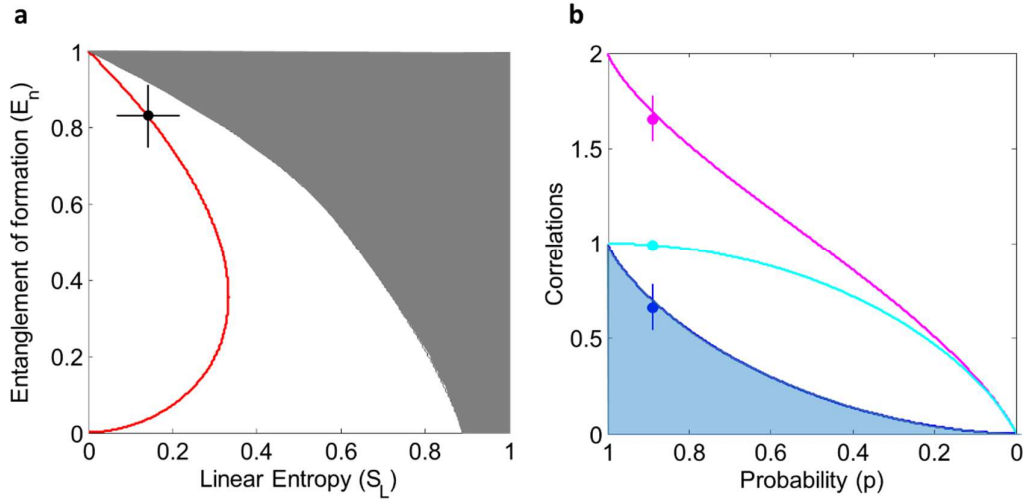
Entanglement of formation, linear entropy, and correlations of the state. (a) Entanglement of formation (E_n) vs. linear entropy (S_L). The solid circle represents the experimentally generated entangled photonic state. The solid red curve represents the behavior of $\rho'(p)$ on the plane. The gray region represents the physically impossible combinations of E_n and S_L. (b) The total correlation, classical correlation, and quantum correlation vs. probability p. The solid magenta, cyan, and blue circles represent total correlation (I), classical correlation (C), and quantum correlation (Q) of the experimentally generated entangled photonic state. The solid magenta, cyan, and blue curves represent the theoretical behaviors of I, C, and Q as functions of $\rho'(p)$. The curved edge of the light blue region represents the relative entropy (R_n) of $\rho'(p)$. The error bars are calculated based on the standard deviation of photon counts using Poisson statistics.

Since some quantum tasks may not rely on the entanglement but still exploit quantum

advantages [99, 100] due to the non-entanglement quantum correlation, it is important

to first distinguish the quantum correlation from the total correlation, then extract the

non-entanglement quantum correlation within the quantum system, especially in a

decoherence environment. Here we demonstrate the characterization of the

correlations within our quantum system. Based on the study of the bipartite system in the previous chapter, we know the quantum mutual information ($I(\rho_{A:B}) \equiv S(\rho_A) + S(\rho_B) - S(\rho_{AB})$) [101] measures the total correlation between the two subsystems, the classical correlation ($C(\rho_{AB}) = \max_{B_i^\dagger B_i}[S(\rho_A) - \sum_i p_i S(\rho_A^i)]$) characterizes the classically achievable correlation, and the quantum correlation ($Q = I - C$) quantifies the correlation that cannot exist in any classical state. For the approximated density matrix $\rho'(p)$,

$$I = -p \log_2\left(\frac{p}{2}\right) - (2-p)\log_2\left(1 - \frac{p}{2}\right) + x_1 \log_2 x_1 + x_2 \log_2 x_2, \qquad (3.4)$$

$$C = -\frac{p}{2}\log_2\left(\frac{p}{2}\right) - \left(1 - \frac{p}{2}\right)\log_2\left(1 - \frac{p}{2}\right), \qquad (3.5)$$

$$Q = -\frac{p}{2}\log_2\left(\frac{p}{2}\right) - \left(1 - \frac{p}{2}\right)\log_2\left(1 - \frac{p}{2}\right) + x_1 \log_2 x_1 + x_2 \log_2 x_2, \qquad (3.6)$$

where $x_{1,2} = 0.5 \pm 0.5\sqrt{p^2 + (1-p)^2}$.

We show the correlations (I, C, Q) for our generated state and for the approximated state in Fig. 3.26b. For the approximated state (solid curves), I, C, and Q, all decay monotonically to 0 at $p = 0$ where the state becomes $\rho'(0) = |H_s H_i\rangle\langle H_s H_i|$ when it carries no information. The I and Q of our generated state (solid circles) are slightly off the curves because we have neglected the small non-corner components in the measured density matrix.

To quantify the difference between the quantum entanglement and the quantum correlation, we can rely on the relative entropy of entanglement (R_n) [102], which

measures the distance between the non-entanglement quantum correlation and quantum correlation. For $\rho'(p)$,

$$R_n = -\frac{p}{2}\log_2\left(\frac{p}{2}\right) - \left(1-\frac{p}{2}\right)\log_2\left(1-\frac{p}{2}\right) + x_1\log_2 x_1 + x_2\log_2 x_2, \qquad (3.7)$$

In Fig. 3.25b, we can see that the relative entropy of $\rho'(p)$ (the curved edge of the light blue region) overlaps with the quantum correlation. It means that the entanglement is the only contributing factor to the quantum correlation in $\rho'(p)$. Therefore, we conclude that the decoherence effect in EGFP can induce an additional component $|H_sH_i\rangle\langle H_sH_i|$ in the prepared state, which can reduce the classical correlation, the quantum correlation, and the total correlation. To understand the origin of the decoherence effect, we can investigate the nonlinear optical processes occurring inside the EGFP. In our case, the dominating process is TPA [88]. The probability that a fluorophore undergoes TPA is ~0.1 within one pump-pulse duration. This means that in the experiment, while the horizontally and vertically polarized pump pulses can create the polarized photon pairs in an ensemble of EGFP molecules through the SpFWM process, simultaneously the pulses can also excite some molecules to the first excited state S_1 via TPA with a probability of ~0.1. Note that the temporal delay of the pump pulses ($\Delta t = 33.3$ ps) is two orders of magnitudes less than the lifetime of S_1 (~3 ns). Therefore, the probability of TPA can make a big difference to the purity of the generated state because when the vertically polarized pump pulses enter the sample, ~10% of the molecules (which

are excited by TPA) are in the excited state and hence cannot participate in the generation of photon pairs through SpFWM. What's more, the molecules that contribute to the SpFWM with the horizontally polarized pump pulses may undergo TPA with the vertically polarized pump pulses. These molecules become unable to produce the quantum amplitude for the vertically polarized photon pairs. Therefore, the net outcome is the occurring of an additional component $|H_s H_i\rangle\langle H_s H_i|$ in the prepared two-photon state. This effect certainly reduces the entanglement and the quantum correlation of the generated photon pairs.

Since the entangled photon pair is better preserved than the correlated photon pair in multiple scattering media [103], our entangled photon pairs can be used as a heralded single-photon source for biomedical imaging. In addition, the TPI visibility of ~85% (~98%) for the entangled photon pairs can provide signal-to-noise ratio as high as 10 dB (20 dB) for sensing and imaging through the coincidence basis. Therefore, we can use the CCs of the photon pairs for observing spatiotemporal dynamics of proteins with resolution surpassing the diffraction limit [56, 104]. The spectral [105] and spatial properties [106] of the polarization-entangled photon pairs can also be used for performing bi-photon spectroscopy [107] and coincidence imaging (ghost imaging) [108] such as measuring the spectral and spatial properties of the EGFP-expressing cells [8] via coincidence basis measurements, respectively. For example, we can design the wavelength range for the signal and idler such that the signal photons travel through the cells under study experiencing phase change and loss while the idler

photons travel through the cells without disturbance. The signal photons are detected by using a single-photon detector. As for the idler photons, we insert a tunable filter or a lens before a single-photon detector for performing the local spectral or spatial analysis, respectively. We can then extract out the spectral and spatial properties of the cells under study via coincidence basis measurements. We can choose the polarization projection angles of the signal and idler photons to be 45° for the Bell state $|\phi^+\rangle$ as we perform the coincidence imaging or bi-photon spectroscopy. The cells under study can be like the transfected mammalian cells (293ETN cells derived from the human embryonic kidney cell line HEK293) with a plasmid encoding for EGFP [8]. Moreover, the entangled photon pairs can be engineered for manipulating the vibronic states in FPs through two-photon excitation. Their superiority originates from the simultaneous absorption of the entangled photons [56], thus avoiding the decay process in the intermediate states that occur when using classical light.

Even more intriguing, however, is the possibility of developing an experimental heuristic for quantum effects in EGFP. Since EGFP can be expressed in living cells, the genetic sequences encoding the residues that define their structures and physical characteristics can be altered. There is a major advantage to using a biological system for generating the fluorophores of interest: physical characteristics can be rapidly and efficiently optimized via random mutagenesis [30], and thus enabling a process by which entanglement sources can be genetically engineered. For this reason, our FP-based entangled photon source is bio-compatible and comparable to quantum dots

as fluorescent labels in medical applications. In addition, our photonic entanglement generation scheme in EGFP can be easily extended to high dimensions ($d > 2$) such as for generating a time-bin polarization-entangled state. Also, the observed fidelity and quantum correlation of the entangled photon pairs generated in EGFP encourage us to apply the quantum illumination technique44 in EGFP-expressing cells in the future.

In conclusion, we have generated polarization-entangled two-photon states with high fidelity through the SFWM process in EGFP. The measured density matrix unveils the fidelity-limiting decoherence effect that originates from TPA inside the EGFP. Moreover, our prepared state is free from environmental decoherence because of the protective β-barrel structure that encapsulates the fluorophore in the protein. Our photonic entanglement generation and characterization indicate that the SFWM process in EGFP is a promising quantum process for developing quantum spectroscopic techniques and quantum-enhanced measurements in biological materials.

References

1.	Engel, G.S., et al., *Evidence for wavelike energy transfer through quantum coherence in photosynthetic systems.* Nature, 2007. **446**(7137): p. 782-786.

2.	Sarovar, M., et al., *Quantum entanglement in photosynthetic light-harvesting complexes.* Nature Physics, 2010. **6**(6): p. 462-467.

3.	Maeda, K., et al., *Chemical compass model of avian magnetoreception.* Nature, 2008. **453**(7193): p. 387.

4.	Li, X., et al., *Optical-fiber source of polarization-entangled photons in the 1550 nm telecom band.* Physical review letters, 2005. **94**(5): p. 053601.

5.	Sharping, J.E., et al., *Generation of correlated photons in nanoscale silicon waveguides.* Optics express, 2006. **14**(25): p. 12388-12393.

6.	Shimomura, O., F.H. Johnson, and Y. Saiga, *Extraction, purification and properties of aequorin, a bioluminescent protein from the luminous hydromedusan, Aequorea.* Journal of cellular and comparative physiology, 1962. **59**(3): p. 223-239.

7.	Fan, X. and S.-H. Yun, *The potential of optofluidic biolasers.* Nature methods, 2014. **11**(2): p. 141-147.

8.	Gather, M.C. and S.H. Yun, *Single-cell biological lasers.* Nature Photonics, 2011. **5**(7): p. 406-410.

9.	!!! INVALID CITATION !!! [4-7].

10.	Lippincott-Schwartz, J. and G.H. Patterson, *Development and use of fluorescent protein markers in living cells.* Science, 2003. **300**(5616): p. 87-91.

11.	Schwille, P., et al., *Molecular dynamics in living cells observed by fluorescence correlation spectroscopy with one-and two-photon excitation.* Biophysical journal, 1999. **77**(4): p. 2251-2265.

12.	Dayan, B., et al., *Two photon absorption and coherent control with broadband down-converted light.* Physical review letters, 2004. **93**(2): p. 023005.

13.	Xiang, G.-Y., et al., *Entanglement-enhanced measurement of a completely unknown optical phase.* Nature Photonics, 2011. **5**(1): p. 43.

14.	Schrödinger, E., *What is life?: With mind and matter and autobiographical sketches*. 1992: Cambridge University Press.

15.	Joaquim, L., O. Freire, and C.N. El-Hani, *Quantum explorers: Bohr, Jordan, and Delbrück venturing into biology.* Physics in Perspective, 2015. **17**(3): p. 236-250.

16.	Löwdin, P.-O., *Quantum genetics and the aperiodic solid: Some aspects on the biological problems of heredity, mutations, aging, and tumors in view of the quantum theory of the DNA molecule*, in *Advances in quantum chemistry*. 1966, Elsevier. p. 213-360.

17.	Kassal, I., J. Yuen-Zhou, and S. Rahimi-Keshari, *Does coherence enhance transport in photosynthesis?* The journal of physical chemistry letters, 2013. **4**(3): p. 362-367.

18.	Lambert, N., et al., *Quantum biology.* Nature Physics, 2013. **9**(1): p. 10.

19.	Imamoglu, A. and K.B. Whaley, *Photoactivated biological processes as quantum measurements.* Physical Review E, 2015. **91**(2): p. 022714.

20.   Raimond, J.-M., M. Brune, and S. Haroche, *Manipulating quantum entanglement with atoms and photons in a cavity.* Reviews of Modern Physics, 2001. **73**(3): p. 565.

21.   Peyronel, T., et al., *Quantum nonlinear optics with single photons enabled by strongly interacting atoms.* Nature, 2012. **488**(7409): p. 57.

22.   Dorfman, K.E., F. Schlawin, and S. Mukamel, *Nonlinear optical signals and spectroscopy with quantum light.* Reviews of Modern Physics, 2016. **88**(4): p. 045008.

23.   Walmsley, I., *Quantum optics: Science and technology in a new light.* Science, 2015. **348**(6234): p. 525-530.

24.   Tsien, R.Y., *The green fluorescent protein.* Annual review of biochemistry, 1998. **67**(1): p. 509-544.

25.   Prasher, D.C., et al., *Primary structure of the Aequorea victoria green-fluorescent protein.* Gene, 1992. **111**(2): p. 229-233.

26.   Chalfie, M., et al., *Green fluorescent protein as a marker for gene expression.* Science, 1994. **263**(5148): p. 802-805.

27.   !!! INVALID CITATION !!! [5, 13-15].

28.   Zimmer, M., *Green fluorescent protein (GFP): applications, structure, and related photophysical behavior.* Chemical reviews, 2002. **102**(3): p. 759-782.

29.   Rizzo, M.A., et al., *An improved cyan fluorescent protein variant useful for FRET.* Nature biotechnology, 2004. **22**(4): p. 445-449.

30.   Nguyen, A.W. and P.S. Daugherty, *Evolutionary optimization of fluorescent proteins for intracellular FRET.* Nature biotechnology, 2005. **23**(3): p. 355-360.

31.   Hakkila, K., et al., *Reporter genes lucFF, luxCDABE, gfp, and dsred have different characteristics in whole-cell bacterial sensors.* Analytical biochemistry, 2002. **301**(2): p. 235-242.

32.   Rudin, M. and R. Weissleder, *Molecular imaging in drug discovery and development.* Nature reviews drug discovery, 2003. **2**(2): p. 123-131.

33.   Denk, W. and K. Svoboda, *Photon upmanship: why multiphoton imaging is more than a gimmick.* Neuron, 1997. **18**(3): p. 351-357.

34.   Levene, M.J., et al., *In vivo multiphoton microscopy of deep brain tissue.* Journal of neurophysiology, 2004. **91**(4): p. 1908-1912.

35.   Gather, M.C. and S.H. Yun, *Lasing from Escherichia coli bacteria genetically programmed to express green fluorescent protein.* Optics letters, 2011. **36**(16): p. 3299-3301.

36.   Galas, J., et al., *Microfluidic dye laser intracavity absorption.* Applied physics letters, 2006. **89**(22): p. 224101.

37.   Chen, Y., et al., *Optofluidic microcavities: Dye-lasers and biosensors.* Biomicrofluidics, 2010. **4**(4): p. 043002.

38.   Zhang, X., W. Lee, and X. Fan, *Bio-switchable optofluidic lasers based on DNA Holliday junctions.* Lab on a Chip, 2012. **12**(19): p. 3673-3675.

39.   Sun, Y. and X. Fan, *Distinguishing DNA by Analog‐to‐Digital‐like Conversion by Using Optofluidic Lasers.* Angewandte Chemie, 2012. **124**(5): p. 1262-1265.

40.   Grotjohann, T., et al., *Diffraction-unlimited all-optical imaging and writing with a photochromic GFP.* Nature, 2011. **478**(7368): p. 204-208.

41.   Hell, S.W. and M. Kroug, *Ground-state-depletion fluorscence microscopy: A concept for breaking the diffraction resolution limit.* Applied Physics B, 1995. **60**(5): p. 495-497.

42.   Hell, S.W., *Toward fluorescence nanoscopy.* Nature biotechnology, 2003. **21**(11): p. 1347-1355.

43.   Hell, S., S. Jakobs, and L. Kastrup, *Imaging and writing at the nanoscale with focused visible light through saturable optical transitions.* Applied Physics A, 2003. **77**(7): p. 859-860.

44.   Hell, S.W., M. Dyba, and S. Jakobs, *Concepts for nanoscale resolution in fluorescence microscopy.* Current opinion in neurobiology, 2004. **14**(5): p. 599-609.

45.   Adam, V., et al., *Data storage based on photochromic and photoconvertible fluorescent proteins.* Journal of biotechnology, 2010. **149**(4): p. 289-298.

46.   Miyawaki, A., *Proteins on the move: insights gained from fluorescent protein technologies.* Nature Reviews Molecular Cell Biology, 2011. **12**(10): p. 656-668.

47.   Webb, W.W., *Applications of fluorescence correlation spectroscopy.* Quarterly reviews of biophysics, 1976. **9**(01): p. 49-68.

48.   Lippincott-Schwartz, J., E. Snapp, and A. Kenworthy, *Studying protein dynamics in living cells.* Nature Reviews Molecular Cell Biology, 2001. **2**(6): p. 444-456.

49.   Capoulade, J., et al., *Quantitative fluorescence imaging of protein diffusion and interaction in living cells.* Nature biotechnology, 2011. **29**(9): p. 835-839.

50.   Matsuda, T., A. Miyawaki, and T. Nagai, *Direct measurement of protein dynamics inside cells using a rationally designed photoconvertible protein.* Nature Methods, 2008. **5**(4): p. 339-345.

51.   Giovannetti, V., S. Lloyd, and L. Maccone, *Quantum-enhanced measurements: beating the standard quantum limit.* Science, 2004. **306**(5700): p. 1330-1336.

52.   Drobizhev, M., et al., *Two-photon absorption properties of fluorescent proteins.* Nature methods, 2011. **8**(5): p. 393-399.

53.   Gather, M.C. and S.H. Yun, *Bio-optimized energy transfer in densely packed fluorescent protein enables near-maximal luminescence and solid-state lasers.* Nature communications, 2014. **5**.

54.   Upton, L., et al., *Optically excited entangled states in organic molecules illuminate the dark.* The Journal of Physical Chemistry Letters, 2013. **4**(12): p. 2046-2052.

55.   Oka, H., *Control of vibronic excitation using quantum-correlated photons.* The Journal of chemical physics, 2011. **135**(16): p. 164304.

56.   Schlawin, F., et al., *Suppression of population transport and control of exciton distributions by entangled photons.* Nature communications, 2013. **4**: p. 1782.

57.   Drobizhev, M., et al., *Resonance enhancement of two-photon absorption in fluorescent proteins.* The Journal of Physical Chemistry B, 2007. **111**(50): p. 14051-14054.

58. Helmchen, F. and W. Denk, *Deep tissue two-photon microscopy.* Nature methods, 2005. **2**(12): p. 932-940.

59. Chudakov, D.M., et al., *Fluorescent proteins and their applications in imaging living cells and tissues.* Physiological reviews, 2010. **90**(3): p. 1103-1163.

60. McCormick, C., et al., *Strong low-frequency quantum correlations from a four-wave-mixing amplifier.* Physical Review A, 2008. **78**(4): p. 043816.

61. Hall, M.A., J.B. Altepeter, and P. Kumar, *Drop-in compatible entanglement for optical-fiber networks.* Optics express, 2009. **17**(17): p. 14558-14566.

62. Shi, S., et al. *Generation of Photon Pairs in Green Fluorescent Protein*. in *Frontiers in Optics*. 2014. Optical Society of America.

63. Hayes, D., G.B. Griffin, and G.S. Engel, *Engineering coherence among excited states in synthetic heterodimer systems.* Science, 2013. **340**(6139): p. 1431-1434.

64. Lee, H., Y.-C. Cheng, and G.R. Fleming, *Coherence dynamics in photosynthesis: protein protection of excitonic coherence.* Science, 2007. **316**(5830): p. 1462-1465.

65. Christensson, N., et al., *High frequency vibrational modulations in two-dimensional electronic spectra and their resemblance to electronic coherence signatures.* The Journal of Physical Chemistry B, 2011. **115**(18): p. 5383-5391.

66. Christensson, N., et al., *Origin of long-lived coherences in light-harvesting complexes.* The Journal of Physical Chemistry B, 2012. **116**(25): p. 7449-7454.

67. Tiwari, V., W.K. Peters, and D.M. Jonas, *Electronic resonance with anticorrelated pigment vibrations drives photosynthetic energy transfer outside the adiabatic framework.* Proceedings of the National Academy of Sciences, 2013. **110**(4): p. 1203-1208.

68. Panitchayangkoon, G., et al., *Direct evidence of quantum transport in photosynthetic light-harvesting complexes.* Proceedings of the National Academy of Sciences, 2011. **108**(52): p. 20908-20912.

69. Boyd, R.W., *Nonlinear optics*. 2003: Academic press.

70. Wan, S., et al., *Photoabsorption of green and red fluorescent protein chromophore anions in vacuo.* Biophysical chemistry, 2007. **129**(2-3): p. 218-223.

71. Scully, M.O., *Quantum optics*. 1997: Cambridge university press.

72. Lin, Q., F. Yaman, and G.P. Agrawal, *Photon-pair generation in optical fibers through four-wave mixing: Role of Raman scattering and pump polarization.* Physical Review A, 2007. **75**(2): p. 023803.

73. Garrett, C. and D. McCumber, *Propagation of a Gaussian light pulse through an anomalous dispersion medium.* Physical Review A, 1970. **1**(2): p. 305.

74. Alibart, O., et al., *Photon pair generation using four-wave mixing in a microstructured fibre: theory versus experiment.* New Journal of Physics, 2006. **8**(5): p. 67.

75. Shi, S., P. Kumar, and K.F. Lee, *Generation of photonic entanglement in green fluorescent proteins.* Nature communications, 2017. **8**(1): p. 1934.

76.   Xu, C., et al., *Multiphoton fluorescence excitation: new spectral windows for biological nonlinear microscopy.* Proceedings of the National Academy of Sciences, 1996. **93**(20): p. 10763-10768.

77.   Zipfel, W.R., R.M. Williams, and W.W. Webb, *Nonlinear magic: multiphoton microscopy in the biosciences.* Nature biotechnology, 2003. **21**(11): p. 1369.

78.   Moneron, G. and S.W. Hell, *Two-photon excitation STED microscopy.* Optics express, 2009. **17**(17): p. 14567-14573.

79.   Vaziri, A., et al., *Multilayer three-dimensional super resolution imaging of thick biological samples.* Proceedings of the National Academy of Sciences, 2008. **105**(51): p. 20221-20226.

80.   Sheik-Bahae, M., et al., *Sensitive measurement of optical nonlinearities using a single beam.* Quantum Electronics, IEEE Journal of, 1990. **26**(4): p. 760-769.

81.   Svelto, O. and D.C. Hanna, *Principles of lasers.* 1998.

82.   Lu, S., et al., *Third order nonlinear optical property of Bi 2 Se 3.* Optics express, 2013. **21**(2): p. 2072-2082.

83.   Henderson, L. and V. Vedral, *Classical, quantum and total correlations.* Journal of physics A: mathematical and general, 2001. **34**(35): p. 6899.

84.   Ji, N., J.C. Magee, and E. Betzig, *High-speed, low-photodamage nonlinear imaging using passive pulse splitters.* Nature methods, 2008. **5**(2): p. 197.

85.   Donnert, G., C. Eggeling, and S.W. Hell, *Major signal increase in fluorescence microscopy through dark-state relaxation.* Nature methods, 2007. **4**(1): p. 81.

86.   Thomas, A. *Direct measurement of third-order nonlinearity of green fluorescent protein*. in *CLEO: Science and Innovations*. 2013. Optical Society of America.

87.   Hof, M., et al., *Fluorescence spectroscopy in biology: advanced methods and their applications to membranes, proteins, DNA, and cells*. Vol. 3. 2005: Springer Science & Business Media.

88.   Shi, S., et al., *Broadband photon pair generation in green fluorescent proteins through spontaneous four-wave mixing.* Scientific reports, 2016. **6**: p. 24344.

89.   Zhiwei, D., et al. *Nonlinear fluorescence properties of DCM dyes irradiated under femtosecond pulses*. in *Laser Physics and Laser Technologies (RCSLPLT) and 2010 Academic Symposium on Optoelectronics Technology (ASOT), 2010 10th Russian-Chinese Symposium on*. 2010. IEEE.

90.   Arbeloa, F.L., T.L. Arbeloa, and I.L. Arbeloa, *Electronic spectroscopy of pyrromethene 546.* Journal of Photochemistry and Photobiology A: Chemistry, 1999. **121**(3): p. 177-182.

91.   Assor, Y., Z. Burshtein, and S. Rosenwaks, *Spectroscopy and laser characteristics of copper-vapor-laser pumped pyrromethene-556 and pyrromethene-567 dye solutions.* Applied optics, 1998. **37**(21): p. 4914-4920.

92.   Lee, D.-I. and T. Goodson, *Entangled photon absorption in an organic porphyrin dendrimer.* The Journal of Physical Chemistry B, 2006. **110**(51): p. 25582-25585.

93.   Sua, Y.M., et al., *Generation of high-purity entangled photon pair in a short highly nonlinear fiber.* Optics letters, 2013. **38**(1): p. 73-75.

94.   Zhang, W., et al., *Impact of fiber birefringence on correlated photon pair generation in highly nonlinear microstructure fibers.* The European Physical Journal D, 2010. **59**(2): p. 309-316.

95.   Barbier, M., I. Zaquine, and P. Delaye, *Spontaneous four-wave mixing in liquid-core fibers: towards fibered Raman-free correlated photon sources.* new Journal of Physics, 2015. **17**(5): p. 053031.

96.   Dong, S., et al., *Energy-time entanglement generation in optical fibers under CW pumping.* Optics Express, 2014. **22**(1): p. 359-368.

97.   Munro, W.J., et al., *Maximizing the entanglement of two mixed qubits.* Physical Review A, 2001. **64**(3): p. 030302.

98.   Bose, S. and V. Vedral, *Mixedness and teleportation.* Physical Review A, 2000. **61**(4): p. 040101.

99.   Datta, A., A. Shaji, and C.M. Caves, *Quantum discord and the power of one qubit.* Physical review letters, 2008. **100**(5): p. 050502.

100.   Lanyon, B., et al., *Experimental quantum computing without entanglement.* Physical review letters, 2008. **101**(20): p. 200501.

101.   Vedral, V., *The role of relative entropy in quantum information theory.* Reviews of Modern Physics, 2002. **74**(1): p. 197.

102.   Modi, K., et al., *Unified view of quantum and classical correlations.* Physical review letters, 2010. **104**(8): p. 080501.

103.   Sua, Y.M., J. Malowicki, and K.F. Lee, *Quantum correlation of fiber-based telecom-band photon pairs through standard loss and random media.* Optics letters, 2014. **39**(16): p. 4808-4811.

104.   D'Angelo, M., M.V. Chekhova, and Y. Shih, *Two-photon diffraction and quantum lithography.* Physical Review Letters, 2001. **87**(1): p. 013602.

105.   Poh, H.S., et al., *Joint spectrum mapping of polarization entanglement in spontaneous parametric down-conversion.* Physical Review A, 2007. **75**(4): p. 043816.

106.   Kwiat, P.G., *Hyper-entangled states.* Journal of modern optics, 1997. **44**(11-12): p. 2173-2184.

107.   Slattery, O., et al., *Frequency correlated biphoton spectroscopy using tunable upconversion detector.* Laser Physics Letters, 2013. **10**(7): p. 075201.

108.   Bennink, R.S., et al., *Quantum and classical coincidence imaging.* Physical review letters, 2004. **92**(3): p. 033601.

109.   Cinelli, Riccardo AG, et al., *Coherent dynamics of photoexcited green fluorescent proteins*. Physical review letters 86.**15** (2001): p. 3439.